Universitat Autònoma de Barcelona

Exploring Synthetic Strategies for the Production of Complex Inorganic Nanoparticles

Javier Ivan Patarroyo Rengifo

Exploring Synthetic Strategies for the Production of Complex Inorganic Nanoparticles.

Javier Ivan Patarroyo Rengifo

Bellaterra, 2018

UAB
Universitat Autònoma de Barcelona

ICN2
Institut Català de Nanociència i Nanotecnologia
EXCELENCIA SEVERO OCHOA

Exploring Synthetic Strategies for the Production of Complex Inorganic Nanoparticles.

A thesis presented

by

Javier Ivan Patarroyo Rengifo

A thesis submitted to attain the degree of

DOCTOR IN MATERIAL SCIENCES of Universitat Autònoma de Barcelona

Director: Dr. Victor F. Puntes

Tutor: Dr. Jordi Pascual I Gainza

2018

“Let’s just say I was testing the bounds of reality. I was curious to see what would happen. That’s all it was: just curiosity.”

Jim Morrison.

Table of Contents

Acknowledgements

First, I would like to deeply thank my supervisor Prof. Dr. Victor F. Puntes who gave me the opportunity to be part of the *Inorganic Nanoparticles Group*. I appreciate the guidance, advice, support and motivation he provided me during my doctoral study. I will be always grateful. Likewise, I want to thank to Dr. Neus G. Bastús for her generous knowledge and valuable discussions throughout all this years. I would like to thank all members of the *Inorganic Nanoparticles Group,* both, past and present, (special thanks go to: Cecilia, Eudald, Ngoc, Marti, Sofia, Florind, Jordi Piella, Oscar and Jana Oliveras) for the wonderful time, unforgettable experiences shared inside and outside the ICN2 and because of them have contributed to my personal and professional growth.

I wish to express my appreciation to Dr. Edgar Gonzalez, for the fruitful scientific discussion during my stays in Bogota. I specially thank to Dr. Jordi Arbiol and Dr. Aziz Genç from GAeN group, for their valuable contribution with part of the electron microscopy imaging and the EDS measurements. I am deeply thankful to Dr. Belen Ballesteros and Marcos Rosado from the Electron Microscopy Division at ICN2 for their constant help.

I want to thank to Dr. Jorge Delgado, from OMICH group, for his friendship and his assistance with the selective hydrogenation essays, also for the fruitful discussion about the results. I want to thanks to the members of “empanadas” group, it is always nice to share your time with Colombian friends, gracias Luis, Cristina y Oscar. I would like to thank to my friends on both sides of the Atlantic Ocean for all the moments we spent together, special thanks to Carlos M, Lina, Sara, Male, Jairo, Milton, Jair, Leonardo... Thanks to Daniel A., for his genuine friendship, for join me to the summer festivals and so on.

Jana, només puc donar-te les gràcies per tot allò que hem compartit, t’estimo.

Finalmente, quiero agradecer a mi papa y mi mama, estoy aquí gracias a ustedes. También agradecer a mis hermanos por su apoyo. A mi familia estaré infinitamente agradecido por estar siempre presentes.

Moltes Gràcies a tots.

Javier P.

Objectives and Dissertation Outline

The aim of this thesis is i. to contribute to the development of reproducible methodologies for the production of high quality noble metal nanostructures, such as solid, hollow and hybrid nanostructures; and ii. to examine the potential applicability of these structures by exploring the nanoscale features that determine their optical, chemical and catalytic behaviour.

The thesis is divided into 7 chapters, as follows:

Chapter 1 introduces the field of the synthesis of noble metal nanoparticles. It includes a brief review of the polyol synthesis of metal NPs, followed by a description of techniques for the production of hollow nanostructures with special emphasis on galvanic replacement reaction and the Kirkendall effect. This is followed by a description of hybrid nanostructures and finally an explanation of surface plasmon resonance (SPR) phenomena.

Chapter 2 discusses the effect of the stabilizer in the synthesis of complex hollow metal nanostructures, from pinholed nanoboxes to double or single walled nanoboxes. Furthermore, the room temperature synthesis of biocompatible (CTAB-free) nanoboxes and the effective label free sensing of bovine serum albumin (BSA) of single walled nanoboxes is presented. These structures are then compared with solid Au NPs in order to demonstrate their excellent performance for possible biomedical applications.

Chapter 3 presents an experimental methodology for the production of bimetallic multidomain noble metal nanotubes (NTs), trimetallic noble metal NTs and tetrametallic noble metal NTs. This is followed by a study of the surface availability for the transfer of electrons of these structures through the catalytic reduction of 4-nitrophenol to 4-aminophenol by sodium borohydride in aqueous solution.

Chapter 4 discusses a polyol method for the production of highly monodisperse short green silver nanorods (NRs), in the presence of tannic acid (TA) and polyvinylpyrrolidone (PVP) and the effect of factors such as temperature, silver precursor, concentration of co-reducer species and the molecular weight of the stabilizer. A method for transforming these Ag NRs into hollow AgAu NRs by means of the GRR at room temperature is also discussed.

Chapter 5 presents a methodology for the synthesis in aqueous media of a new kind of heterogeneous nanostructure, formed by the combination of a noble metal (Au or Ag) and a CeO_2 domain. Depending on the reaction conditions, these nanostructure can have a core@shell or a heterodimer morphology.

Chapter 6, discusses how the heterodimer Ag/CeO_2 nanostructures described in chapter 5 can be transformed into bimetallic Ag-noble metal (Au, Pd or Pt) heterodimer hollow / CeO_2 nanostructures *via* GRR at room temperature. The effective use of heterodimer hollow AgPd/CeO_2 nanostructures in the selective hydrogenation of alkynes and alkynols is also demonstrated.

Finally, **Chapter 7** contains the general conclusions of the thesis.

A list of abbreviations, publications and contributions to conferences are detailed in **Appendix 1** and **Appendix 2** respectively.

Resumen

La presente tesis doctoral está dividida en 7 capítulos, a continuación se presenta una descripción de los mismos:

En el **capítulo 1** se introduce al lector el campo de la síntesis de nanopartículas compuestas por metales nobles. Este capítulo incluye un breve resumen de la síntesis de polialcohol de nanopartículas metálicas, seguido por una descripción de las técnicas de producción de nanoestructuras huecas con énfasis en la reacción de reemplazo galvánico y el efecto Kirkendall, seguido por la descripción de nanoestructuras hibridas y finalmente una explicación del fenómeno del plasmon de resonancia de superficie (SPR).

El **capítulo 2** discute el efecto del estabilizante en la síntesis de nanoestructuras metálicas huecas complejas, desde nanocajas agujereadas hasta nanocajas con una o con doble pared. Además, la síntesis a temperatura ambiente de nanocajas bio-compatibles (libres de CTAB) y se presenta la detección de albumina de suero bovino con nanocajas de pared sencilla. Estas estructuras son comparadas con nanoparticulas solidas de oro, para demostrar su excelente desempeño para posibles aplicaciones biomédicas.

En el **capítulo 3** se presenta una metodología experimental para la producción de nanotubos bimetálicos de metales nobles con múltiples dominios, nanotubos trimetalicos y tetrametálicos de metales nobles. También se estudió la disponibilidad de la superficie para la transferencia de electrones de estas nanoestructuras a través de la reducción catalítica de 4-nitrofenol a 4-aminofenol con boro hidruro de sodio en solución acuosa.

El **capítulo 4** discute un método de polialcohol para la producción de *nanorods* cortos de plata altamente monodispersos, en presencia de ácido tánico y polivinilpirrolidona. De igual forma, se discute el efecto de factores como temperatura, precursor de plata, concenteracion de las especies co-reductoras y el peso molecular del estabilizante. También se discute un método para transformar estos *nanorods* de plata en *nanorods* huecos de plata y oro, por medio de la reacción de reemplazo galvánico a temperatura ambiente.

En el **capítulo 5** se presenta una metodología para la síntesis en medio acuoso de una nueva clase de nanoestructura heterogénea, formada por la combinación de un metal noble

(Au o Ag) y un dominio de CeO_2. Dependiendo de las condiciones de reacción, estas nanoestructuras pueden tener una morfología tipo *"core@shell"* o tipo heterodimero.

En el **capítulo 6** se discute como las nanoestructuras tipo heterodimero de AgCeO2 descritas en el capítulo 5, pueden ser transformadas en heterodimeros huecos bimetálicos de Ag-metal noble (Au, Pd o Pt) / CeO_2 utilizando la reacción de reemplazo galvánico a temperatura ambiente. Se demostró el uso efectivo de las nanoestructuras heterodimeras huecas de $AgPdCeO_2$ en la hidrogenación selectiva de alquinos y alquinoles.

Finalmente, el **capítulo 7** contiene las conclusiones generales de la tesis doctoral.

Una lista de las abreviaciones utilizadas en esta tesis doctoral así como de las publicaciones y contribuciones en conferencias es presentada en los apéndices 1 y 2 respectivamente.

Chapter 1

Introduction

This chapter provides a background on the synthesis of metal nanoparticles (NPs) with a focus on the polyol method for the production of silver NPs. A general description of hollow and hybrid NPs as well as the SPR phenomena and the general synthetic methods for the fabrication of hollow noble metal nanostructures is presented.

Nanomaterials have been a very intriguing area of scientific research over the previous few decades because of their unique physical and chemical properties that make them suitable for applications in fields like photonics, catalysis, biomedicine, environmental remediation, energy conversion and storage, sensors, etc. There are two proposed definitions of nanomaterials. The first defines nanomaterials *as materials with sizes below 100 nm at least in one dimension*. This definition is quite broad and does not require deeper thoughts about properties and applications. The second definition is more restrictive, as it defines nanomaterials *as having properties that depend inherently on the small grain size* [1, 2].

The synthesis of NPs has been widely explored and, two main approaches have been used for their production, as presented in **Figure 1.1.** The first approach is known as *top-down*, which starts with a bulk material and systematically removes material until the desired NPs remains. This method usually involves mechanical energy, lasers, thermal and lithographic techniques [3]. The second method is known as a *bottom-up* method where colloidal NPs are self-assembled in solution by nucleation and further growth of atomic or molecular precursors [4].

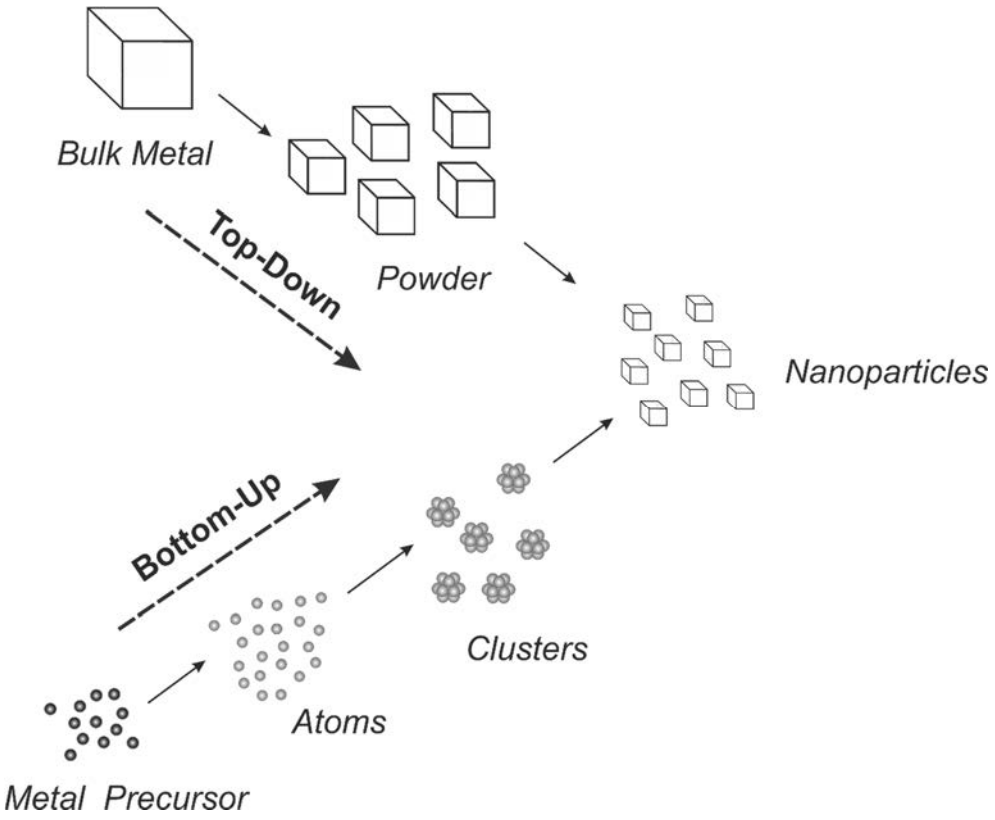

Figure 1.1. Schematic representation of top-down and bottom-up approaches for the synthesis of NPs. Adapted from reference [5]

The various parameters relating to the nature of metal NPs are schematically presented in **Figure 1.2**. It is well known that these parameters, i.e. material, size, morphology and composition, determine the physicochemical properties of the NPs and therefore, that atomic precision control of these parameters can lead to the production of complex functional nanostructures (**Figure 1.2E**).

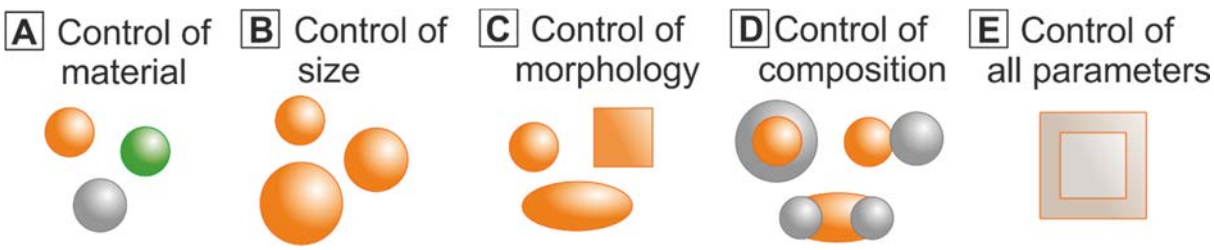

Figure 1.2. Parameter of control for the synthesis of metal NPs. Adapted from reference [4]

Due to their very small size, surface and confinement effects endow NPs with new important properties. For example Au and Ag NPs acquire their surface plasmonic properties as a result of confining the electromagnetic fields of much larger photons of resonance frequencies [6]. Thus, noble metal NPs with well-defined shapes have received considerable attention in recent years due to the fact that their electronic, catalytic and plasmonic properties depends on their morphology.

1.1. Polyol synthesis of metal NPs. The term polyol process was first reported by Fievet, Lagier and Figlarz in 1989 [7, 8] for the synthesis of sub-micrometer sized metal NPs that need a reducing environment. The polyol synthesis started with Co, Ni, Cu, and Pt NPs and was extended to further metals, intermetallics and alloys such as Re, Ru, Rh, Au, Sn, CoNi, FeNi, Co_xCu_{1-x}, or FeCoNi. [9-11]

Polyol synthesis is a liquid phase procedure that provides a simple and versatile route for the synthesis of noble metal NPs with various sizes and morphologies. This method uses a polyalcohol that acts not only as a solvent but also as a reducing agent. In this process, a metal salt used as the precursor is dissolved in a liquid polyol, the solution is then stirred and heated to a given temperature to achieve the reduction of the metal precursor. The choice of the polyol used for the reduction of a metal precursor is determined by the boiling point and the reduction potential of the polyol. Thus, easily reducible metals like Ag, Pd or Cu do not require high temperatures and can be reduced in ethylene glycol (Bp: 197.3 °C) or propylene glycol (Bp: 188.2 °C). However, less easily reducible metals such as Co, Fe or Ni require higher temperatures for which tetraethylene glycol may be suitable (Bp: 327 °C). The structures are presented in **Figure 1.3.** [9]

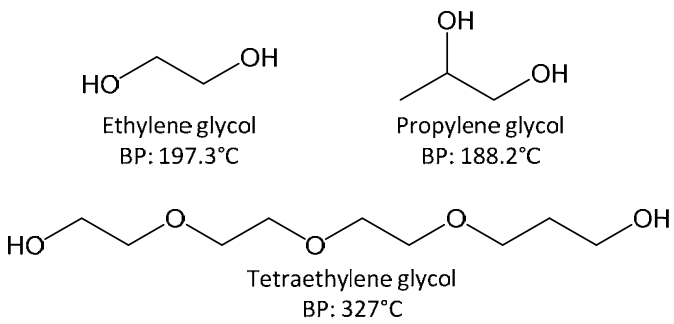

Figure 1.3. Polyols used for the reduction of metal salt precursors. Varying the hydroxyl sites has an effect on the overall reduction potential of the polyol along with its boiling point.

1.1.1. Polyol synthesis of Ag NPs. Ethyleneglycol (EG) is the most commonly used polyol for the synthesis of Ag [10, 11], Pd [12] and Pt [13] NPs. The metal NPs are formed by nucleation and growth from the solution. **Scheme 1.1** outlines the possible mechanism of reducing Ag^+ by the polyol method in ethylene glycol. The mechanism for precursor reduction involves the thermal oxidation of ethylene glycol to glycolaldehyde, which is responsible for reducing Ag^+ to Ag [14]. The obtained Ag atoms will start to nucleate and grow into clusters, seeds and then nanocrystals. The initial nucleation process plays an important role in determining the shape of final products. In order to acquire desired nanostructure with good uniformity, the nucleation process should be precisely controlled [15].

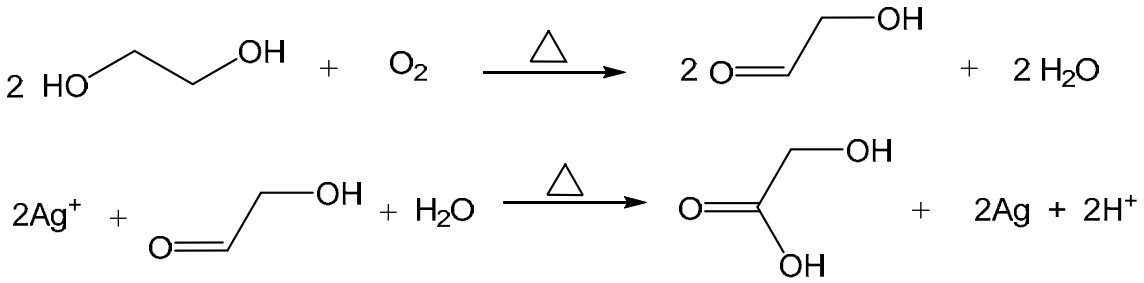

Scheme 1.1. Possible mechanism for the reduction of Ag^+ by EG.

1.1.2. Use of polivinylpyrrolidone (PVP) on the polyol synthesis of Ag NPs. The shape control of Ag nanostructures by the polyol method requires a strict control of the reactions parameters, such as temperature, stirring rate, reaction time, PVP molecular weight as well as the molar ratio of PVP and Ag precursor [16]. A slight modification of these parameters may result in a completely different morphology to that expected. Morphological control of the synthesis of Ag NPs enables optimization of the surface plasmon resonance (SPR) and the local electric field strength for chemical sensing [7] or surface-enhanced Raman scattering (SERS) [8].

A number of organic materials are known to work as NPs stabilizing agent, among them PVP, (a bulky, non-toxic, non-ionic polymer with C=O, C-N and CH_2 functional groups that is widely used in NPs synthesis [17]); which passivate the nanocrystal surface and prevents the aggregation of NPs via the steric hindrance effect [18]. By adjusting the molar ratio between PVP and Ag precursor, the degree of coating and distribution of PVP chains on the surface of the Ag seeds can be modified. This modification, changes the growing kinetic

of different facets, and leads to the formation of Ag nanostructures with different morphologies. **Figure 1.4** shows different nanostructures that can be obtained through the polyol method in which PVP is used as a stabilizer and shape directing agent in EG. These nanostructures are nanocubes [19], nanowires [20], bipyramids [21], nanobars [22] octahedron [23], square prismatic [24] and nanorods [25] (which are explained in detail in **Chapter 4**).

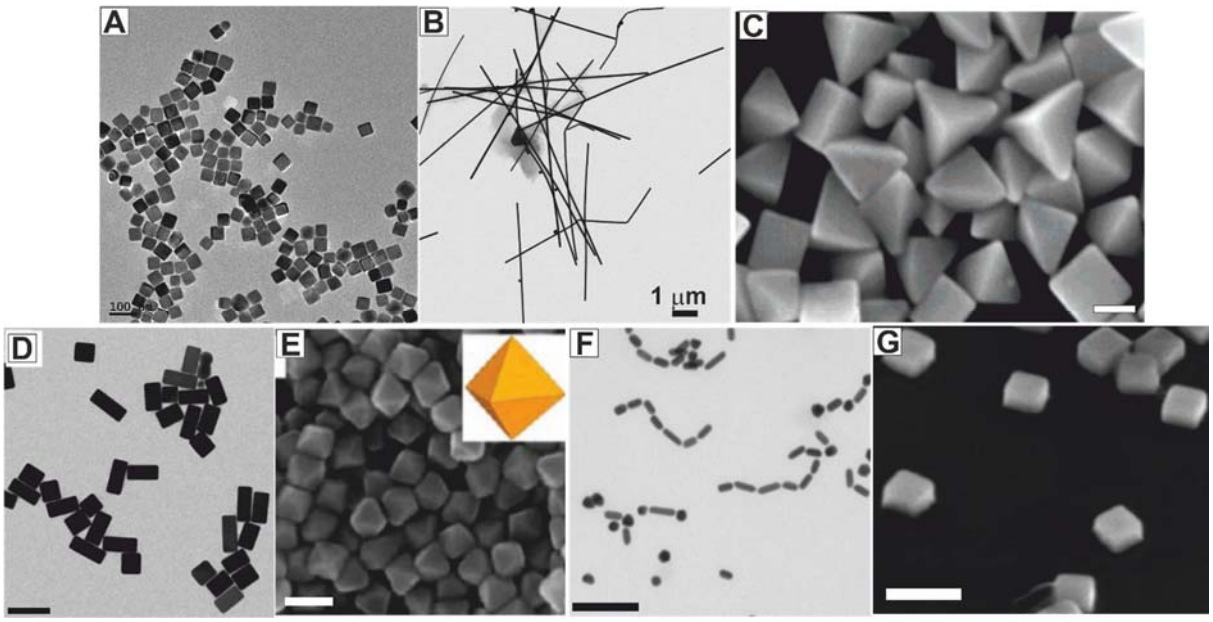

Figure 1.4. Electron microscope images of Ag NPs synthesized by the polyol method using PVP as stabilizer. **A,** nanocubes; **B,** nanowires; **C,** bipyramids (adapted from reference [21]); **D,** nanobars (adapted from reference [22]); **E,** octahedron (adapted from reference [23]) and **F,** nanorods; **G**, square prismatic (adapted from reference [24])

Different morphologies can be obtained because PVP selective attach to different Ag crystal planes, promoting the growth of specific crystal faces while hindering others [26]. For example, in EG, PVP interacts more strongly with silver atoms located in the {100} facets, (through interaction of the carbonyl group of the repeating unit), than with those on the {111} (lower energy facets), allowing growth along <111> directions to obtain Ag NRs or Ag NWs [27-29].

1.2. Hollow Nanostructures. The synthesis of hollow nanostructures is not as easy as that solid ones. Over the last two decades, research onto hollow nanostructures has grown significantly as evidenced by the exponential increase in the number of articles published (**Figure 1.5**).

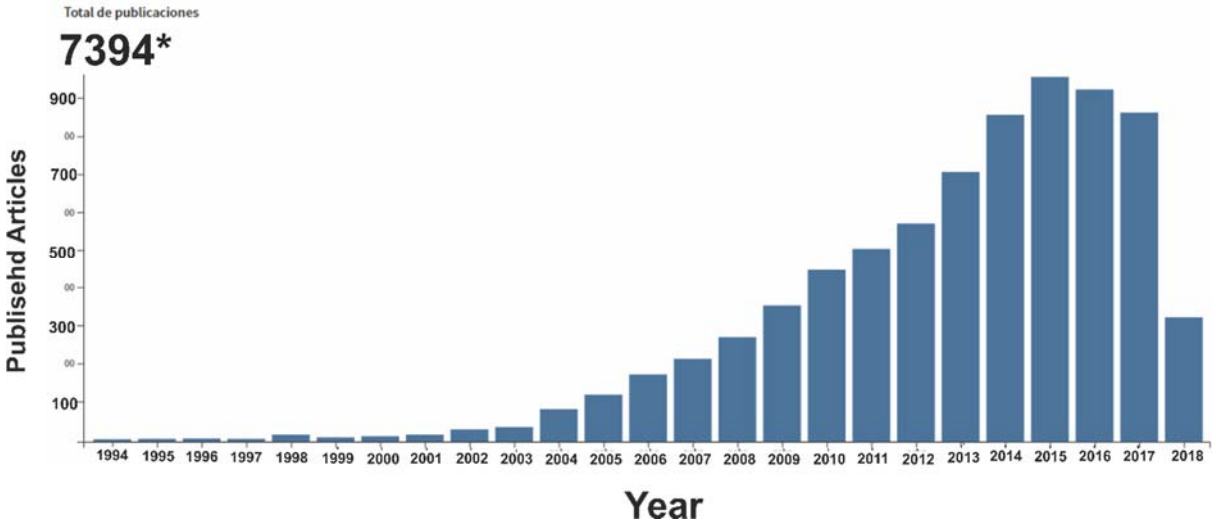

Figure 1.5. Representation of the number of research articles published in the period 1994-2018 according to Web of Science containing the term "*hollow nanostructures*" as keyword. The asterisk* indicates that the result was obtained on May the 8th of 2018.

Hollow metal nanostructures have attracted a lot of interest by virtue of their wide range of applications with performances better than their solid counterparts. These advantages are primarily due to a unique architecture, in that a hollow design provides these nanostructures with both an inner and an outer surface. This has made hollow nanostructures very appealing in many areas of science and technology. Above all, they have been extensively studied for their applications in sensing [30], SERS [31, 32], photoacoustic imaging [33] catalysis [30] bioencapsulation [34], and areas such as drug delivery [35] and removal of pollutants. Additionally, hollow metal nanostructures have superior surface plasmonic properties [36], as they have two coupled plasmon surface fields, inside and outside the NP walls. These fields can couple to produce a much enhanced field, which extends the use of their properties to many sensing applications [37] and photothermal agents for hyperthermia, triggers for drug delivery and contrast-enhancing agents in optical imaging.

1.2.1 General perspective on the synthesis of hollow nanostructures. The most popular approach for the production of hollow nanostructures involves the deposition of the desired material onto a sacrificial template which is removed once the shell is formed leaving a hollow nanostructure [38]. These template strategies, based on the coating of pre-fabricated templates with a layer of a shell material, are conceptually the simplest ones. By the use of hard templates, hollow nanostructures are obtained after a selective removal process, which typically involves processes of dissolution [39], chemical etching [40], or thermal decomposition [41] (See **Figure 1.6**). The void size, and the morphology of the hollow nanostructure are determined by the nature of the template, while the composition, thickness and porosity of the shell is mainly defined in the coating and removal processes. As a result, a wide variety of hollow NPs with different morphologies and compositions have been produced using hard templates such as, polymers [42, 43], silica [44, 45], and carbon particles [46].

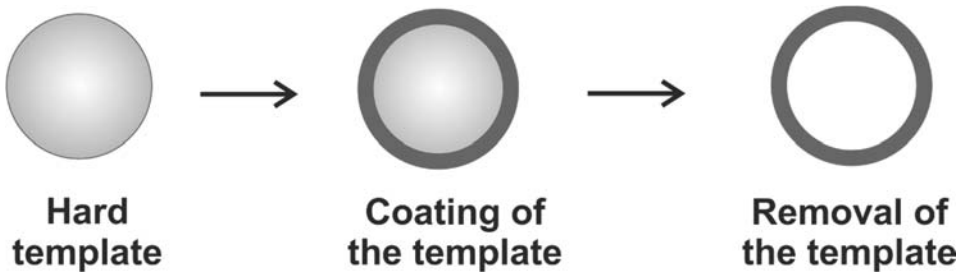

Figure 1.6. Schematic representation of hard template strategy for the synthesis of hollow nanostructures.

Despite their simplicity and versatility, traditional templating strategies present some important drawbacks associated with the scale up and the complexity of the surface deposition processes needed for the shell formation, which usually involve tedious procedures, and the use of toxic etchants or solvents in the removal processes. In this regard, the direct synthesis of hollow nanostructures without the need of additional steps is significantly advantageous due to reduced production costs, high reproducibility, great control over particle morphology and an easy scale up. Some results have been reported for the synthesis of hollow NPs in which the templates are consumed during shell deposition and hollow NPs are directly obtained without further treatment to remove the templates. In such a process, one of the reactants acts as the template for the formation of hollow structures. The advantage of utilizing such a template is that the template is automatically removed at

the end of the reaction, which avoids the need of a posterior step of having to remove the templates to obtain hollow products. This methodology is called galvanic replacement reaction and will be explained in the following section.

1.2.2 Synthesis of hollow nanostructures by galvanic replacement reaction (GRR). GRR provides a versatile approach for the transformation of monometallic solid NPs into more complex multimetallic nanostructures with hollow interiors, with tuneable and well controlled properties that are often not attainably by other methods [19, 30]. Over the past few years, remarkable progress has been made in the use of GRR for generating complex multimetallic hollow nanostructures with controllable hollow interiors. This approach involves the reaction of solid metal nanostructures used as sacrificial templates (usually Ag [19], but also Cu [47], Co [48], Ni [49], Mg [50] or Pd [51]) and a precursor containing a relatively more noble metal ion, in a process in which the composition of the template is modified while retaining its initial morphology. **Figure 1.7** shows the schematic illustration of the morphological and structural changes involved in GRR between an Ag nanocube (NC) and $HAuCl_4$ solution. The cross sectional view corresponds to the plane along the dashed lines. The major steps of the reaction are i) formation of a pinhole at one of the faces, ii) enlargement of the voids, iii) continuation of the GRR resulting in a partially hollow nanostructure, and iv) fragmentation of the nanostructures [52] .

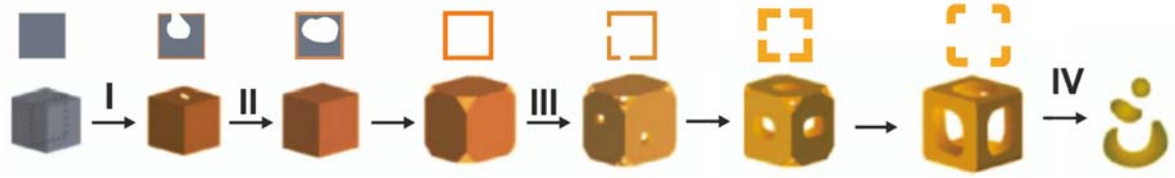

Figure 1.7. Schematic illustration of the morphological and structural changes involved in GRR between an Ag NC and $HAuCl_4$ solution (adapted from reference [52]).

Silver is commonly used as sacrificial template for GRR due to its relatively low electrochemical potential and well stablished colloidal chemistry [47, 53]. In GRR with Ag, the atoms of the template oxidize and dissolve ($Ag^0 \rightarrow Ag^+ + e^-$), while the ions of the more noble metal precursor are simultaneously reduced onto it ($M^{+n} + ne^- \rightarrow M^0$). The driving force for this reaction comes from the difference in reduction potentials of the two metals involved, with the potential of the second metal necessarily being higher than that of the first metal. **Table 1** summarizes the standard reduction potentials of metals commonly used in GRR [54].

It should be noted that the potentials presented in **Table 1.** are for the standard conditions. Variations in temperature and concentrations of relevant ions, as well as the involvement of other non-standard conditions can all affect the value of reduction potentials [55].

Table 1. Reduction potentials of metals relative to the standard hydrogen electrode (SHE).

Reduction reaction	***E_0 (V vs. SHE)****
$Co^{2+} + 2e^- \rightarrow Co$	–0.28
$Cu^{2+} + 2e^- \rightarrow Cu$	0.34
$Ag^+ + e^- \rightarrow Ag$	0.80
$Pd^{2+} + 2e^- \rightarrow Pd$	0.95
$Pt^{2+} + 2e \rightarrow Pt$	1.18
$Au^{3+} + 3e^- \rightarrow Au$	1.50

*For ideal conditions at 25 °C and 1 atm.

The chemical reduction process is initially confined to the vicinity of the Ag template surface, leading to the nucleation and growth of the noble metal precursor, which forms a thin shell that oxidizes and dissolves the Ag template and creates a pinhole, as shown in **Figure 1.8.**

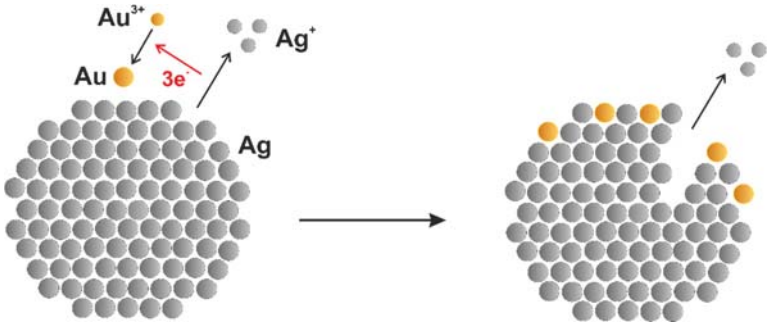

Figure 1.8. Schematic illustration of the morphological change at the first stages of GRR of Ag templates with Au^{+3} precursor. Adapted from reference [54].

The first demonstration of GRR in the synthesis of hollow noble metal NPs was reported by Xia and co-workers in 2002 [56]. In this work, GRR at high temperature between $HAuCl_4$ and Ag NPs used as a template led to the formation of hollow NPs with well-defined void spaces and crystalline walls. Since Xia's pioneering work, a wide variety of AgAu hollow nanostructures with controlled composition, morphology and internal structure have been produced. The elemental composition of the final NPs can be adjusted

by selecting the nature of the sacrificial template, and the concentration, type and number of metal precursors involved in the reaction. Thus, in addition to AgAu hollow nanostructures, AgPt [57, 58], AgPd [59], PdPt [60] and trimetallic PdAuAg hollow nanostructures [61], can be prepared via GRR. Beyond chemical composition, the morphology of the hollow nanostructures can be easily controlled by the choice of the template because as the deposition of precursor atoms takes place on the surface of the template, the final hollow NPs retains the shape of the original template [56].

Xia's group has widely studied the synthesis of Au nanocages (**Figure 1.9A**) through the GRR of Ag NCs [62] and, Ag NWs have been similarly exploited as template for the preparation of hollow nanotubes (**Figure 1.9B**) [63], other structures commonly obtained through GRR between $HAuCl_4$ and the corresponding Ag template include nanorings (**Figure 1.9C**) [64], octahedral nanoframes (**Figure 1.9D**) [65], and nanorattles (**Figure 1.9E**) [66].

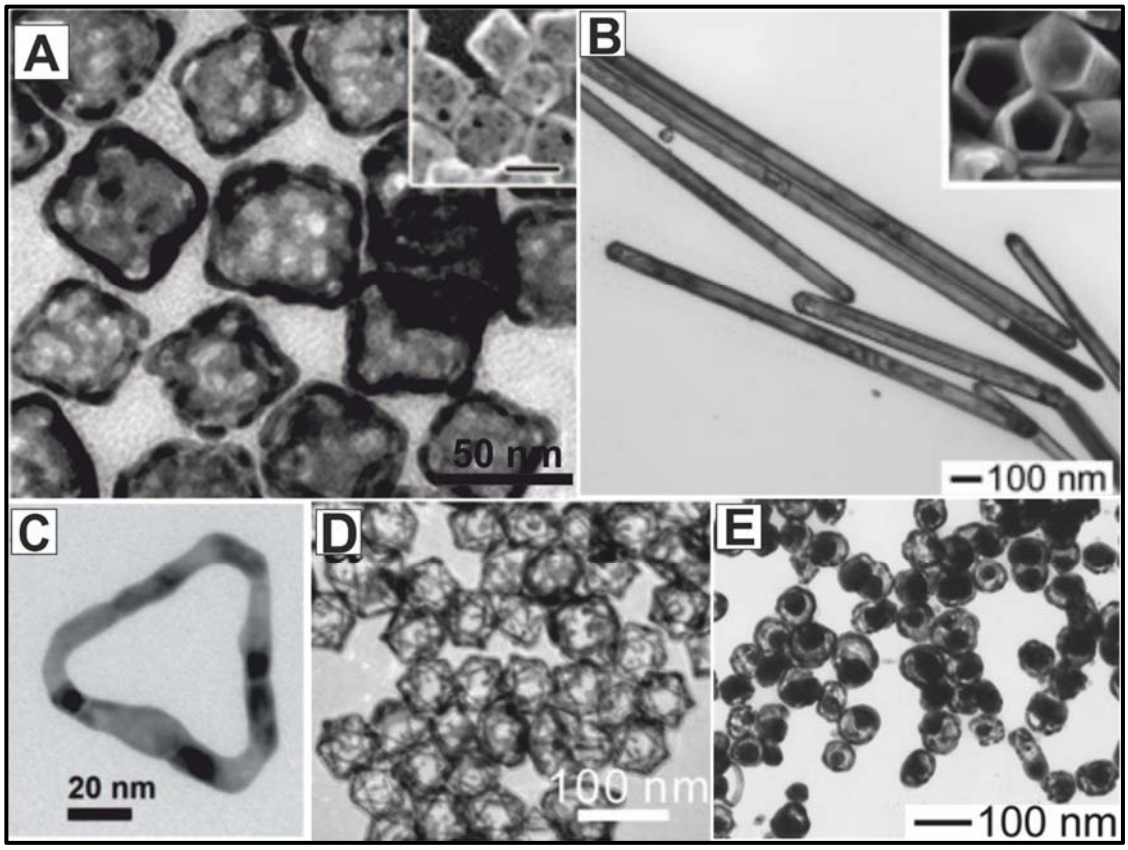

Figure 1.9. TEM images of **A.** AgAu nanocages [62]. **B.** AgAu NTs [63]. **C.** Au nanoring [64]. **D.** AgAu octahedral nanoframes [65] and **E.** AgAu nanorattles [66].

By coupling GRR with other chemical/physical processes, complex hollow nanostructures, such as multiple walled nanotubes [67] or multiple walled nanoshells [66] can be obtained.

1.2.3 Kirkendall effect. The Kirkendall effect has been also used very effectively in the preparation of hollow nanostructures [68, 69]. Initially, in this chemical transformation, NPs of controlled size, composition and morphology are exposed to oxygen, sulphur or selenium precursors under elevated temperatures, resulting in a diffusion couple. As a result of the faster outward diffusion of the metal cations compare with the inward diffusion of the anions, a flux of vacancies is created. When the vacancies supersaturate, they coalesce into voids which results in the production of hollow NPs.

As an alternative to GRR, the Kirkendall effect has been exploited to produce hollow noble metal NPs with controlled interior voids and shell thickness at the nanoscale [70]. The NPs result from the difference of the solid-state diffusion rates of the reactants in an alloying or oxidation reaction. More specifically, voids are formed due to a higher rate of outward core atoms compare with the inward rate of the added secondary species into the NP core [71]. In the case of AgAu NP formation (see **Figure 1.10**), due to the atomic radius ratio, Ag diffuses more quickly into Au than Au into Ag resulting in an AgAu alloy shell surrounding a hollow core [72].

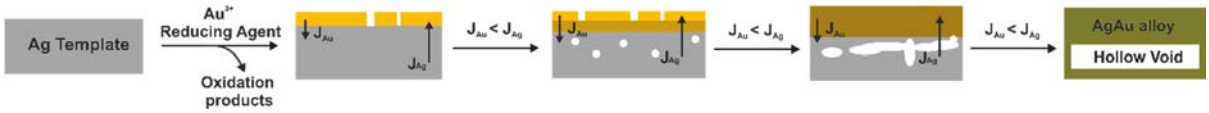

Figure 1.10. Schematic representation of the Kirkendall diffusion process. Adapted from reference [72]

The simultaneous or sequential action of GRR and the Kirkendall effect has been found an interesting synthetic route for the production of polymetallic hollow NPs with various morphologies and compositions. For example Gonzalez and co-workers [30] showed the possibility of producing complex bimetallic multi hollow NPs at room temperature, as is shown in **Figure 1.11**.

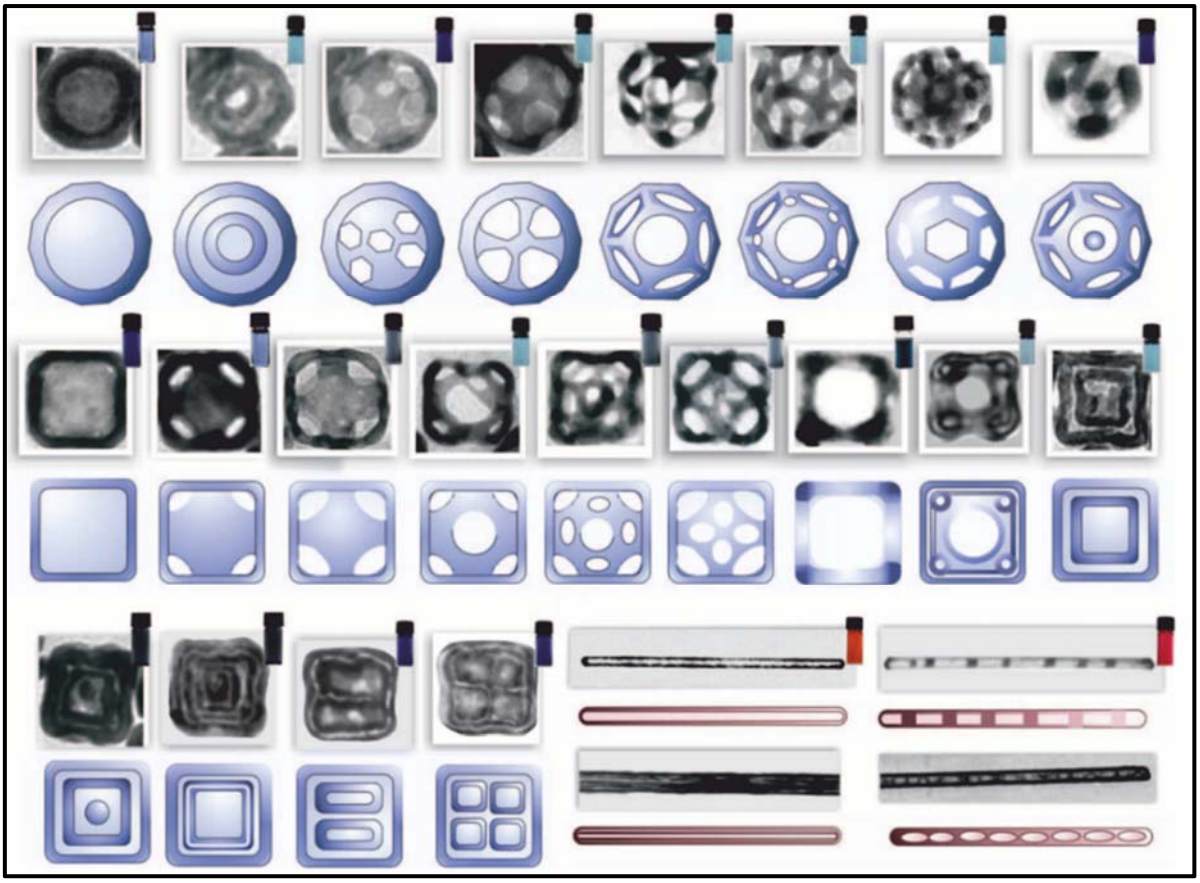

Figure 1.11. TEM images and schematic representation of the different morphologies produced by the simultaneous or sequential action of GRR and the Kirkendall effect. Adapted from reference [30].

1.3. Hybrid nanostructures. The wide applicability of inorganic NPs can be increased by designing nanostructures with a precise morphological control of their composition and structure. In the last few years, a big effort has been directed towards the design and synthesis of hybrid NPs, which combine two or more components into one individual structure. The main advantage of these structures is that exhibit unique characteristics that are greater than the sum of their parts as they have the potential to combine magnetic, plasmonic, semiconducting or other physical or chemical properties into a single object, therefore providing an increased functionality [73, 74]. The first efforts began with core@shell hybrid NPs, in which the core and shell are composed of different materials, such as a combination of semiconductors [75] and magneto-plasmonic NPs [76]. Later studies produced morphologies that deviated significantly from core@shell architectures, among them heterodimers made of spherical domains [77], nano-dumbell [78], hybrid

nanostructures; and other structures, such as branched NPs decorated with several domains [79].

In the case of noble metal – metal oxide hybrid nanostructures, according to the geometrical configuration of hybrid nanostructure, they can be sub-divided into [74] i) noble metal decorated metal oxide NPs; ii) noble metal@metal oxide core@shell nanostructures; iii) noble metal/metal oxide yolk/shell nanostructures; and iv) noble metal–metal oxide heterodimer nanostructures as shown in **Figure 1.12.**

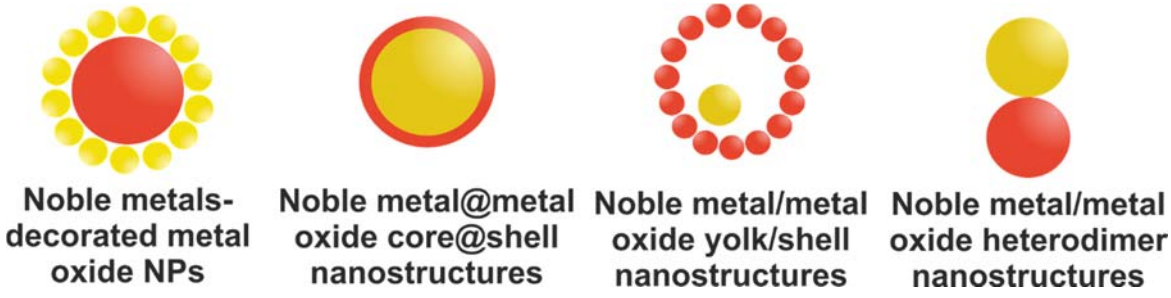

Figure 1.12. Schematic representation of different structures of noble metal–metal oxide nanostructures. Adapted from reference [74].

Hybrid NPs hold great promise for a number of potential uses ranging from nanoelectronics, biomedical, photovoltaic and catalytic applications [80, 81].

1.4. Surface plasmon resonance (SPR). Conductive metals contain large numbers of free electrons and, because they are not strongly bound to individual atoms, the electrons can easily respond to specific external stimuli. When a small spherical metallic NP is irradiated by light, the oscillating electric field causes the conduction electrons to oscillate coherently. When the electron cloud is displaced relative to the nuclei, a restoring force arises from Coulomb attraction between electrons and nuclei that results in oscillation of the electron cloud relative to the nuclear framework as is schematically represented in **Figure 1.13.** This oscillation is known as surface plasmon resonance (SPR) and the oscillation frequency is determined by the density of electrons, the effective electron mass, the shape and size of the charge distribution, the size and the structure of the particles, their interaction with other particles and the dielectric properties of the surrounding medium [82].This plasmon absorption , which is the origin of the observed colour in NPs solution, is a NP effect, it is absent in the individual atoms as well as in the bulk.

In the case of nanorods (NRs), these nanostructures differ from spherical NPs by the appearance of two distinct surface plasmon bands in the visible region, the transverse surface plasmon band (**Figure 1.13B**) and the longitudinal surface plasmon band (**Figure 1.13C**). Both of these bands correspond to light absorption along the short axis and scattering along the long axis. While the transverse surface plasmon band is usually at the same wavelength as that of the nanospheres, with no dependence on the aspect ratio, the longitudinal surface plasmon band of the NRs is dependent on their overall size and aspect ratio.

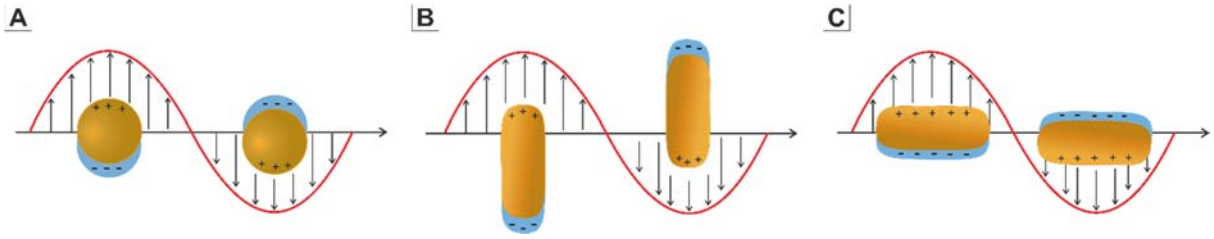

Figure 1.13. Schematic representation of SPR in: **A.** Au sphere **B.** Au NR s longitudinal SPR **C.** transversal SPR [82]. The red line and black arrows show the direction of electric field.

Many of the photonic and photothermal properties of plasmonic NPs are derived from the strong plasmonic electromagnetic fields resulting from localized surface plasmon resonance, which are stronger than those of the exciting resonant light. Furthermore, hollow nanostructures are known to have better plasmonic properties than their solid counterparts, thanks to the plasmon hybridization mechanism [83], which results in the enhanced plasmon field and a more homogeneous distribution.

SPR is dependent on the size and morphology of the NPs as well as the interfacial properties and, therefore the local environment surrounding plasmonic NPs is also an important factor. As the refractive index of the surrounding medium is increased, the SPR red-shifts to longer wavelengths. This effect allows plasmonic NPs to be used as efficient molecular sensors. When molecules adsorb to or desorb from the NP surface, the local refractive index changes, resulting in an SPR wavelength shift. This effect is also why gold NPs exhibit different SPR wavelengths depending on the surface coating.

The research on SPR is fundamental for the application in fields such as sensors, photonics, photocatalysis and surface enhanced Raman spectroscopy [84].

1.5 References

1. Vollat, D., *Nanoparticles - Nanocomposites – Nanomaterials: An Introduction for Beginners*. 2013: Wiley - VCH Verlag GmbH & Co. KGaA.
2. Vollay, D., *Nanomaterials: An Introduction to Synthesis, Properties and Applications*. 2nd ed. 2013: Wiley-VCH Verlag GmbH & Co. KGaA.
3. Merkel, T.J., et al., *Scalable, Shape-Specific, Top-Down Fabrication Methods for the Synthesis of Engineered Colloidal Particles.* Langmuir, 2010. **26**(16): p. 13086-13096.
4. Parak, W.J., *Complex Colloidal Assembly.* Science, 2011. **334**(6061): p. 1359-1360.
5. Zahmakran, M. and S. Ozkar, *Metal nanoparticles in liquid phase catalysis; from recent advances to future goals.* Nanoscale, 2011. **3**(9): p. 3462-3481.
6. Henglein, A., *Small-particle research: physicochemical properties of extremely small colloidal metal and semiconductor particles.* Chemical Reviews, 1989. **89**(8): p. 1861-1873.
7. Fievet, F., J. Lagier, and M. Figlarz, *Preparing Monodisperse Metal Powders in Micrometer and Submicrometer Sizes by the Polyol Process.* MRS Bulletin, 1989. **14**(12): p. 29-34.
8. Fievet, F., et al., *Homogeneous and heterogeneous nucleations in the polyol process for the preparation of micron and submicron size metal particles.* Solid State Ionics, 1989. **32**: p. 198-205.
9. G. Viau, F.R., and O. Acher, *Preparation and microwave characterization of spherical and monodisperse Co20Ni80 particles.* Journal of Applied Physics, 1994. **76**(10): p. 6570-6572.
10. Viau, G., F. Fiévet-Vincent, and F. Fiévet, *Monodisperse iron-based particles: precipitation in liquid polyols.* Journal of Materials Chemistry, 1996. **6**(6): p. 1047-1053.
11. Chow, G.M., et al., *Structural, morphological, and magnetic study of nanocrystalline cobalt-copper powders synthesized by the polyol process.* Journal of Materials Research, 2011. **10**(6): p. 1546-1554.
12. Carroll, K.J., et al., *Preparation of Elemental Cu and Ni Nanoparticles by the Polyol Method: An Experimental and Theoretical Approach.* The Journal of Physical Chemistry C, 2011. **115**(6): p. 2656-2664.
13. Wiley, B., Y. Sun, and Y. Xia, *Synthesis of Silver Nanostructures with Controlled Shapes and Properties.* Accounts of Chemical Research, 2007. **40**(10): p. 1067-1076.
14. Wiley, B., et al., *Shape-Controlled Synthesis of Metal Nanostructures: The Case of Silver.* Chemistry – A European Journal, 2005. **11**(2): p. 454-463.
15. Xia, X., et al., *Facile Synthesis of Palladium Right Bipyramids and Their Use as Seeds for Overgrowth and as Catalysts for Formic Acid Oxidation.* Journal of the American Chemical Society, 2013. **135**(42): p. 15706-15709.
16. Herricks, T., J. Chen, and Y. Xia, *Polyol Synthesis of Platinum Nanoparticles: Control of Morphology with Sodium Nitrate.* Nano Letters, 2004. **4**(12): p. 2367-2371.
17. Skrabalak, S.E., et al., *On the Polyol Synthesis of Silver Nanostructures: Glycolaldehyde as a Reducing Agent.* Nano Letters, 2008. **8**(7): p. 2077-2081.
18. Wu, F., et al., *Bromide (Br) - Based Synthesis of Ag Nanocubes with High-Yield.* Scientific Reports, 2015. **5**: p. 10772.
19. Skrabalak, S.E., et al., *Facile synthesis of Ag nanocubes and Au nanocages.* Nature Protocols, 2007. **2**: p. 2182.
20. Koczkur, K.M., et al., *Polyvinylpyrrolidone (PVP) in nanoparticle synthesis.* Dalton Transactions, 2015. **44**(41): p. 17883-17905.
21. Si, R., et al., *Self-Organized Monolayer of Nanosized Ceria Colloids Stabilized by Poly(vinylpyrrolidone).* The Journal of Physical Chemistry B, 2006. **110**(12): p. 5994-6000.
22. Sun, Y. and Y. Xia, *Shape-Controlled Synthesis of Gold and Silver Nanoparticles.* Science, 2002. **298**(5601): p. 2176-2179.
23. Sun, Y. and Y. Xia, *Large-Scale Synthesis of Uniform Silver Nanowires Through a Soft, Self-Seeding, Polyol Process.* Advanced Materials, 2002. **14**(11): p. 833-837.

24. Wiley, B.J., et al., *Right Bipyramids of Silver: A New Shape Derived from Single Twinned Seeds.* Nano Letters, 2006. **6**(4): p. 765-768.
25. Zhang, Q., et al., *Synthesis of Ag Nanobars in the Presence of Single-Crystal Seeds and a Bromide Compound, and Their Surface-Enhanced Raman Scattering (SERS) Properties.* Langmuir, 2012. **28**(24): p. 9047-9054.
26. Xia, X., et al., *Quantitative Analysis of the Role Played by Poly(vinylpyrrolidone) in Seed-Mediated Growth of Ag Nanocrystals.* Journal of the American Chemical Society, 2012. **134**(3): p. 1793-1801.
27. Hsu, S.-W. and A.R. Tao, *Halide-Directed Synthesis of Square Prismatic Ag Nanocrystals by the Polyol Method.* Chemistry of Materials, 2018.
28. Patarroyo, J., et al., *One-pot polyol synthesis of highly monodisperse short green silver nanorods.* Chemical Communications, 2016. **52**(73): p. 10960-10963.
29. Wu, X., et al., *PVP-assisted synthesis of shape-controlled CuFeS2 nanocrystals for Li-ion batteries.* Journal of Materials Science, 2015. **50**(12): p. 4250-4257.
30. Saidi, W.A., H. Feng, and K.A. Fichthorn, *Binding of Polyvinylpyrrolidone to Ag Surfaces: Insight into a Structure-Directing Agent from Dispersion-Corrected Density Functional Theory.* The Journal of Physical Chemistry C, 2013. **117**(2): p. 1163-1171.
31. Sun, Y., et al., *Polyol Synthesis of Uniform Silver Nanowires: A Plausible Growth Mechanism and the Supporting Evidence.* Nano Letters, 2003. **3**(7): p. 955-960.
32. Xia, X., et al., *Recent Developments in Shape-Controlled Synthesis of Silver Nanocrystals.* The Journal of Physical Chemistry C, 2012. **116**(41): p. 21647-21656.
33. González, E., J. Arbiol, and V.F. Puntes, *Carving at the Nanoscale: Sequential Galvanic Exchange and Kirkendall Growth at Room Temperature.* Science, 2011. **334**(6061): p. 1377-1380.
34. Rycenga, M., et al., *Probing the surface-enhanced Raman scattering properties of Au-Ag nanocages at two different excitation wavelengths.* Physical Chemistry Chemical Physics, 2009. **11**(28): p. 5903-5908.
35. Schwartzberg, A.M., et al., *Improving Nanoprobes Using Surface-Enhanced Raman Scattering from 30-nm Hollow Gold Particles.* Analytical Chemistry, 2006. **78**(13): p. 4732-4736.
36. Li, W., et al., *Gold nanocages as contrast agents for photoacoustic imaging.* Contrast Media & Molecular Imaging, 2011. **6**(5): p. 370-377.
37. Marinakos, S.M., et al., *Gold Particles as Templates for the Synthesis of Hollow Polymer Capsules. Control of Capsule Dimensions and Guest Encapsulation.* Journal of the American Chemical Society, 1999. **121**(37): p. 8518-8522.
38. Hyuk Im, S., U. Jeong, and Y. Xia, *Polymer hollow particles with controllable holes in their surfaces.* Nat Mater, 2005. **4**(9): p. 671-675.
39. Genç, A., et al., *Tuning the Plasmonic Response up: Hollow Cuboid Metal Nanostructures.* ACS Photonics, 2016. **3**(5): p. 770-779.
40. Mahmoud, M.A., F. Saira, and M.A. El-Sayed, *Experimental Evidence For The Nanocage Effect In Catalysis With Hollow Nanoparticles.* Nano Letters, 2010. **10**(9): p. 3764-3769.
41. Wang, X., et al., *Synthesis, Properties, and Applications of Hollow Micro-/Nanostructures.* Chemical Reviews, 2016. **116**(18): p. 10983-11060.
42. Kundu, S. and N. Ravishankar, *Rapid synthesis of hybrids and hollow PdO nanostructures by controlled in situ dissolution of a ZnO nanorod template: insights into the formation mechanism and thermal stability.* Nanoscale, 2016. **8**(3): p. 1462-1469.
43. An, K., et al., *Synthesis of Uniform Hollow Oxide Nanoparticles through Nanoscale Acid Etching.* Nano Letters, 2008. **8**(12): p. 4252-4258.
44. Khanal, A., et al., *Synthesis of Silica Hollow Nanoparticles Templated by Polymeric Micelle with Core−Shell−Corona Structure.* Journal of the American Chemical Society, 2007. **129**(6): p. 1534-1535.

45. Caruso, F., R.A. Caruso, and H. Möhwald, *Nanoengineering of Inorganic and Hybrid Hollow Spheres by Colloidal Templating.* Science, 1998. **282**(5391): p. 1111-1114.
46. Wirtz, M. and C.R. Martin, *Template-Fabricated Gold Nanowires and Nanotubes.* Advanced Materials, 2003. **15**(5): p. 455-458.
47. Kim, S.-W., et al., *Fabrication of Hollow Palladium Spheres and Their Successful Application to the Recyclable Heterogeneous Catalyst for Suzuki Coupling Reactions.* Journal of the American Chemical Society, 2002. **124**(26): p. 7642-7643.
48. Piquemal, J.-Y., et al., *One-step construction of silver nanowires in hexagonal mesoporous silica using the polyol process.* Materials Research Bulletin, 2003. **38**(3): p. 389-394.
49. Titirici, M.-M., M. Antonietti, and A. Thomas, *A Generalized Synthesis of Metal Oxide Hollow Spheres Using a Hydrothermal Approach.* Chemistry of Materials, 2006. **18**(16): p. 3808-3812.
50. Gilroy, K.D., et al., *Sacrificial Templates for Galvanic Replacement Reactions: Design Criteria for the Synthesis of Pure Pt Nanoshells with a Smooth Surface Morphology.* Chemistry of Materials, 2014. **26**(10): p. 3340-3347.
51. Prieto, M., et al., *Morphological Tunability of the Plasmonic Response: From Hollow Gold Nanoparticles to Gold Nanorings.* The Journal of Physical Chemistry C, 2014. **118**(49): p. 28804-28811.
52. Renu, P., et al., *Synthesis of Catalytically Active Porous Platinum Nanoparticles by Transmetallation Reaction and Proposition of the Mechanism.* Small, 2009. **5**(12): p. 1467-1473.
53. Li, X., et al., *Pure gold nanocages by galvanic replacement reaction of magnesium nanoparticles.* RSC Advances, 2014. **4**(3): p. 1185-1188.
54. Xie, S., et al., *Synthesis and Characterization of Pd@MxCu1−x (M=Au, Pd, and Pt) Nanocages with Porous Walls and a Yolk–Shell Structure through Galvanic Replacement Reactions.* Chemistry – A European Journal, 2012. **18**(47): p. 14974-14980.
55. Au, L., et al., *Synthesis and optical properties of cubic gold nanoframes.* Nano Research, 2008. **1**(6): p. 441-449.
56. Bastús, N.G., et al., *Synthesis of Highly Monodisperse Citrate-Stabilized Silver Nanoparticles of up to 200 nm: Kinetic Control and Catalytic Properties.* Chemistry of Materials, 2014. **26**(9): p. 2836-2846.
57. Xia, X., et al., *25th Anniversary Article: Galvanic Replacement: A Simple and Versatile Route to Hollow Nanostructures with Tunable and Well-Controlled Properties.* Advanced Materials, 2013. **25**(44): p. 6313-6333.
58. Dursun, A., D.V. Pugh, and S.G. Corcoran, *Dealloying of Ag-Au Alloys in Halide-Containing Electrolytes: Affect on Critical Potential and Pore Size.* Journal of The Electrochemical Society, 2003. **150**(7): p. B355-B360.
59. Sun, Y., B.T. Mayers, and Y. Xia, *Template-Engaged Replacement Reaction: A One-Step Approach to the Large-Scale Synthesis of Metal Nanostructures with Hollow Interiors.* Nano Letters, 2002. **2**(5): p. 481-485.
60. Rodrigues, T.S., et al., *AgPt Hollow Nanodendrites: Synthesis and Uniform Dispersion over SiO2 Support for Catalytic Applications.* ChemNanoMat, 2015. **1**(1): p. 46-51.
61. Gonzalez, E., et al., *Enhanced reactivity of high-index surface platinum hollow nanocrystals.* Journal of Materials Chemistry A, 2016. **4**(1): p. 200-208.
62. Jing, H. and H. Wang, *Structural Evolution of Ag–Pd Bimetallic Nanoparticles through Controlled Galvanic Replacement: Effects of Mild Reducing Agents.* Chemistry of Materials, 2015. **27**(6): p. 2172-2180.
63. Zhang, H., et al., *Facile Synthesis of Pd–Pt Alloy Nanocages and Their Enhanced Performance for Preferential Oxidation of CO in Excess Hydrogen.* ACS Nano, 2011. **5**(10): p. 8212-8222.
64. Cobley, C.M., D.J. Campbell, and Y. Xia, *Tailoring the Optical and Catalytic Properties of Gold-Silver Nanoboxes and Nanocages by Introducing Palladium.* Advanced Materials, 2008. **20**(4): p. 748-752.

65. Skrabalak, S.E., et al., *Gold Nanocages: Synthesis, Properties, and Applications.* Accounts of Chemical Research, 2008. **41**(12): p. 1587-1595.
66. Sun, Y., *Silver nanowires - unique templates for functional nanostructures.* Nanoscale, 2010. **2**(9): p. 1626-1642.
67. Sun, Y. and Y. Xia, *Triangular Nanoplates of Silver: Synthesis, Characterization, and Use as Sacrificial Templates For Generating Triangular Nanorings of Gold.* Advanced Materials, 2003. **15**(9): p. 695-699.
68. Hong, X., et al., *Single-Crystalline Octahedral Au–Ag Nanoframes.* Journal of the American Chemical Society, 2012. **134**(44): p. 18165-18168.
69. Sun, Y., et al., *Synthesis and Optical Properties of Nanorattles and Multiple-Walled Nanoshells/Nanotubes Made of Metal Alloys.* Journal of the American Chemical Society, 2004. **126**(30): p. 9399-9406.
70. Sun, Y. and Y. Xia, *Multiple-Walled Nanotubes Made of Metals.* Advanced Materials, 2004. **16**(3): p. 264-268.
71. Railsback, J.G., et al., *Size-Dependent Nanoscale Kirkendall Effect During the Oxidation of Nickel Nanoparticles.* ACS Nano, 2010. **4**(4): p. 1913-1920.
72. Liang, J., et al., *Fabrication of TiO2 hollow nanocrystals through the nanoscale Kirkendall effect for lithium-ion batteries and photocatalysis.* New Journal of Chemistry, 2015. **39**(4): p. 3145-3149.
73. Chee, S.W., et al., *Direct observation of the nanoscale Kirkendall effect during galvanic replacement reactions.* Nature Communications, 2017. **8**(1): p. 1224.
74. Yin, Y., et al., *Formation of Hollow Nanocrystals Through the Nanoscale Kirkendall Effect.* Science, 2004. **304**(5671): p. 711-714.
75. Moreau, L.M., et al., *How Ag Nanospheres Are Transformed into AgAu Nanocages.* Journal of the American Chemical Society, 2017. **139**(35): p. 12291-12298.
76. Bastús Neus, G., et al., *Exploring New Synthetic Strategies for the Production of Advanced Complex Inorganic Nanocrystals*, in *Zeitschrift für Physikalische Chemie*. 2015. p. 65.
77. Liu, X., et al., *Noble metal-metal oxide nanohybrids with tailored nanostructures for efficient solar energy conversion, photocatalysis and environmental remediation.* Energy & Environmental Science, 2017. **10**(2): p. 402-434.
78. Peter, R., P. Myriam, and L. Liang, *Core/Shell Semiconductor Nanocrystals.* Small, 2009. **5**(2): p. 154-168.
79. Nguyen, T., F. Mammeri, and S. Ammar, *Iron Oxide and Gold Based Magneto-Plasmonic Nanostructures for Medical Applications: A Review.* Nanomaterials, 2018. **8**(3): p. 149.
80. Feng, Y., et al., *Depletion sphere: Explaining the number of Ag islands on Au nanoparticles.* Chemical Science, 2017. **8**(1): p. 430-436.
81. Wu, B., et al., *Anisotropic Growth of TiO2 onto Gold Nanorods for Plasmon-Enhanced Hydrogen Production from Water Reduction.* Journal of the American Chemical Society, 2016. **138**(4): p. 1114-1117.
82. Zhang, X., Y. Liu, and Z. Kang, *3D Branched ZnO Nanowire Arrays Decorated with Plasmonic Au Nanoparticles for High-Performance Photoelectrochemical Water Splitting.* ACS Applied Materials & Interfaces, 2014. **6**(6): p. 4480-4489.
83. Ruibin, J., et al., *Metal/Semiconductor Hybrid Nanostructures for Plasmon-Enhanced Applications.* Advanced Materials, 2014. **26**(31): p. 5274-5309.
84. Quarta, A., et al., *Fluorescent-Magnetic Hybrid Nanostructures: Preparation, Properties, and Applications in Biology.* IEEE Transactions on NanoBioscience, 2007. **6**(4): p. 298-308.
85. Kelly, K.L., et al., *The Optical Properties of Metal Nanoparticles: The Influence of Size, Shape, and Dielectric Environment.* The Journal of Physical Chemistry B, 2003. **107**(3): p. 668-677.
86. Prodan, E., et al., *A Hybridization Model for the Plasmon Response of Complex Nanostructures.* Science, 2003. **302**(5644): p. 419-422.

87. Choi, Y., et al., *Galvanically Replaced Hollow Au–Ag Nanospheres: Study of Their Surface Plasmon Resonance.* Langmuir, 2012. **28**(16): p. 6670-6676.

Chapter 2

The Effect of Surfactants on the Formation of Hollow Complex Nanostructures

Noble metal hollow nanoboxes are among attractive nanostructures due to their exotic morphology and their optical properties. However to date, relatively little is known about the effect of surfactants. Consequently, in this chapter, the effect of different surfactants (CTAB, CTAC, CTApTS and PVP) on the production of hollow AgAu nanoboxes at room temperature is studied. In addition, the synthesis, characterization and possible mechanisms for the formation of AgAu hollow bimetallic nanostructures are presented.

2.1 Introduction

Hollow nanostructures have been of great interest mainly by their optical, electrical, thermal and catalytic properties [1]. These structural advantages make them potentially useful for applications in biomedical imaging [2, 3], controlled drug release [4], chemical sensing [5] and as photothermal agents [6] among others.

As previous studies show, while the shape of the resulting hollow nanostructure is defined by the starting template, wall thickness, composition, and porosity are controlled by the interfacial alloying and dealloying processes associated with the galvanic replacement reaction (GRR) [7-9]. It is also possible to create a variety of nanostructures with increasingly sophisticated interior and surfaces via the coupling of GRR with sequentially deposited templates [10-12], the Kirkendall effect [13, 14] or combined co-reduction and corrosion processes [15, 16]. For instance Wang and Jing show that the use of mild reducing agents such as ascorbic acid or formaldehyde, provide a pathway to tailor the geometries, both the interior structure as well as the roughness and porosity of the walls of AgPd bimetallic hollow nanostructures, enhancing the optical and catalytic properties of the resulting NPs [17].

Thus, GRR provides a simple and versatile route to transform less noble metallic solid NPs into more complex bimetallic hollow nanostructures with tuneable and well controlled properties [17]. The bimetallic hollow NPs forming through such galvanic replacements

exhibit optical properties that are highly mouldable in the visible and near-infrared regions, providing these NPs with great potential for photonic and biomedical applications [1, 2, 18].

Silver NPs with well-defined shapes, such as nanospheres, nanocubes, nanoprisms, nanorods and nanowires are commonly used as sacrificial templates for GRR. When a more noble metal precursor is used, these structures evolve to bimetallic nanoshells, nanocages, nanoframes and nanotubes, under appropriate conditions [1, 8, 14, 19]. In this way the templates define the overall shapes of the resulting hollow nanostructure.

The synthesis of silver nanocubes (Ag NCs) using several methods has been reported, including water based reduction from Ag precursor with CTAB [20], seed mediated synthesis [21], inhomogeneous nucleation strategy in a hydrophobic binary organic solvent [22] and polyol reduction [23]. Among these methods, polyol reduction provides the most reliable results in terms of monodispersity, yield and reproducibility [24].

Bimetallic hollow nanostructures, such as porous nanocages and nanoframes, are of particular interest for nanocatalysis because of their high surface-to-volume ratio, surface accessibility, nanocage confinement effects, and optimal use of the catalytic active metal [25-28]. Aditionally, the synthesis of metal nanostructures with plasmon absorption band around 1000 nm is strongly desired, especially for biomedical imaging and diagnostics [29, 30]. By changing the shape and composition of the NP, the surface plasmon absorption can be shifted into the NIR transmission window [31]. So far, Au nanocages obtained by GRR of Ag NCs with Au precursors, have been demonstrated to have plasmon absorptions band up to 900 nm [2]. Therefore the synthesis of bimetallic hollow nanostructures with plasmon bands beyond 900 nm is still a challenging area.

Based on the previous work of Gonzalez and co-authors [13] regarding the route for the production at room temperature of complex hollow nanostructures, in this chapter the effect of the surfactant on the synthesis of hollow nanostructures is studied with the aim of determining changes on morphology and optical properties. To this end, several surfactant agents including CTAB, CTAC, CTApTS and PVP were used for this purpose. The synthesis of bimetallic AgAu nanostructures with plasmon absorption band around 1000 nm is also presented.

2.2 Materials and methods

2.2.1 Materials

Ethyleneglycol anhydrous 99.8% (EG), silver trifluoroacetate (CF_3COOAg), polyvinylpyrrolidone (PVP, MW: 55,000; 360,000), hydrochloric acid 37% (HCl), sodium hydrosulfide (NaHS), ascorbic acid (AA), gold (III) chloride trihydrate >99,9% ($HAuCl_4 . 3H_2O$), sodium citrate tribasic dihydrate (SC), cetyltrimethylammonium bromide (CTAB), cetyltrimethylammonium chloride (CTAC), cetyltrimethylammonium *p*-toluenesulfonate (CTApTS), bovine serum albumin (BSA), Anti-BSA (bovine serum albumin) antibody, were purchased from Sigma-Aldrich. All chemicals were used as received without further purification. Distilled water passed through a Millipore system (ρ = 18.2 mΩ) was used in all experiments.

2.2.2 Methods

2.2.2.1 Synthesis of Ag NCs. Ag NCs were synthesized by a modified polyol method, briefly 15 mL of EG was added to a 100 mL round-bottomed flask, the flask was closed and then it was heated in a silicon oil bath at 150˚C. The reaction solution was continuously stirred using a magnetic stir bar. After 10 min, 180 μL of 3mM NaHS solution in EG was added. After 2 min, 1.5 mL of 3 mM HCl solution in EG and 3.8 mL of 20 mg/mL PVP were added. Finally after 3 min, 1.2 mL of 282 mM CF_3COOAg solution in EG was added. After 60 min, the reaction was stopped by placing the reaction flask in an ice-water bath. Resultant Ag NCs were purified by centrifugation (8000 g, 20 min) in order to remove the EG and the excess of PVP, and further dispersed in MQW before sample characterization.

2.2.2.2 Synthesis of AgAu hollow nanostructures. Bimetallic hollow AgAu nanostructures were synthesized via GRR and/or Kirkendall effect at room temperature. In a typical procedure, 0.25 mL of Ag NCs ($\sim 10^{12}$ NPs/mL) were dispersed in 1 mL of MQW, 1 mL of surfactant (CTAB, CTAC, CTApts 20 mM or PVP), and 0.1 mL of 1 mM AA, were added. Then, increasing amounts of $HAuCl_4$ (1 mM), was added through a syringe pump at a rate of 25 μL/min under constant stirring. After the addition of the $HAuCl_4$ solution, the reaction was stirred for about 30 min at room temperature until the UV–vis spectra of the solution became stable. The sample was centrifuged at 8000 g for 10 min and the supernatant was discarded. The pellet was suspended in 1 mL of MQW for further characterization.

2.2.2.3 Synthesis of AgAu hollow nanostructures with SPR band at 1000nm. In a typical procedure, 250 μL of Ag NCs (~10^{12} NPs/mL) were dispersed in 2 mL of PVP 20 mg/mL (180 mM by repeating unit) and 0.1 mL of AA 0.1 mM were added. Then, 250 μL of $HAuCl_4$ (1 mM), was added through a syringe pump at a rate of 10 μL/min under constant stirring. After the addition of the $HAuCl_4$ solution the reaction was stirred for 30 min at room temperature until the UV–vis spectra of the solution became stable. The sample was then centrifuged at 8000 g for 10 min and the supernatant was discarded. The pellet was suspended in 1 mL of MQW for further characterization.

2.2.2.4 Label-Free Sensing. A 0.9 mL aliquot of NPs (~10^{12} NPs/mL), spherical Au NPs or single-walled AgAu nanoboxes (PVP synthesized), dispersed in phosphate buffer 10 mM, were mixed with 0.1 mL of BSA (1 mM) in phosphate buffer and placed in an incubator at 37 °C for 48 h. After incubation of the NPs, the UV–vis spectra were acquired. Finally, 0.02 mL of a 2 mg/mL solution of anti-BSA was added to the incubated NPs and the UV–vis spectra were acquired.

2.2.2.5 Characterization

Absorption spectra of the as synthesized NPs were acquired with a Shimadzu UV-2401 PC or a Perkin Elmer Lambda 25 spectrophotometer. An aliquot of the NPs solution was placed in a cuvette, and spectral analysis was performed at room temperature.

The morphology and size of the NPs were visualized using FEI Magellan 400L XHR SEM, in transmission mode operated at 20 kV. TEM, HR-TEM, and STEM-HAADF images were obtained from a FEI Tecnai G2 F20 S-TWIN HR(S) TEM, operated at an accelerated voltage of 200 kV. A droplet of the sample was drop casted onto a piece of ultrathin carbon-coated 200-mesh copper grid (Ted-pella, Inc.) and left to dry in air. XRD data were collected on a PANalytical X'Pert diffractometer using a Cu Kα radiation source.

2.3 Results

In this study, the production of hollow AgAu nanoboxes was a two-step process. The first step involved the synthesis of monodisperse Ag NCs templates in high yield. In the second step, these Ag NCs were used as sacrificial template for the preparation of hollow AgAu nanostructures *via* GRR at room temperature.

2.3.1 Synthesis of Ag NCs. For the synthesis of Ag NCs a modified polyol method [24] was used (see methods for experimental details). **Figure 2.1A** shows TEM images of as synthesized monodisperse Ag NCs. There was a small fraction of by-products formed by Ag NPs with different morphologies such as nanorods and spheres. Size distribution analysis using over 200 particles from the TEM images shows that the mean length of the Ag NCs produced was 45.4 ± 5.1 nm, as depicted in **Figure 2.1C**. The UV-Vis absorption spectra of Ag NCs shown in **Figure 2.1C**, presents two distinctive bands, the small one at 350 nm from the out-of-plane quadrupole contribution, and the intense band at 440 nm corresponding to the dipole plasmon resonance mode. The small bump around 400 nm corresponds to the in-plane quadrupole mode [32, 33].

A photograph of a vial containing a diluted solution of Ag NCs is shown in **Figure 2.1D**, the yellow colour is characteristic for this type of morphology. **Figure 2.1E** shows the measured XRD patterns. Four diffraction peaks at 2θ values of 38˚, 44˚, 64˚, 76˚ and 82˚ are observed, corresponding to the (111), (200), (220), (311) and (222) planes respectively, which can be attributed to the fcc structure of Ag (JCPDS file No. 04-0783). The over dominance of the (200) peak in the XRD pattern confirms the flat faces of the NCs [34]. No diffractions peaks due to impurities, such as Ag precursor or Ag_2O were observed.

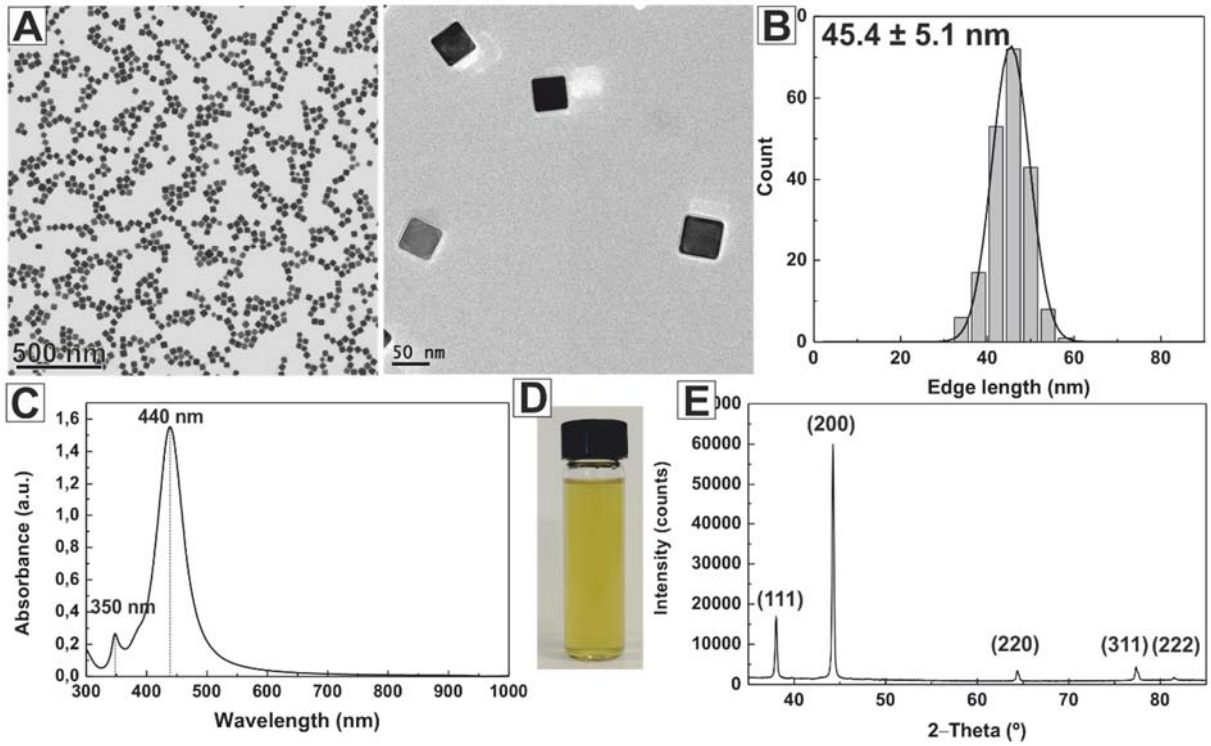

Figure 2.1 A. TEM images of Ag NCs. **B.** Particle size distribution of Ag NCs. **C.** UV-Vis spectrum of the as synthesized Ag NCs. **D.** Photograph of aqueous dispersion of Ag NCs. **E.** XRD patterns of Ag NCs.

2.3.2 Effect of the surfactant on the synthesis of AgAu hollow nanostructures. The obtained Ag NCs were used as sacrificial templates for the production of bimetallic AgAu hollow nanoboxes, *via* the GRR with $HAuCl_4$ as gold precursor, in the presence of ascorbic acid (AA) and different surfactants and/or stabilizers. AA a reductant that was used to avoid too aggressive Au^{+3} corrosion of the Ag NCs. The temperature at which the GRR take place plays an important role in the formation of bimetallic AgAu nanostructures, since the rate of the GRR, the roughness and porosity increases with temperature [35]. Thus, to have better control over the kinetic of the GRR and therefore the morphology of the products, room temperature was chosen for all the studies.

In a typical synthesis, the Ag NCs were dispersed in an aqueous solution of the surfactant and/or capping agent (the chemical structure of the surfactants and/or capping agent used in this study is presented in **Figure 2.2**) and AA, followed by the addition of an aqueous $HAuCl_4$ solution using a syringe pump. In contrast to the GRR used in previous studies [23, 36], the addition of AA allows the generation of $AuCl_2^-$ through the co-reduction of $AuCl_4^-$ inducing a

decrease in the etching power of Au^{+3} among other effects. To monitor the changes in morphology and composition in the course of the GRR, different amounts of $HAuCl_4$ were added and the products were characterized using TEM, HAADF-STEM, EDS analysis, and UV-vis spectroscopy.

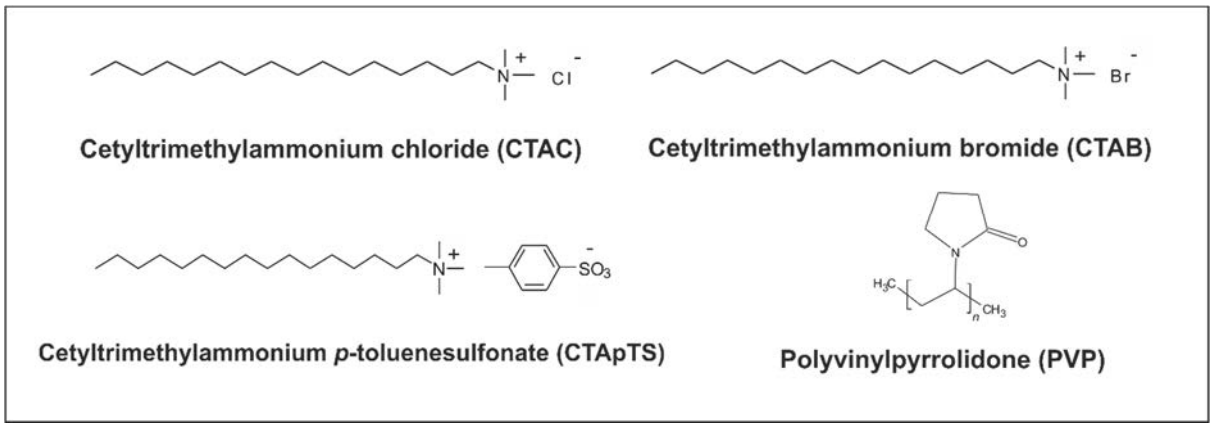

Figure 2.2. Chemical structures of the surfactants and capping agent employed in this study.

2.3.2.1 Effect of cationic surfactants. Here, the morphological evolution of hollow nanostructures using two halogenated surfactants is compared. CTAB and CTAC are well known cationic surfactants. CTAB is an effective capping agent for the production of Au NRs [37] and it has also been used for the synthesis of complex hollow nanostructures [13]. Additionally, a non-halogenated cationic surfactant (CTApTS) was used to understand the effect of the halogen on the final morphology of the nanostructure.

2.3.2.1.1 Effect of CTAB. The structural evolution of the Ag NCs through GRR in the presence of CTAB 20 mM was studied. When Ag NCs reacted with a substoichometric amount of $HAuCl_4$ (25 μL (1mM), 6.25×10^{-4} mmol) in the presence of AA and CTAB, a thin layer of Au was first deposited on the surface of the Ag NCs as described in **Figure 2.3A.** This layer can be explained by the fact that, after the addition of the Au precursor to the mixture of Ag NCs, CTAB and AA, some of the Au^{+3} ions turns immediately to Au^0 by the direct action of AA [38], while the GRR took place due to the remaining Au precursor [13, 39].

When more Au precursor was added (50 μL (1mM), 1.25×10^{-3} mmol), a pinhole was always observed on the centre of the face of the Ag NCs (**Figure 2.3B**), indicating that the reaction had been initiated locally at a preferred site rather than over the entire NC' surface. As the reaction proceeded, this small-hole gives access to the anode, where Ag is oxidized and

electrons are stripped. Then the released electrons migrated to the surrounding NC surfaces and were captured by $AuCl_4^-$ or $AuCl_2^-$. As the Au layer formed, the initial small-hole served as the site for Ag dissolution, facilitating the conversion of the solid Ag NCs into hollow nanostructures (**Figure 2.3C–E**). Higher amounts of $HAuCl_4$ solution (100 μL (1mM), 3.2×10^{-3} mmol) created double walled nanostructures (**Figure 2.4**), this was due to the combination of galvanic corrosion and Kirkendall effect. In this way, the NC morphology from core-shell, pinhole, and double walled could be controlled by the added amount of $HAuCl_4$ employed. The formation of double walled nanoboxes was previously reported by Gonzalez and co-workers [13] (see **Scheme 1**).

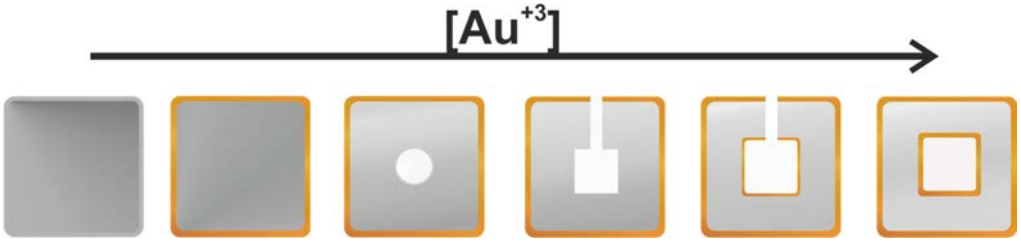

Scheme 1. Representation of the formation of bimetallic AgAu double walled nanoboxes in the presence of CTAB.

The optical properties of these AgAu hollow nanoboxes were studied by UV-vis spectroscopy and are shown in **Figure 2.3F.** When the amount of $HAuCl_4$ was increased, the SPR bands of the nanostructures were noticeably red-shifted from 440 nm for Ag NCs to 680 nm for double walled nanoboxes, indicating the surface plasmon resonance shift induced by the increasing of the content Au in the nanostructure, the void size and the wall thicknesses of the nanostructure [40]. By simply controlling the amount of Au precursor added into the reaction medium, the surface plasmon band of the nanostructures can be conveniently tuned over the broad spectral range.

The increase of the broadness in the absorption band due to the increases of the amount of gold precursor added to the reaction, can be explained because of the presence of by-products with different morphologies in the Ag templates. These undesired by-products, formed during the GRR, sinclude hollow nanorods, nanospheres or nanoprisms. There was also a small fraction of double walled nanoboxes of different size and single walled nanoboxes which were formed at the same time as the double walled nanoboxes, and can be clearly seen in TEM images of **Figure 2.3.**

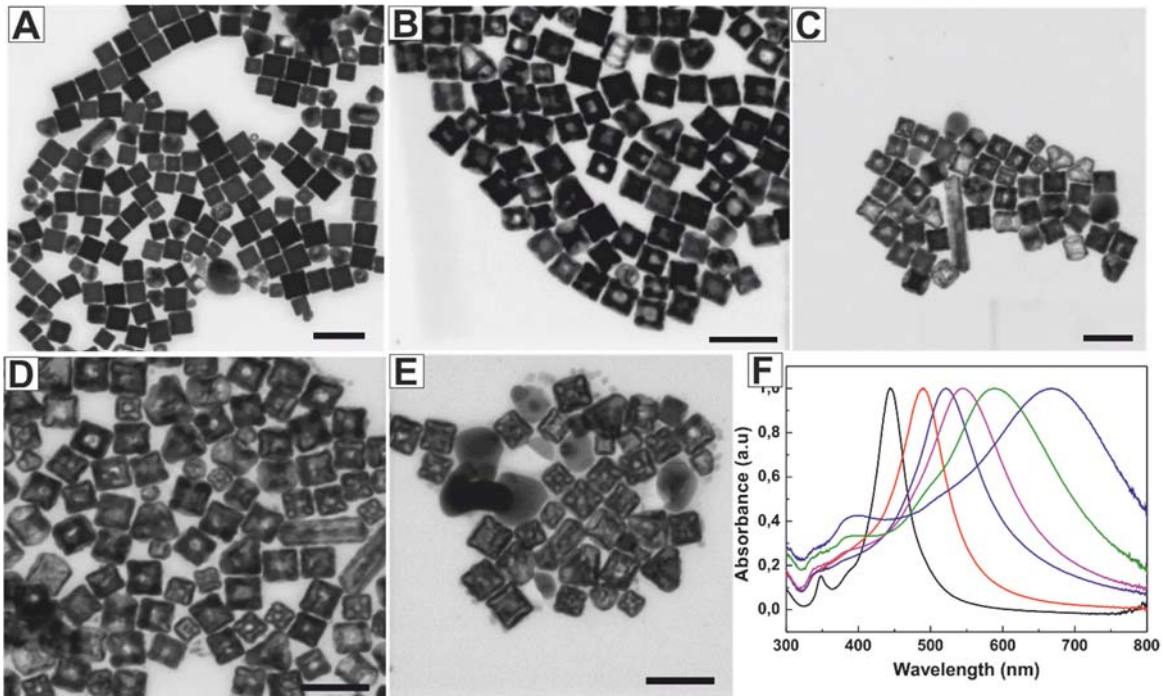

Figure 2.3. TEM images of AgAu NPs synthesized in the presence of CTAB with the addition of different amounts of $HAuCl_4$ 1mM. **A.** 25 μL (6.25×10^{-4} mmol) **B.** 50 μL (1.25×10^{-3} mmol) **C.** 75 μL (1.87×10^{-3} mmol) **D.** 100 μL (2.50×10^{-3} mmol) **E.** 125 μL (3.12×10^{-3} mmol). Scale bar represents 100 nm for all images. **F.** UV-Vis spectra of: black Ag NCs, red A, purple B, pink **C**, green **D** and blue **E**.

One of the interesting features of these bimetallic AgAu hollow nanostructures is that the colour of the colloidal solution of the NPs strongly depends on the degree of voiding which is directly related to the amount of $HAuCl_4$ added to the reaction. Thus, by adding different amounts of the $HAuCl_4$ 1mM solution into a fixed volume of Ag NCs in the presence of CTAB 20 mM, the colour of the solution slowly varies from yellow, dark yellow, orange, red, red-violet, purple, and finally blue as is shown in **Figure 2.4.**

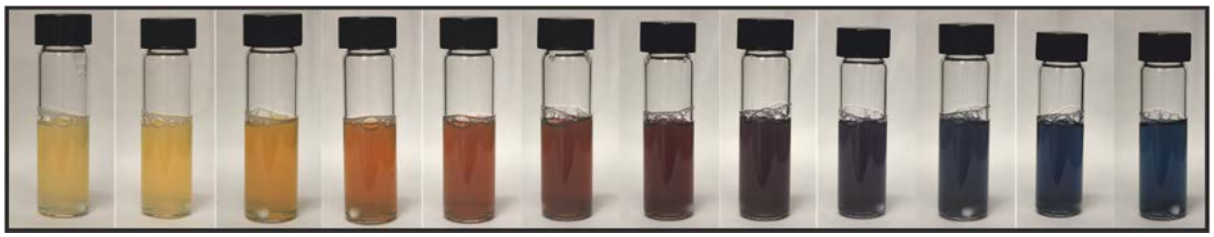

Figure 2.4. Variation of the colour with the amount of $HAuCl_4$ 1mM added into a fixed volume of Ag NCs in the presence of CTAB 20 mM.

As can be observed, **Figure 2.5A** shows TEM images of double walled nanoboxes, along with nanoboxes single walled nanoboxes. In the double walled nanoboxes the existence of a face centered inner cavity is clearly visible.

In **Figure 2.5B** Energy-dispersive X-ray spectroscopy (EDS) map of a double walled nanobox is presented, revealing almost homogeneous distribution of Ag (red) and Au (green) throughout the crystal. Quite different chemical compositions are observed during the quantification of individual spectrums. The outer wall had a composition of 36.2 ± 5.4 % Ag and 63.8 ± 5.4 % Au, whereas inner wall was composed of 24.1 ± 4.9 % Ag and 75.9 ± 4.9 % Au. Regions in the center and in between the walls had an overall composition of 37.5 ± 4.6 % Ag and 64.3 ± 4.55 % Au, which is quite similar to the values observed for the center parts of a single walled nanobox (**Figure 2.16**). Overall, the double walled nanobox had a chemical composition of 31.3 ± 7.9 % Ag and 68.7 ± 7.8 % Au, indicating the presence of about 6 % more Au compared to the single walled nanobox. It was noted that the size of the nanoboxes formed was larger than their precursor Ag NCs. The average length size of the obtained nanoboxes was 51.0 ± 4.7 nm (**Figure 2.5C**) which is 5.6 nm (12%) larger than the Ag NC templates. The wall thickness of the nanoboxes corresponded to 6.5 ± 1.2 nm (**Figure 2.5D**).

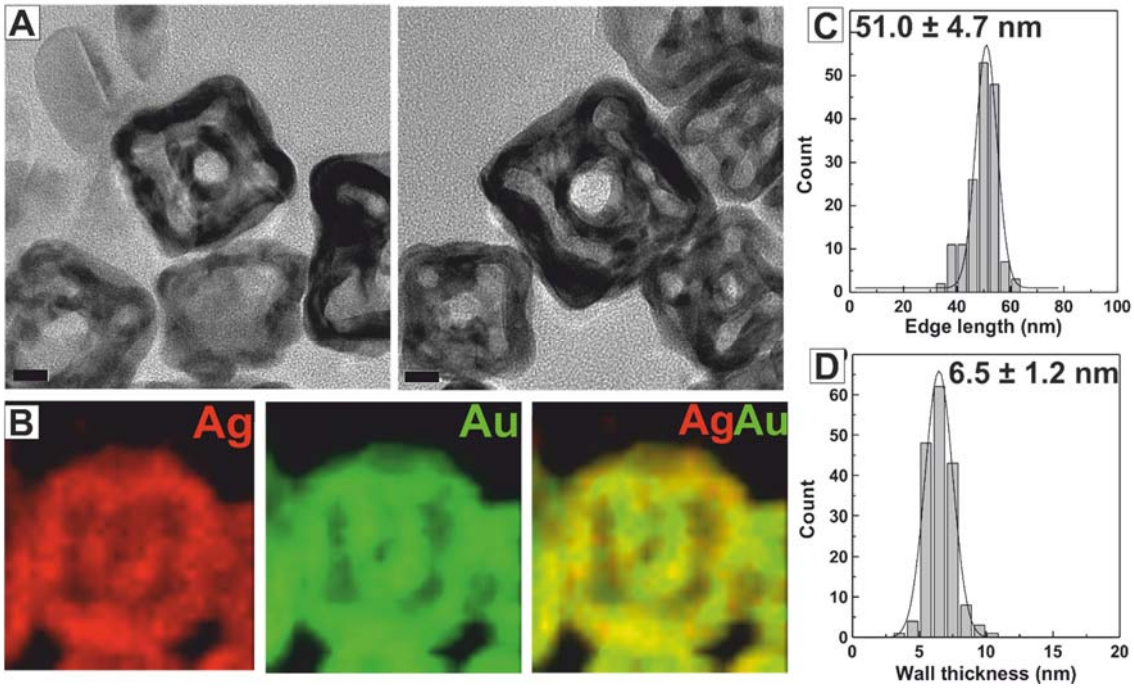

Figure 2.5. A. TEM images of double walled nanoboxes. Scale bar represents 10 nm for all images. **B.** EDS mapping of a double walled nanobox, Red for Ag, green for Au and composite **C.** Size distribution and **D.** Wall thickness distribution.

2.3.1.1.2. Effect of CTAB concentration. The effect of the CTAB concentration was also studied. **Figure 2.6** present TEM images of the obtained nanostructures, using four different concentrations of CTAB and keeping constant the amount of $HAuCl_4$ added to the reaction. As is shown in **Figure 2.6A-B**, when lower concentration of CTAB (0.20 – 2.0 mM) were used, the final product of the reaction correspond to fully corroded nanostructures formed by the agglomeration of small Au NPs or not well defined single walled nanoboxes due to the faster reduction of the gold precursor. Double walled nanoboxes were not present in the obtained products. Besides, when a CTAB concentration of 20 mM (**Figure 2.6C**) or superior (200 mM **Figure 2.6D**) was used, an improvement in the complexity of the resulting nanostructures was observed, and double walled nanoboxes were clearly visible. These results shows that the CTAB not only acts as stabilizer and complexing agent but also has and important effect on the formation of complex cavities in the NPs.

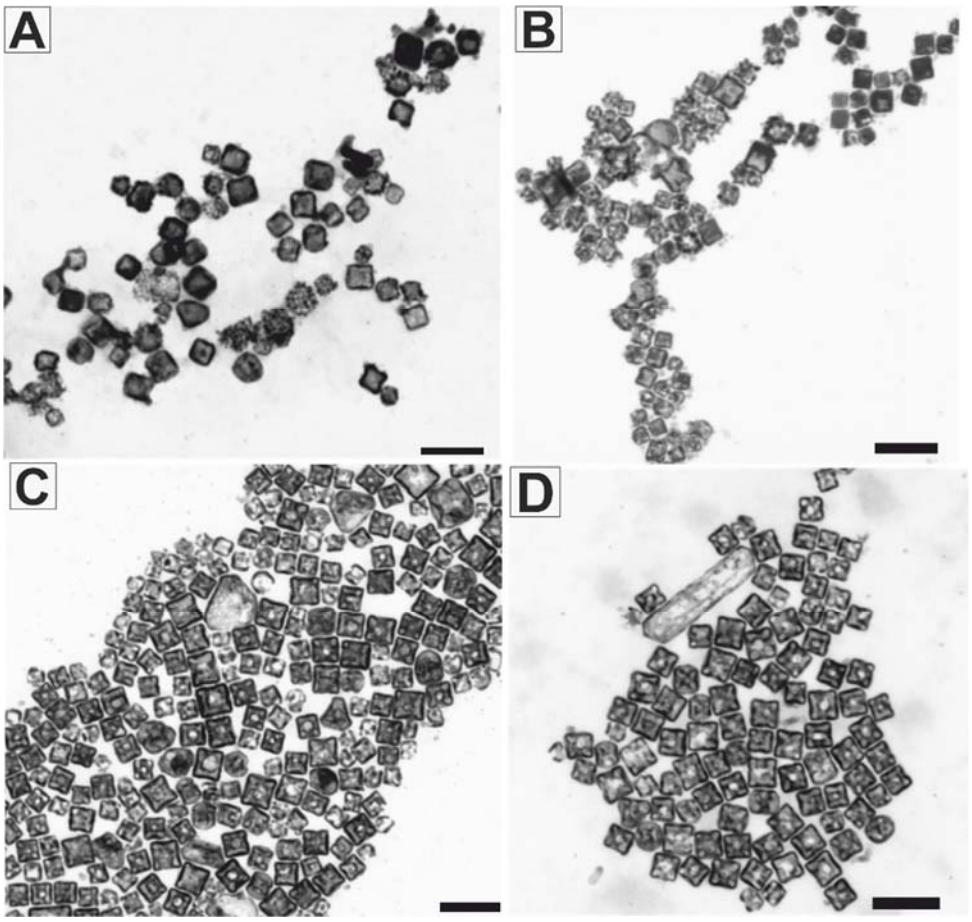

Figure 2.6. Effect of CTAB concentration. **A.** 0.20 mM **B.** 2.0 mM **C.** 20 mM and **D.** 200 mM. Scale bar 100 nm for all images.

2.3.1.1.3 Effect of CTAC. The effect in changing the anion in the surfactant from Br- to Cl on the GRR and on the morphology of the obtained nanostructures was then studied, with the use of CTAC instead of CTAB, while all the other experimental parameters were kept the same.

The optical and morphological evolution of the GRR was quite similar that in the case when CTAB was used as stabilizer, however, some differences are observed, especially in the first steps of the reaction as is displayed in **Scheme 2.**

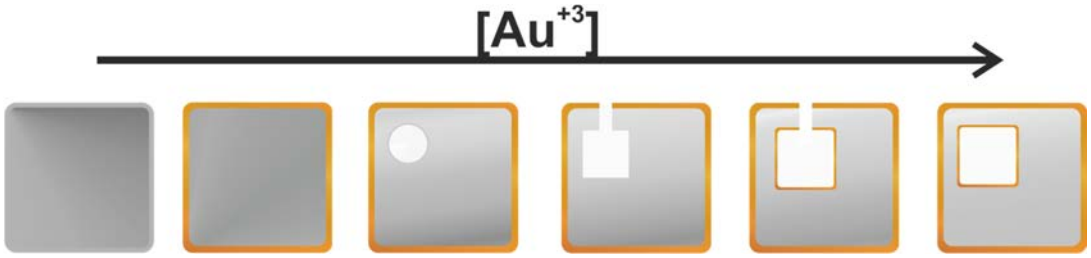

Scheme 2. Representation of the formation of bimetallic AgAu double walled nanoboxes in the presence of CTAC.

The morphological evolution of the Ag NCs templates with increasing amounts of $HAuCl_4$ added to the reaction media is shown in **Figure 2.7.** When a certain amount of gold precursor is added (50 μL (1mM), 1.25×10^{-3} mmol), a pinhole was observed on the face of the Ag NCs (**Figure. 2.7A**). The main difference when CTAB was used is that this pinhole was randomly situated on the face of the Ag NCs, especially on the centre of the face, but the pinhole is randomly situated on the face of the Ag NCs, especially on the centre of the edge or in the corner of the Ag NC, rather than in the centre of the Ag NC face (**Figure 2.9A**). The optical properties of the synthesized AgAu nanoboxes were studied by using Uv-vis spectroscopy (**Figure 2.7E**) the SPR peak red-shift from 440 nm until 650 nm as a function of the addition of different amounts of $HAuCl_4$ solution ($6.25x10^{-4}$ mmol – 3.12×10^{-3} mmol) into a fixed volume of Ag NCs. As explained before, this red-shift is due to the increasing of the content Au in the nanostructure and the increase of void size. In the same way as in the case of CTAB, the broadness of the band is caused by the formation of different products during the reaction such as single, double or multi walled nanoboxes, as well as the presence of different morphologies.

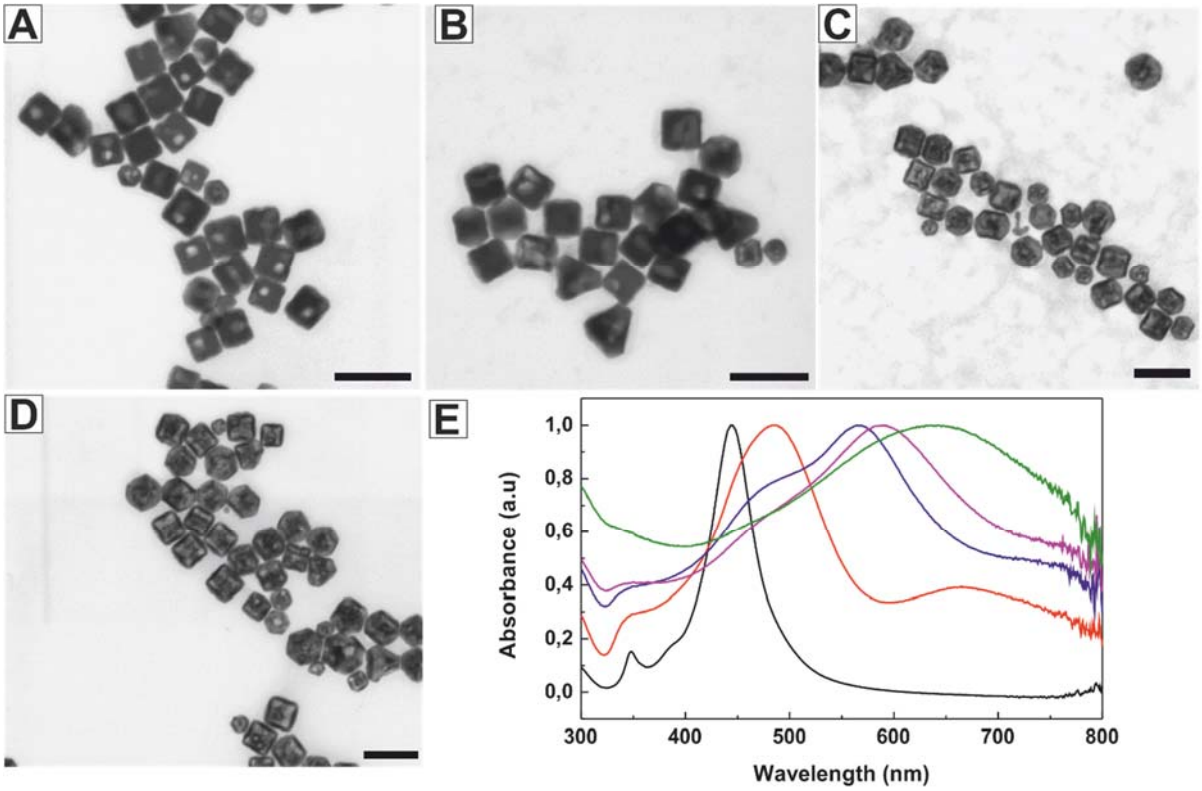

Figure 2.7 TEM images of AgAu NPs synthesized in the presence of CTAC 20 mM with the addition of different amounts of $HAuCl_4$ 1mM. Insets shows photographs of the colloidal suspension of NPs **A.** 50 μL (1.25×10^{-3} mmol) **B.** 75 μL (1.87×10^{-3} mmol) **C.** 100 μL (2.50×10^{-3} mmol) **D.** 125 μL (2.50×10^{-3} mmol). Scale bar represents 100 nm for all images. **E.** UV-Vis spectra of: black Ag NCs, red A, blue B, purple C, and green D.

After the addition of different amounts of $HAuCl_4$ 1mM into a fixed volume of Ag NCs in the presence of CTAC 20 mM, the colour of the solution varies from yellow, orange, red, purple, and finally blue as is shown **Figure. 2.8.**

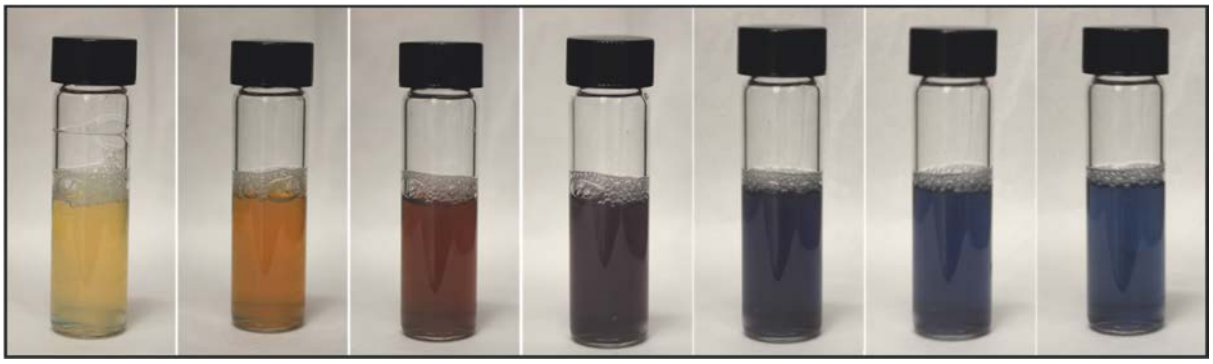

Figure 2.8 Variation of the colour with the amount of $HAuCl_4$ 1mM added to into a fixed volume of Ag NCs in the presence of CTAC 20 mM.

As can be observed, **Figure 2.9B** shows EDS maps of a single pinhole NC, which shows that Au is homogeneously located in all the NP. An outer layer of 4nm which was formed in the first steps of the reaction is clearly visible in the composite map (**Figure 2.7B**, bottom left). It should be noted that the pinhole is located in the corner of the face of the Ag NC.

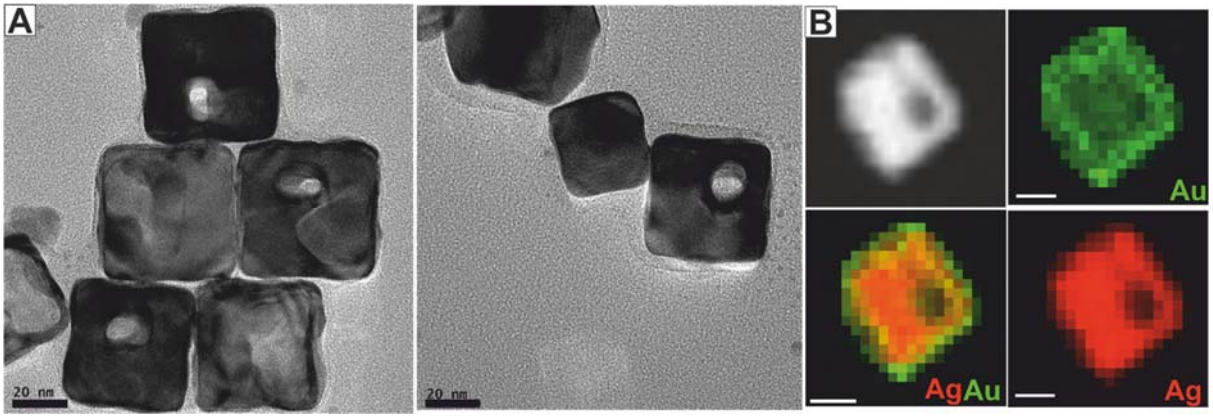

Figure 2.9. A. TEM images of pinholed NCs obtained when CTAC was used. **B**. HAADF-STEM image, EDS mapping of a pinholed NC, Red for Ag, green for Au and composite.

Sometimes, more than one pinhole is observed, as shown in **Figure 2.10A.** The EDS line scanning (**Figure 2.10B**) through the blue arrow shows that the NP was composed of Ag and Au and, at this stage of the GRR, Ag was more abundant than Au. Both pinholes are also clearly visible in the HAADF-STEM image and as well as in the EDS profile by the drop on the Ag EDS signal.

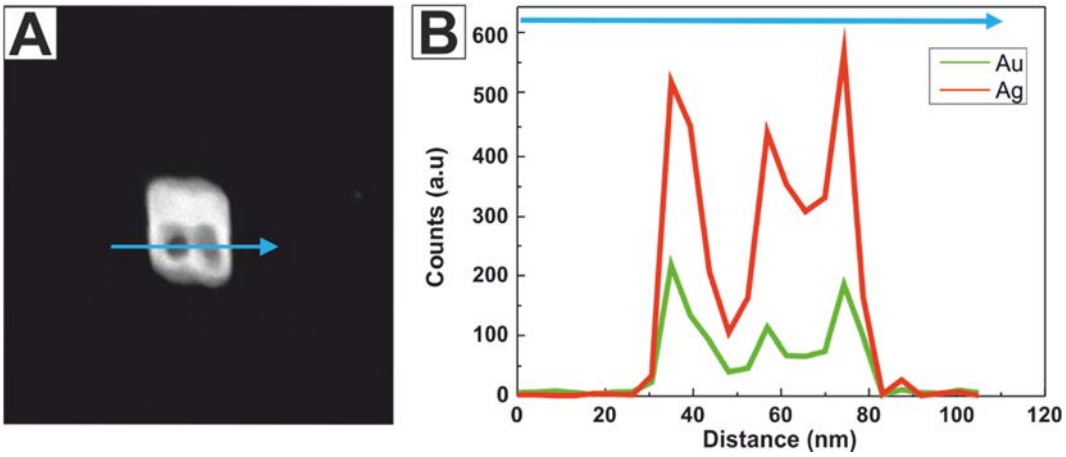

Figure 2.10 A. HAADF-STEM image of a two pinholed NC. **B.** EDS line scanning through the blue arrow of the double pinholed NC presented in **A.**

Higher amounts of $HAuCl_4$ solution (3.2×10^{-3} mmol) created double walled nanoboxes along with single walled nanoboxes (**Figure 2.11**). Is important to highlight, that the inner cage is not centred as in the case of CTAB, and its position corresponds to the initial position of the pinhole. In the case of more than one pinhole, it is possible to observe multi chambered nanoboxes. The EDS maps of a double walled nanobox (**Figure 2.11B**) reveal a homogeneous distribution of Ag and Au throughout the NP. The average length of the obtained nanoboxes was 54.2 ± 4.3 nm (**Figure 2.11C**) with a wall thickness of 7.0 ± 1.4 nm (**Figure 2.11D**) almost the same size as the nanoboxes obtained with CTAB. In this way, the morphology from pinholed to multichambered nanostructures can be controlled by tuning the added amount of $HAuCl_4$ in the presence of CTAC.

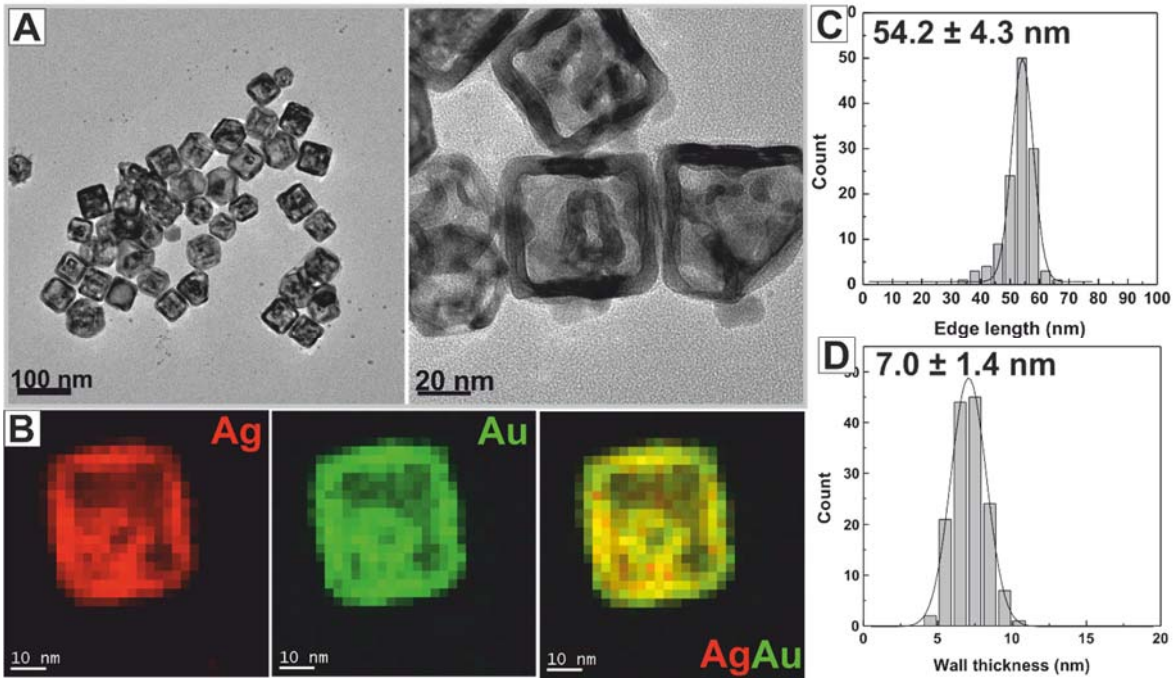

Figure 2.11. A. TEM images of double walled nanoboxes obtained when CTAC was used as surfactant. **B.** EDS mapping of a double walled nanobox, red for Ag, green for Au and composite. **C.** Size distribution and **D.** Wall thickness distribution.

The EDS line scanning (**Figure 2.12**) through the orange and blue arrows shows that the nanobox is composed by Ag and Au. A homogeneous gold distribution can be observed through the NP, indicating that it was composed by an AgAu alloy.

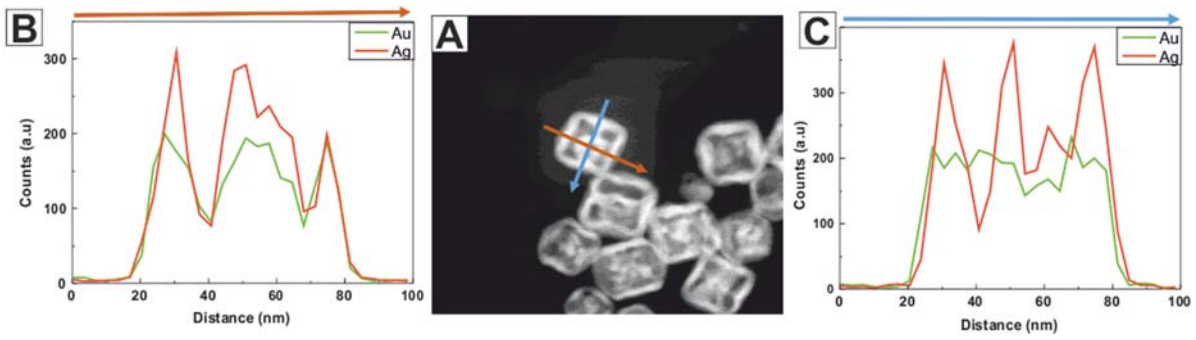

Figure 2.12. A. HAADF-STEM image of double walled nanoboxes obtained in the presence of CTAC. **B.** EDS line scanning through the orange arrow of nanostructure presented in A. **C.** EDS line scanning through the blue arrow of nanostructure presented in A.

2.3.2.1.4 Effect of a non-halogenated cationic surfactant. The effect of a non-halogenated cationic surfactant in the GRR of Ag NCs with $HAuCl_4$ solution was studied. In this case an organic anion, *p*-toluenesulfonate, was chosen because of its water solubility. The main difference between CTApTS and halogenated surfactants is that, when a certain amount of Au precursor was added (50 μL (1mM), 1.25×10^{-3} mmol), the characteristic pinhhole was not observed in the resulting nanostructures (**Figure 2.13A**), suggesting that the galvanic corrosion occurs very fast during the first stages of the reaction, as can be confirmed by the presence of single walled and partially corroded nanoboxes. When more Au precursor was added, the presence of single walled nanoboxes increases. See **Scheme 3.**

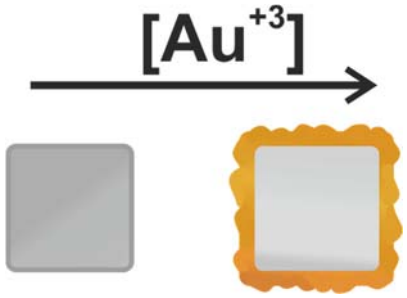

Scheme 3. Representation of the formation of bimetallic AgAu double walled nanoboxes in the presence of CTApts.

By adding different amounts of the $HAuCl_4$ solution ($6.25\text{x}10^{-4}$ mmol – 3.12×10^{-3} mmol) into a fixed volume of Ag NCs, the colour of the solution varies from yellow to purple, and finally blue as show in the insets in **Figure 2.13A-D**. The evolution of the UV-Vis spectra with the addition of different amounts of Au precursor is shown in **Figure 2.13D**. When small volumes of Au precursor were added, the SPR band present a redshift until ~550nm (red and

blue line in **Figure 2.13D**), when more gold precursor was added, the spectra became a flat line with a small bump around ~750nm. This change in the absorption spectra is due to the aggregation of the resulting nanostructures.

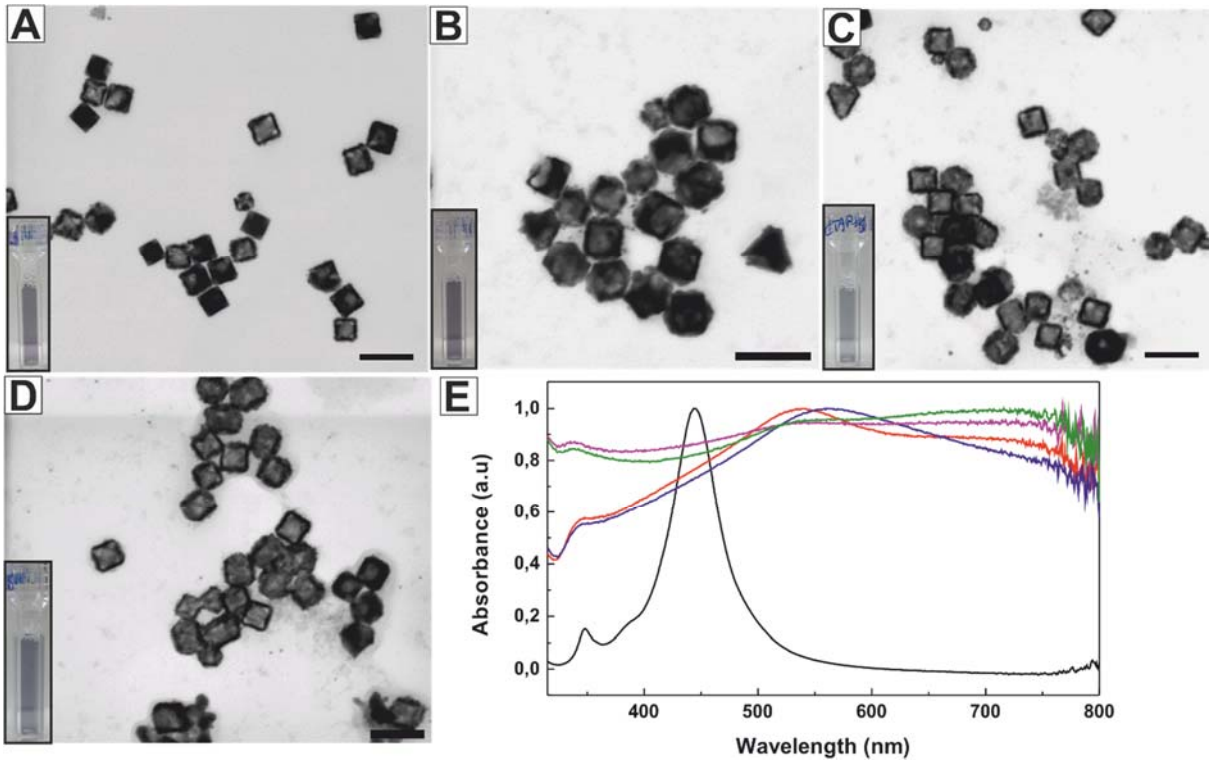

Figure 2.13. TEM images of AgAu NPs synthesized in the presence of CTApTS 20mM with the addition of different amounts of $HAuCl_4$ 1mM. Photographs showing the colloidal suspension of NPs are presented as insets. **A.** 50 μL (1.25×10^{-3} mmol) **B.** 75 μL (1.87×10^{-3} mmol) **C.** 100 μL (2.50×10^{-3} mmol) **D.** 125 μL (2.50×10^{-3} mmol). Scale bar represents 100 nm for all images. **E.** UV-Vis spectra of: black Ag NCs, red A, blue B, purple C, and green D.

As mentioned before, when CTApTS was used as surfactant, single walled nanostructures (**Figure 2.14A**) with irregular thick walls were obtained and, the average edge size of these nanoboxes corresponded to 53.1 ± 5.0 nm and a wall thickness of 8.3 ± 1.7 nm as is shown in **Figure 2.14B-C** respectively.

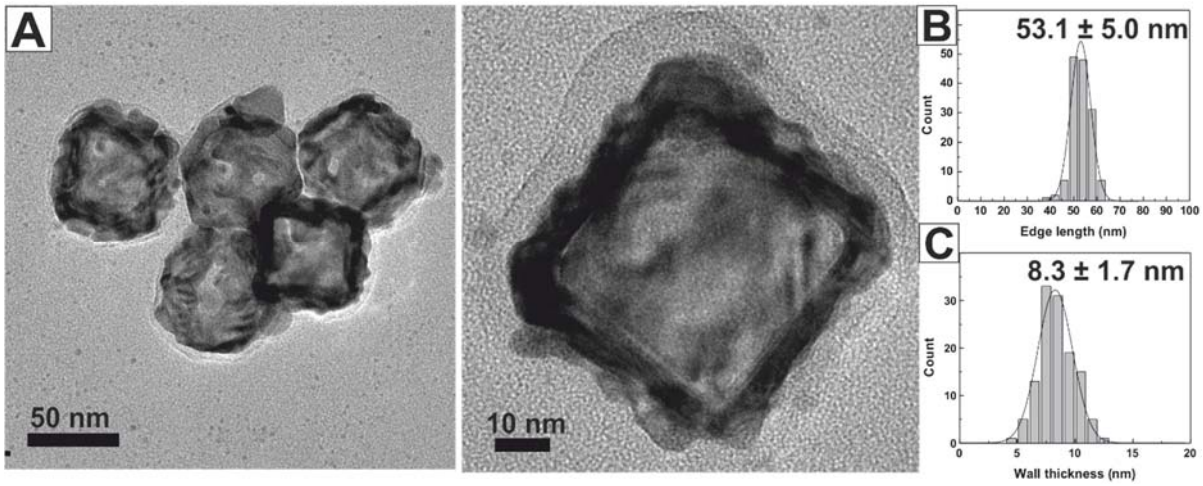

Figure 2.14 A. TEM images of single walled nanoboxes synthesized in the presence of CTApTS. **B.** Size distribution and **C.** Wall thickness of single walled nanoboxes.

It would appear that the presence of halogens provided by the surfactant, forms a layer of AgBr or AgCl on the surface of the Ag NCs, protecting them from fast corrosion and modifying the kinetics of the reaction. In this context, the potential presence of AgBr or AgCl at the surface of the Ag template, together with the surfactants, can produce a physical barrier which would avoid fast galvanic corrosion, controlling the diffusion of the Au precursor, favouring the diffusion due to the Kirkendall effect and the formation of complex nanostructures.

2.3.2.2 Effect of non-ionic stabilizer. The effect of a non-ionic stabilizer was then studied. PVP was chosen because it is widely used as stabilizing and shape-directing agent in the synthesis of noble metal NPs [41].

First, the effect of the concentration of PVP was studied. For this purpose, PVP of MW 55,000 was used at different concentrations (by repeating unit), and the same amount of Au precursor was added in all cases as is shown in **Figure 2.15.**

When PVP was not used (**Figure 2.15A**) sponge like nanostructures were formed, this was due to the fast oxidation of the Ag template together with the fast deposition of Au. When the concentration of PVP was fixed to 0.01 mM, a mixture between the sponge like nanostructures and single walled nanoboxes were obtained, where the amount of the sponge like nanostructures was very low. When PVP concentration was adjusted to 0.1 and 1 mM (**Figure 2.15C-D**) just single walled nanoboxes were observed. Finally, when higher PVP

concentrations, 10 mM and 100 mM were used (**Figure 2.15 E-F**) a mixture between single walled nanoboxes and nanostructures partially corroded (see HAADF-STEM insets images in **Figure 2.15 E-F**), where considerable amounts of Ag were still present, were obtained. The formation of these partially corroded nanostructures could be explained because the PVP binds to the surface of Ag NCs and acts as a physical barrier for the Au precursor deposition-reduction and decreases the kinetic of the GRR. In **Figure 2.15G** we can see than the SPR band of the nanostructures synthesized in high PVP concentrations appears at lower values (670 nm) than in the case of lower concentrations (up to 700 nm), this is due to the presence of this not fully corroded nanostructures mentioned before.

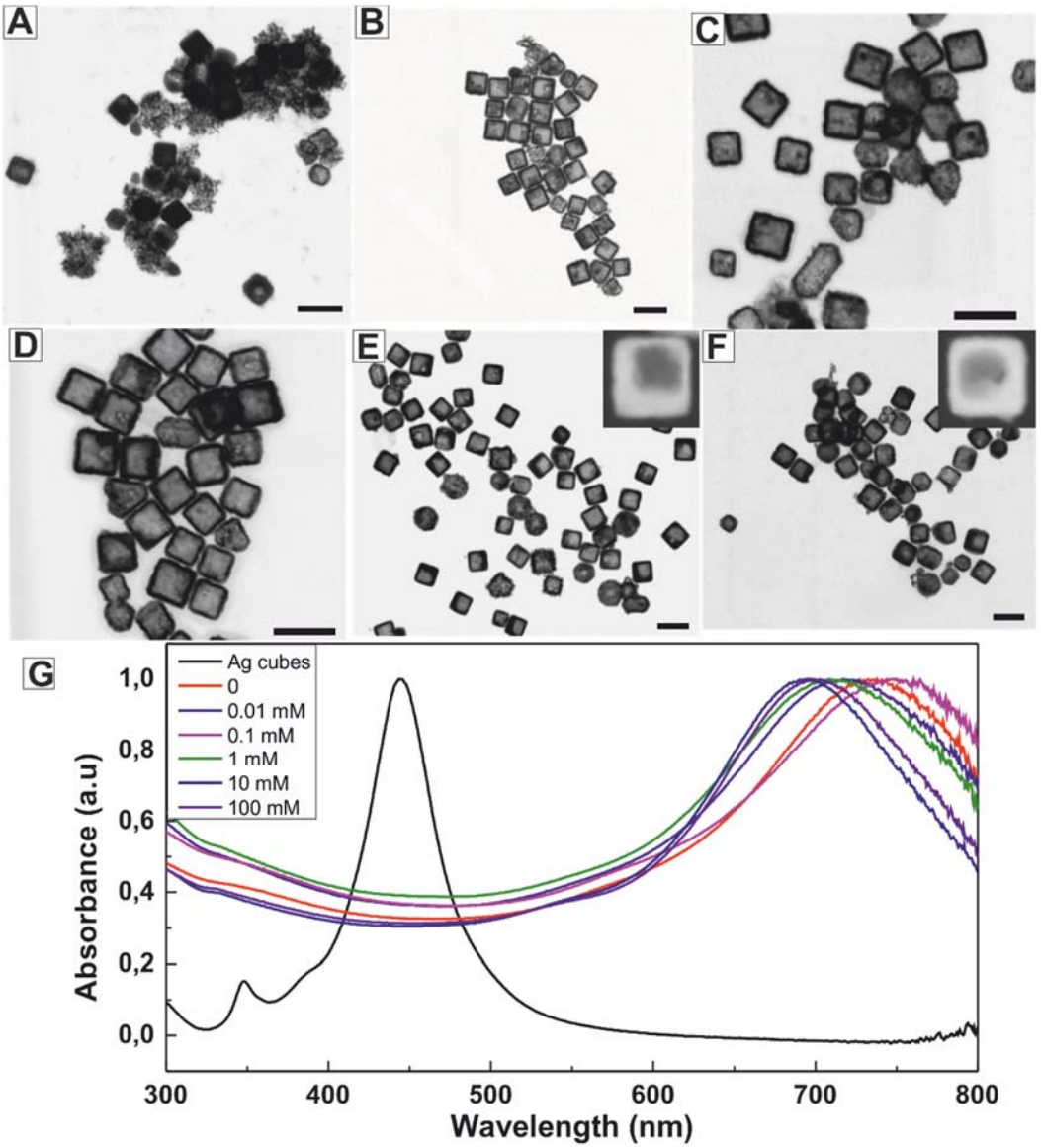

Figure 2.15. Effect of PVP concentration (by repeating unit). **A.** without **B.** 0.01 mM **C.** 0.1 mM **D.** 1 mM. **E.** 10 mM **F.** 100 mM. Scale bar 100 nm for all images. **G**. UV-Vis spectra.

TEM images of single walled nanoboxes are shown in **Figure 2.16A.** These nanoboxes were synthesized in the presence of PVP (1 mM, by repeating unit). The monodispersity and homogenity of the product is clearly visible. EDS analysis of a single walled nanobox is shown in **Figure 2.16B.** As can be observed, the distribution of Ag (red) and Au (green) in the single walled nanobox seems to be almost homogeneous throughout the nanostruture. Quantification of different spectra from the wall and inner part of the nanobox also suggested overall homogenity. The wall was composed of 37.8 ± 6.2 % Ag and 62.2 ± 6.2 % Au, and the inner part was composed of 36.2 ± 9.2 % Ag and 63.8 ± 9.2 % Au. Since both the walls and inner parts had similar chemical composition, it is convenient to present them as an overall result, which is 37.8 ± 7.1 % Ag and 62.2 ± 7.1 % Au.

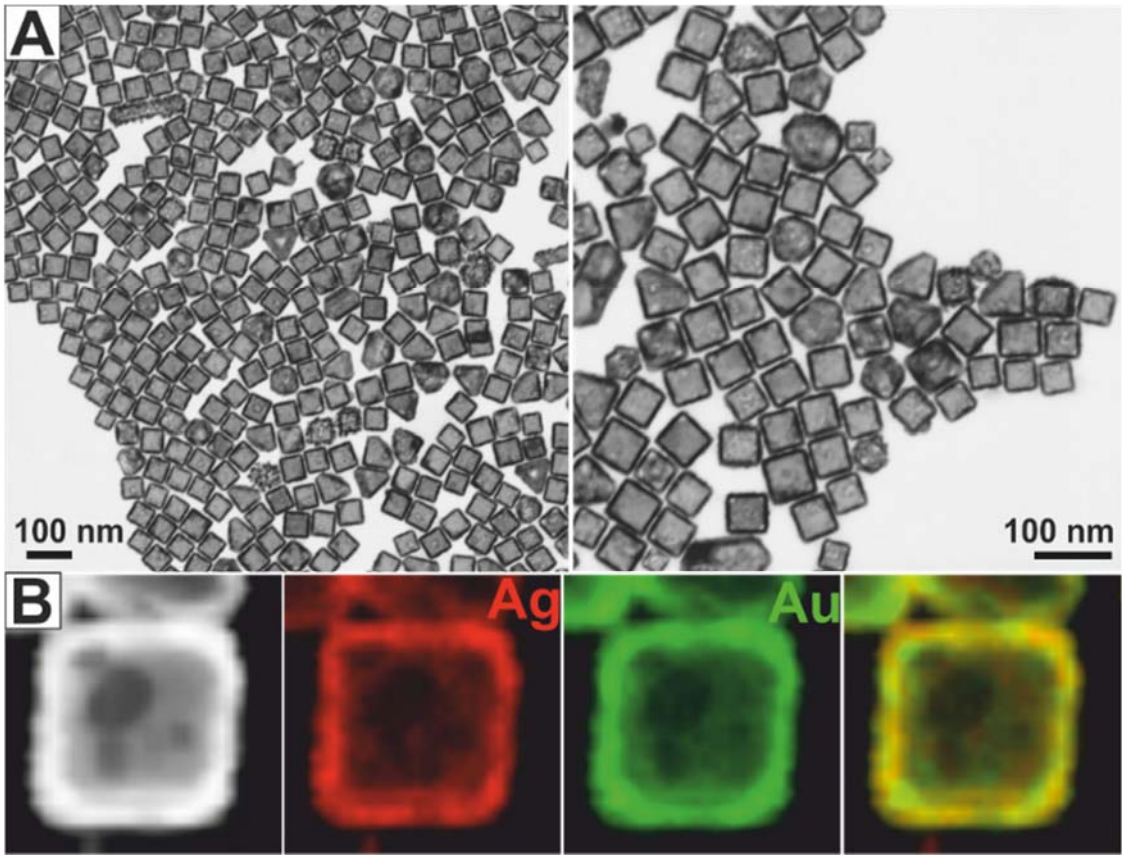

Figure 2.16. A. TEM images of single walled nanoboxes synthesized in the presence of PVP. **B.** HAADF-STEM image and EDS mapping of a single walled nanobox, red for Ag, green for Au and composite.

By using even higher concentrations of PVP (180 mM by repeating unit, 20 mg/mL), along with the slow addition of the Au precursor (10 μL/min) it was possible to obtain highly porous nanoboxes, resulting from the dealloying and dissolution of Ag from the nanoboxes

wall, as is shown in **Figure 2.17A.** These nanostructures present a strong SPR band in the near IR region at ~1000 nm (**Figure 2.17B**). These NPs have great potential for biomedical applications [42] as a contrast agent for photoacoustic tomography [43], or in photothermal therapy [31].

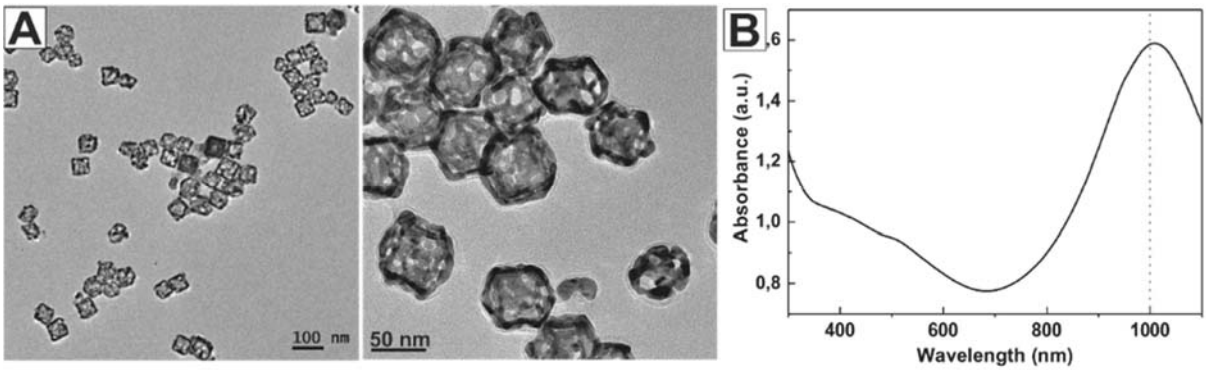

Figure 2.17 A. TEM images **B.** UV-Vis spectra of as synthesized nanostructures.

As is shown in **Figure 2.18,** selected TEM tilt images of the same nanobox showing different perspectives with tilting the sample from +50° to −45° and confirm the highly porous morphology of the nanoboxes.

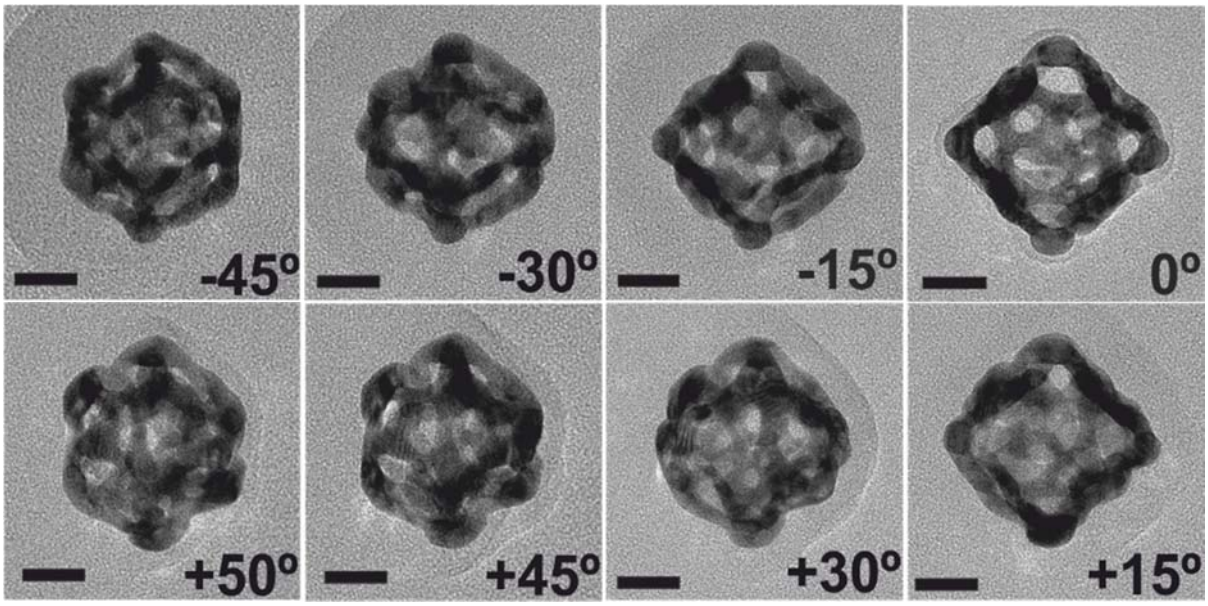

Figure 2.18. TEM, images of the same nanobox tilted -45°, -30°, -15°, 0°, 15°, 30°, 45°, and 50°. Scale bar represent 20 nm for all images.

2.3.3. Biosensing with single walled nanoboxes. The binding of antibodies to a protein corona [44] formed on single-walled AuAg nanoboxes or on 50 nm spherical Au NPs as a benchmark [45] for comparison was detected. It is well-known that when the NPs are dispersed in physiological media, they are immediately coated by proteins, forming a protein corona that may harden with time [46], and become a hard protein shell that provides the biological identity [47] of the NP. In this regard BSA [44] is one of the major compound. **Scheme 4** shows the representation of the primary (with BSA) and secondary (with anti-BSA) protein conjugation processes with spherical solid Au NPs (**Scheme 4A)** and single walled nanoboxes (**Scheme 4B)**, where the coverage of nanostructures with BSA and further attachment of antibodies are illustrated.

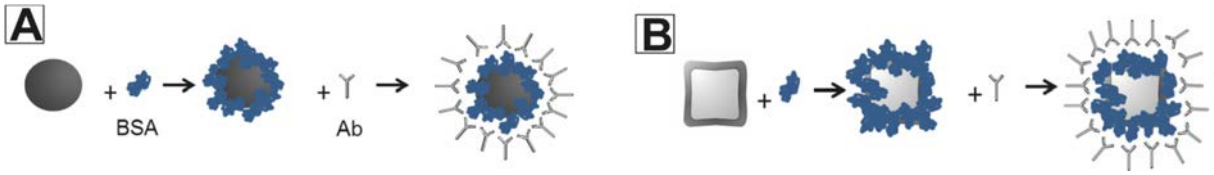

Scheme 4. A. Schematic representation of the primary and secondary protein conjugation processes with **A.** spherical Au NPs and **B.** single walled nanoboxes.

The UV–visible spectra from the unconjugated Au NPs (**Figure 2.19A**) and single-walled AgAu nanoboxes (**Figure 2.19B**) along with their response to the BSA conjugation are shown in **Figure 2.19**. As can be seen in these UV–vis spectra, after incubation with BSA (shown in red), the position of the LSPR peak of spherical Au NPs does not change much (about 4 nm), whereas the shift in the LSPR peak of the AgAu nanoboxes is clearly visible (about 12 nm). Similar differences between the Au-BSA NPs and single-walled AgAu-BSA nanoboxes are also observed during the second conjugation event when incubated with antibodies against BSA (shown in blue). Overall, it can be clearly seen in **Figure 2.19C** that shifts for the single walled nanoboxes are about 4 times stronger than the Au NPs, especially in the second binding event, thanks to the enhancement of the localized electromagnetic field around the hollow nanoboxes that allows easy and direct detection of binding events in their vicinity.

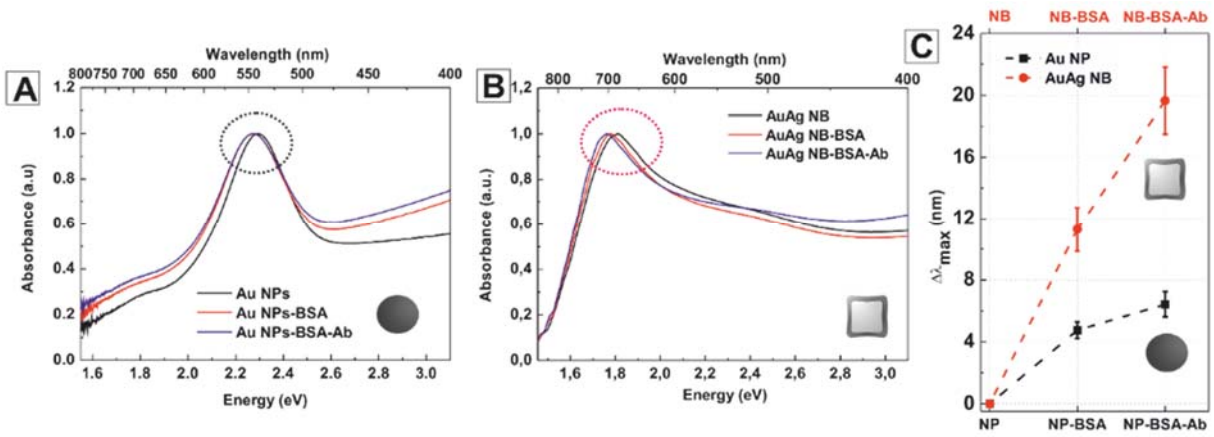

Figure 2.19. The UV–visible spectra from the unconjugated Au NPs (**A**) and single-walled nanoboxes (**B**) along with their response to the BSA conjugation and after the further addition of the Ab (blue line). Insets on A and B are plotted in **C**, which is the redshift comparison between Au NPs and single-walled nanoboxes after the first NP–protein interaction and secondary protein–Ab interaction.

2.4 References

1. Skrabalak, S.E., et al., *Gold Nanocages: Synthesis, Properties, and Applications.* Accounts of Chemical Research, 2008. **41**(12): p. 1587-1595.
2. Xia, Y., et al., *Gold Nanocages: From Synthesis to Theranostic Applications.* Accounts of Chemical Research, 2011. **44**(10): p. 914-924.
3. Wang, Y., et al., *Radioluminescent Gold Nanocages with Controlled Radioactivity for Real-Time in Vivo Imaging.* Nano Letters, 2013. **13**(2): p. 581-585.
4. Yavuz, M.S., et al., *Gold nanocages covered by smart polymers for controlled release with near-infrared light.* Nat Mater, 2009. **8**(12): p. 935-939.
5. Mahmoud, M.A., D. O'Neil, and M.A. El-Sayed, *Hollow and Solid Metallic Nanoparticles in Sensing and in Nanocatalysis.* Chemistry of Materials, 2014. **26**(1): p. 44-58.
6. Wang, L., et al., *Near-IR-Absorbing Gold Nanoframes with Enhanced Physiological Stability and Improved Biocompatibility for In Vivo Biomedical Applications.* ACS Applied Materials & Interfaces, 2017. **9**(4): p. 3873-3884.
7. Cobley, C.M. and Y. Xia, *Engineering the properties of metal nanostructures via galvanic replacement reactions.* Materials Science and Engineering: R: Reports, 2010. **70**(3–6): p. 44-62.
8. Sun, Y. and Y. Xia, *Alloying and Dealloying Processes Involved in the Preparation of Metal Nanoshells through a Galvanic Replacement Reaction.* Nano Letters, 2003. **3**(11): p. 1569-1572.
9. Xia, X., et al., *25th Anniversary Article: Galvanic Replacement: A Simple and Versatile Route to Hollow Nanostructures with Tunable and Well-Controlled Properties.* Advanced Materials, 2013. **25**(44): p. 6313-6333.
10. Sun, Y. and Y. Xia, *Mechanistic Study on the Replacement Reaction between Silver Nanostructures and Chloroauric Acid in Aqueous Medium.* Journal of the American Chemical Society, 2004. **126**(12): p. 3892-3901.

11. Khalavka, Y., J. Becker, and C. Sönnichsen, *Synthesis of Rod-Shaped Gold Nanorattles with Improved Plasmon Sensitivity and Catalytic Activity.* Journal of the American Chemical Society, 2009. **131**(5): p. 1871-1875.
12. Xiong, W., et al., *Single-crystal caged gold nanorods with tunable broadband plasmon resonances.* Chemical Communications, 2013. **49**(83): p. 9630-9632.
13. González, E., J. Arbiol, and V.F. Puntes, *Carving at the Nanoscale: Sequential Galvanic Exchange and Kirkendall Growth at Room Temperature.* Science, 2011. **334**(6061): p. 1377-1380.
14. Gonzalez, E., et al., *Enhanced reactivity of high-index surface platinum hollow nanocrystals.* Journal of Materials Chemistry A, 2016. **4**(1): p. 200-208.
15. Yang, Y., et al., *Transformation of Ag Nanocubes into Ag–Au Hollow Nanostructures with Enriched Ag Contents to Improve SERS Activity and Chemical Stability.* ACS Applied Materials & Interfaces, 2014. **6**(5): p. 3750-3757.
16. McEachran, M., et al., *Ultrathin Gold Nanoframes through Surfactant-Free Templating of Faceted Pentagonal Silver Nanoparticles.* Journal of the American Chemical Society, 2011. **133**(21): p. 8066-8069.
17. Jing, H. and H. Wang, *Structural Evolution of Ag–Pd Bimetallic Nanoparticles through Controlled Galvanic Replacement: Effects of Mild Reducing Agents.* Chemistry of Materials, 2015. **27**(6): p. 2172-2180.
18. Chen, J., et al., *Gold Nanocages: Bioconjugation and Their Potential Use as Optical Imaging Contrast Agents.* Nano Letters, 2005. **5**(3): p. 473-477.
19. Patarroyo, J., et al., *One-pot polyol synthesis of highly monodisperse short green silver nanorods.* Chemical Communications, 2016. **52**(73): p. 10960-10963.
20. Yu, D. and V.W.-W. Yam, *Controlled Synthesis of Monodisperse Silver Nanocubes in Water.* Journal of the American Chemical Society, 2004. **126**(41): p. 13200-13201.
21. Zhang, Q., et al., *Seed-Mediated Synthesis of Ag Nanocubes with Controllable Edge Lengths in the Range of 30–200 nm and Comparison of Their Optical Properties.* Journal of the American Chemical Society, 2010. **132**(32): p. 11372-11378.
22. Peng, S. and Y. Sun, *Synthesis of Silver Nanocubes in a Hydrophobic Binary Organic Solvent.* Chemistry of Materials, 2010. **22**(23): p. 6272-6279.
23. Sun, Y. and Y. Xia, *Shape-Controlled Synthesis of Gold and Silver Nanoparticles.* Science, 2002. **298**(5601): p. 2176-2179.
24. Zhang, Q., et al., *Facile Synthesis of Ag Nanocubes of 30 to 70 nm in Edge Length with CF3COOAg as a Precursor.* Chemistry – A European Journal, 2010. **16**(33): p. 10234-10239.
25. Zhang, W., J. Yang, and X. Lu, *Tailoring Galvanic Replacement Reaction for the Preparation of Pt/Ag Bimetallic Hollow Nanostructures with Controlled Number of Voids.* ACS Nano, 2012. **6**(8): p. 7397-7405.
26. Mahmoud, M.A., F. Saira, and M.A. El-Sayed, *Experimental Evidence For The Nanocage Effect In Catalysis With Hollow Nanoparticles.* Nano Letters, 2010. **10**(9): p. 3764-3769.
27. Mahmoud, M.A., B. Garlyyev, and M.A. El-Sayed, *Controlling the Catalytic Efficiency on the Surface of Hollow Gold Nanoparticles by Introducing an Inner Thin Layer of Platinum or Palladium.* The Journal of Physical Chemistry Letters, 2014. **5**(23): p. 4088-4094.
28. Zhang, L., et al., *Platinum-based nanocages with subnanometer-thick walls and well-defined, controllable facets.* Science, 2015. **349**(6246): p. 412-416.
29. Zhu, X., et al., *Realization of Red Plasmon Shifts up to ~900 nm by AgPd-Tipping Elongated Au Nanocrystals.* Journal of the American Chemical Society, 2017. **139**(39): p. 13837-13846.
30. Smith, A.M., M.C. Mancini, and S. Nie, *Second window for in vivo imaging.* Nature Nanotechnology, 2009. **4**: p. 710.
31. Chen, J., et al., *Immuno Gold Nanocages with Tailored Optical Properties for Targeted Photothermal Destruction of Cancer Cells.* Nano Letters, 2007. **7**(5): p. 1318-1322.

32. Near, R., S. Hayden, and M. El-Sayed, *Extinction vs Absorption: Which Is the Indicator of Plasmonic Field Strength for Silver Nanocubes?* The Journal of Physical Chemistry C, 2012. **116**(43): p. 23019-23026.
33. Zhou, F., et al., *Quantitative Analysis of Dipole and Quadrupole Excitation in the Surface Plasmon Resonance of Metal Nanoparticles.* The Journal of Physical Chemistry C, 2008. **112**(51): p. 20233-20240.
34. Bansal, V., et al., *Shape dependent electrocatalytic behaviour of silver nanoparticles.* CrystEngComm, 2010. **12**(12): p. 4280-4286.
35. Park, T.-H., et al., *Morphology evolution of Ag/Au nanocomposites via temperature-controlled galvanic exchange to enhance catalytic activity.* RSC Advances, 2017. **7**(13): p. 7718-7724.
36. Skrabalak, S.E., et al., *Facile synthesis of Ag nanocubes and Au nanocages.* Nat. Protocols, 2007. **2**(9): p. 2182-2190.
37. Smith, D.K. and B.A. Korgel, *The Importance of the CTAB Surfactant on the Colloidal Seed-Mediated Synthesis of Gold Nanorods.* Langmuir, 2008. **24**(3): p. 644-649.
38. Yang, Y., et al., *Galvanic Replacement-Free Deposition of Au on Ag for Core–Shell Nanocubes with Enhanced Chemical Stability and SERS Activity.* Journal of the American Chemical Society, 2014. **136**(23): p. 8153-8156.
39. Ghosh, T., B. Satpati, and D. Senapati, *Characterization of bimetallic core-shell nanorings synthesized via ascorbic acid-controlled galvanic displacement followed by epitaxial growth.* Journal of Materials Chemistry C, 2014. **2**(13): p. 2439-2447.
40. Zhang, Q., et al., *Synthesis of Ag@AgAu Metal Core/Alloy Shell Bimetallic Nanoparticles with Tunable Shell Compositions by a Galvanic Replacement Reaction.* Small, 2008. **4**(8): p. 1067-1071.
41. Xiong, Y., et al., *Poly(vinyl pyrrolidone): A Dual Functional Reductant and Stabilizer for the Facile Synthesis of Noble Metal Nanoplates in Aqueous Solutions.* Langmuir, 2006. **22**(20): p. 8563-8570.
42. Chen, J., et al., *Gold Nanocages: Engineering Their Structure for Biomedical Applications.* Advanced Materials, 2005. **17**(18): p. 2255-2261.
43. Yang, X., et al., *Photoacoustic Tomography of a Rat Cerebral Cortex in vivo with Au Nanocages as an Optical Contrast Agent.* Nano Letters, 2007. **7**(12): p. 3798-3802.
44. Casals, E., et al., *Time Evolution of the Nanoparticle Protein Corona.* ACS Nano, 2010. **4**(7): p. 3623-3632.
45. Xia, F., et al., *Colorimetric detection of DNA, small molecules, proteins, and ions using unmodified gold nanoparticles and conjugated polyelectrolytes.* Proceedings of the National Academy of Sciences, 2010. **107**(24): p. 10837-10841.
46. Casals, E., et al., *Hardening of the Nanoparticle–Protein Corona in Metal (Au, Ag) and Oxide (Fe3O4, CoO, and CeO2) Nanoparticles.* Small, 2011. **7**(24): p. 3479-3486.
47. Monopoli, M.P., et al., *Biomolecular coronas provide the biological identity of nanosized materials.* Nat Nano, 2012. **7**(12): p. 779-786.

Chapter 3

Multidomain and Multimetallic Nanotubes.

In this chapter, a general synthetic route for the preparation of multidomain bimetallic AgAu, trimetallic AgAuPt, AgAuPd and tetrametallic AgAuPdPt NTs is presented. Multimetallic NTs have been successfully prepared via a simple and sequential GRR at room temperature using Ag NWs as sacrificial templates. The prepared NTs exhibited catalytic activity toward the reductive degradation of 4-nitrophenol by $NaBH_4$ due to their characteristic morphology and the synergism between the constituent metals. This strategy offers a convenient, versatile and highly valuable approach to the fabrication of multimetallic nanostructures with various components and compositions.

3.1 Introduction

Multimetallic nanostructures which are composed of different metals integrated into a single NP in a controlled spatial arrangement, represent an unprecedented possibility to increase the diversity and degree of complexity of nanostructured materials. These advanced nanostructures possess pronounced physicochemical properties compared with individual constituent metal counterparts via synergism between components. These properties, which are ascribed to changes in their atomic and electronic structure upon introducing other metal species, enables their use as very effective surface enhanced Raman scattering (SERS) substrates [1] and optical waveguides. Especially interesting is their use as electro and chemical catalysts, where the incorporation of additional metals to the nanostructure facilitates surface adsorption/desorption processes, modulates lattice strain [2-4], and their electronic states. This effectively improves their activity, selectivity and/or reusability and results in unprecedented efficiencies in hydrogenation and oxygen reduction reactions (ORRs) [5, 6]. Furthermore, hollow NPs overcome important drawbacks of noble metals, maximizing their mass specific catalytic activity [7] and surprisingly enhancing their stability and robustness.

Because the properties of NPs highly depend on their morphology and composition, the rational design and production of multimetallic NPs has been a research topic of great interest the last few years. To date, bimetallic NPs composed of combinations of metals, such as AuPt [8], AgAu [9, 10], AgPt [11], PdPt [2, 12-14], have been obtained by wet chemical approaches including co-nucleation/co-reduction methods, thermal decomposition and seeded-growth strategies [15-17]. These techniques have been further exploited for the production of multimetallic NPs, including solid AuPtPd [18], core(alloy)/shell AuAg@Pd [19], AgPd@Pt [20, 21], core/shell(alloy) Au@PdPt [22], core/shell/shell structures, Au@Pd@Pt [23] and domain-segregated AgAuPt NPs [24]. However, despite the remarkable results obtained, the control of NP morphology and composition by these methods is not straightforward. This is due to the difficulties in controlling the nucleation and growth pathways of different metal precursors with different redox potentials, interfacial energies, and reduction kinetic rates.

Among the different synthetic strategies, GRRs represent a versatile route to produce nanostructures with controllable hollow sections [25]. This reaction, involving the oxidation of sacrificial templates with a precursor containing a relatively more noble metal ion, has been proved effective in producing a wide variety of hollow bimetallic NPs, such as AgAu [26], AgPt [27], AgPd [27, 28], and PdPt [29]. Furthermore, as the morphology of the sacrificial template is preserved, the shape of the final nanostructures can be adjusted by selecting the template and finely controlling the interfacial deposition and alloying (dealloying) processes, ultimately determined by the intrinsic miscibility of the metals involved in the reaction. Thus, using metal NWs as sacrificial templates, one-dimensional (1D) bimetallic NTs, based on AgAu [30, 31], AgPd [32], AgPt [33], PtPd [2], AuPt [34] and trimetallic PtAgAu NTs [35] have been reported, which are of special interest due to their unique properties and promising applicability.

The production of multimetallic nanostructures involving three or more metal precursors has been traditionally restricted by the complex reaction environments involved, in particular due to the difficulty in promoting (or preventing) GRR processes by adjusting reaction conditions (differences in precursor reduction, decomposition rates and miscibility of metallic phases). In spite of these limitations, Weiner et al. [36] recently reported a synthetic route to produce trimetallic AgAuPd nanostructures by coupling seed-mediated co-reduction with galvanic replacement, simultaneously reducing Au and Pd precursors with AA

in the presence of CTAC using Ag NCs as templates. A similarly strategy was reported by Pen et al. on the preparation of AgAuPt nanocages [37]. Despite its versatility, GRR has important limitations because its use is restricted to metals that have higher reduction potential values than those of metal sacrificial templates.

In this regard, the question still remains of how to produce more complex multimetallic nanostructures, involving three or more metal precursors. Based on existing knowledge of GRR, we herein develop a facile, efficient and reproducible sequential approach for the production of multimetallic AgAuPtPd NTs using Ag NWs as sacrificial templates, CTAB as surfactant, $HAuCl_4$, K_2PdCl_6 and/or K_2PtCl_4 as an oxidizing agents and AA as a co-reducing agent. The method, based on controlled successive galvanic corrosion of the Ag NWs, relies on the delicate control of the rate of Ag galvanic oxidation, which is achieved by coupling the action of GRR with other chemical processes, in particular the competing reduction of the metal precursors and the control of its diffusion kinetics. Furthermore, the success of this shape transformation from solid NWs to quaternary NTs offers a convenient, versatile, low-cost, and highly valuable approach to the fabrication of multimetallic nanostructures with various components and compositions. Additionally, this rational approximation could provide a better understanding of the parameters controlling the reaction ultimately leading to the control of the overall morphological and composition of the system.

3.2 Materials and methods

3.2.1 Materials

Ethylene glycol anhydrous, 99.8% (EG), silver nitrate ≥ 99.0% ($AgNO_3$), platinum chloride 98% ($PtCl_2$), Potassium tetrachloroplatinate (II) 98% (K_2PtCl_4), polyvinylpyrrolidone (PVP, Mw ≈360.000), gold (III) chloride trihydrate ≥ 99.9% ($HAuCl_4.3H_2O$), Potassium hexachloropalladate (IV) 99% (K_2PdCl_6), cetyltrimethylammonium bromide ≥ 99 % (CTAB), L-ascorbic acid (AA), 4-nitrophenol and sodium borohydride ($NaBH_4$) were purchased from Sigma-Aldrich. All chemicals were used as received without further purification. Distilled water passed through a Millipore system (ρ = 18.2 MΩ) was used in all experiments.

3.2.2 Methods

3.2.2.1 Synthesis of Ag NWs. A polyol process was used to synthesize Ag NWs [38]. In a typical synthesis, 5 mL of EG was placed in a round- bottom flask and heated in an oil bath at 160°C. A solution of 0.15 mM $PtCl_2$ (0.5 mL) was added. After 10 minutes, a mixture of 2.5 mL of $AgNO_3$ (0.12 M in EG) and 5 mL of PVP solution (0.36 M in EG based on the repeating unit) were added through a syringe pump under magnetic stirring. The solution was heated at 160°C for one hour. The final product was diluted with acetone and centrifuged at 2000 g for 15 min, and finally redispersed in MQW for further use.

3.2.2.2 Synthesis of AgAu multidomain NTs. In a typical synthesis, 0.5 mL of Ag NWs (427 ppm Ag+, 3.9 mM by ICP-MS) were dispersed in 2 mL of milli-Q water, 1 mL of CTAB (20 mM), and 0.1 mL of AA (0.1 mM) were added. Then, 0.2 mL of $HAuCl_4$ (1mM), was added through a syringe pump at a rate of 25 μL/min under stirring. After the addition of the $HAuCl_4$ solution, the reaction was stirred for 30 min at room temperature until the solution UV-vis spectra became stable. The sample was centrifuged at 2000 g for 10 min and washed with MQW twice; finally the pellet was resuspended in 1 mL of MQW for further catalytic essays and characterization.

3.2.2.3 Synthesis of AgAuPt NTs. In a typical synthesis, 0.25 mL of as prepared AgAu MDNTs were dispersed in 2 mL of MQW and 1 mL of CTAB (20 mM), was then added. Then, 0.1 mL of K_2PtCl_4 (1mM) was added through a syringe pump at a rate of 25 μL/min under stirring at room temperature. After the addition of the K_2PtCl_4 solution, the reaction was stirred overnight. The sample was centrifuged at 2000 g for 10 min and washed with MQW twice; finally the pellet was resuspended in 1 mL of MQW for further characterization.

3.2.2.4 Synthesis of AgAuPd NTs. In a typical synthesis, 0.25 mL of as prepared AgAu MDNTs were dispersed in 2 mL of MQW and 1 mL of CTAB (20 mM), was then added. Then, 0.1 mL of Na_2PdCl_6 (1mM) was added through a syringe pump at a rate of 25 μL/min under stirring at room temperature. After the addition of the Na_2PdCl_4 solution, the reaction was stirred for 3 hours until the solution UV-vis spectra became stable. The sample was centrifuged at 2000 g and washed with MQW twice; finally the pellet was resuspended in 1 mL of MQW for further catalytic essays and characterization.

3.2.2.5 Synthesis of AgAuPd multidomain NTs. In a typical synthesis, 0.50 mL of as prepared AgAu MDNTs were dispersed in 2 mL of MQW and 1 mL of CTAB (20 mM) was then added. Then, 0.1 mL of Na_2PdCl_4 (1mM) was added through a syringe pump at a rate of 25 μL/min under stirring at room temperature. After the addition of the Na_2PdCl_4 solution, the reaction was stirred for 3 hours until the solution UV-vis spectra became stable. The sample was centrifuged at 2000 g for 10 min and washed with MQW twice; finally the pellet was resuspended in 1 mL of MQW for further catalytic essays and characterization.

3.2.2.6 Synthesis of AgAuPdPt NTs. In a typical synthesis, 0.25 mL of as prepared AgAuPd MDNTs were dispersed in 2 mL of milli-Q water and 1 mL of CTAB (20 mM) was then added. Then, 0.1 mL of K_2PtCl_4 (1mM) was added through a syringe pump at a rate of 25 μL/min under stirring at room temperature. After the addition of the K_2PtCl_4 solution, the reaction was stirred overnight. The sample was centrifuged at 2000 g for 10 min and washed twice with milli-Q water; finally the pellet was resuspended in 1 mL of milli-Q water for further catalytic essays and characterization.

3.2.2.7 Catalytic reduction of 4-nitrophenol. The reduction of 4-nitrophenol to 4-aminophenol with $NaBH_4$ was used as a probe reaction because the change of colour is easy to monitor by UV-vis absorption spectroscopy. In a typical process, in a 4 mL cuvette, 2 mL of MQW was mixed with 50 μL of 5 mM 4-nitrophenol, then 0.1 mL of freshly prepared 0.1M $NaBH_4$ solution was added, resulting in a change in colour of the solution from pale yellow to bright yellow due to the conversion of 4-nitrophenol to 4-nitrophenolate anion. Finally, 50 μL of NPs were added (77.5 ppm Ag^+ for Ag NWs) and the UV-vis absorption spectra was recorded between 500 - 300 nm at a time increment of 1 minute. The same concentration of NPs was maintained during the catalytic reaction to compare all the catalytic experiments.

3.2.2.8 Characterization

Absorption spectra of the as synthesized NPs were acquired with a Shimadzu UV-2401PC spectrophotometer.

The morphology of the synthesized NTs was investigated by TEM, HR-TEM, STEM, and SEM. The compositional analysis of the synthesized nanotubes was performed by EDS line scan and elemental analysis. The morphology and size of the NPs were visualized using FEI Magellan 400L XHR SEM, in scanning mode operated at 1kV and in transmission mode operated at 20

kV. STEM-EDS maps and line scans were obtained in a FEI Tecnai G2 F20 S-TWIN HR(S) TEM, operated at an accelerated voltage of 200 kV. A droplet of the sample was drop cast onto a piece of ultrathin carbon-coated 200-mesh copper grid (Ted-pella, Inc.) and left to dry in air. XRD data were collected on a PANalytical X'Pert diffractometer using a Cu Kα radiation source.

3.3 Results

The controlled production of multimetallic AgAuPdPt NTs, herein presented, relies on the individual control of 3 sequential GRR steps onto Ag NW templates with the 3 different metal precursors (Au, Pd and Pt) involved in the reaction. The galvanic replacement process in the simplest case of bimetallic AgAu multidomain NTs is first presented and then extended to a more complex mixture of metals, where the Ag template was progressively replaced with more noble metals.

The replacement process occurs when a more noble metal cation is allowed to react with a less noble nanostructure in the same solution. Interestingly, starting with Ag NWs, the partial (uncompleted) GRR by the addition of $HAuCl_4$ at substoichiometric concentrations, results in the formation of AgAu periodic hollow-solid multidomain NTs comprising the sequential formation of solid Ag parts and hollow AgAu parts. Solid and hollow domains appear because the GRR has geometrical constraints but, in contrast to the pinholes observed in spherical and cubic NPs, in this reaction, a pinhole cannot control the dissolution of the whole Ag NCs. As a result, different pinholes appear at distances stablished by the chemical potential of the reaction (determined by factors such as reagent concentration, time, presence of stabilizers and complexing agents, temperature and surface state). The Ag residue that has not exchanged with Au^+ ions is further replaced by the controlled addition of K_2PtCl_4 or Na_2PdCl_6, which leads to ternary alloy hollow NCs without any significant change in their morphology. Finally, the GRR reaction of AuAgPd hollow NWs with K_2PtCl_4 produces AgAuPdPt NWs with morphological and compositional control as illustrated in **Scheme 3.1**.

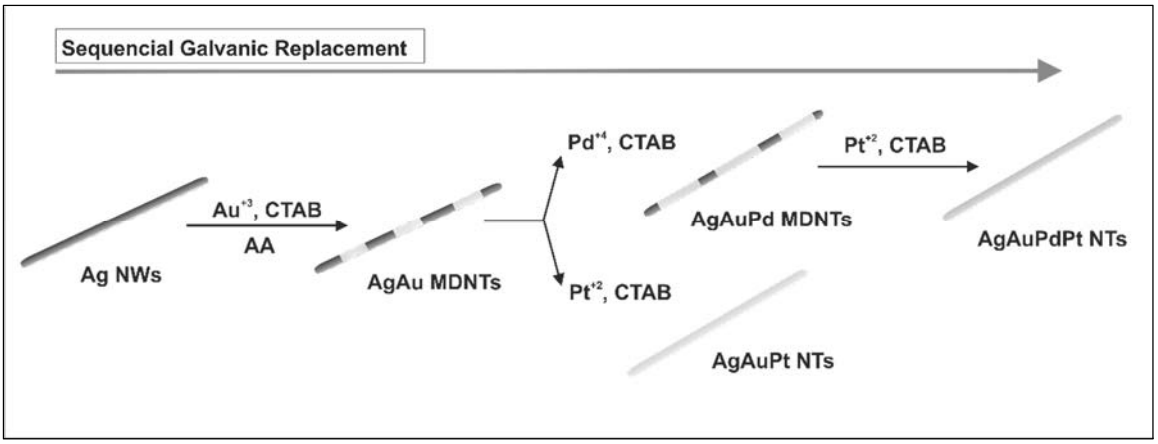

Scheme 3.1 Representation of the synthesis of multimetallic nanostructures

In each individual process, the partial Ag replacement relies on the controlled oxidation of the Ag templates at room temperature by the metal precursor involved in the reaction (Au, Pt or Pd), which is achieved by adjusting the precursor's reactivity and galvanic reaction rate. Thermodynamically, these GRR are a rather strong reaction and precise control of the corrosion process is difficult to achieve, resulting in poor morphological control. Therefore, to be able to progressively remove material from the inside of the initial Ag NWs with different metallic precursors, the chemical potential of the reaction has to be lowered to allow better kinetic control and the obtention of desired intermediate species. In order to get this control working at room temperature, it is necessary to add surfactants, co-reducers and complexing agents

The use of a cationic surfactant, such as CTAB, which serves as a NP surface stabilizer, structure directing agent and complexing ligand, simultaneously reduces the reduction rate of the metal precursor and inducing its epitaxial deposition. A co-reductant, such as AA, competes with the Ag template for the reduction of the metal species, modifying delivery of the metal precursor and allowing the deposition rate to be adjusted. This precise adjustment of synthetic parameters allows the control of whole the shape transformation from NWs to quaternary NTs and prevents secondary NP nucleation in solution and nonspecific metal deposition at the surface of the NTs.

3.3.1 Synthesis of AgAu multidomain NTs. For the production of multimetallic NTs, the first step involves the synthesis of AgAu multidomain NTs at room temperature *via* GRRs of Ag NWs, after the addition of controlled substoichiometric amounts of $HAuCl_4$ in the presence of CTAB and AA.

Ag NWs were prepared as previously described by Xia *et al* [38] with minor modifications, as was described previously in the methods section, with lengths of up to ~5 μm and widths of 60-80 nm. TEM images are shown in **Figure 3.1A-B** and a SEM image is presented in **Figure 3.1C** indicating that the Ag NWs displayed well defined shapes and smooth surfaces. **Figure 3.1D** shows UV-vis spectrum of the as synthesized Ag NWs. The spectrum exhibit two relatively sharp surface plasmon resonance (SPR) peaks at ~350 and ~380 nm, both of them corresponding with reported values for Ag NWs and are attributed to the quadrupole and the transverse plasmon resonance of the Ag NWs with pentagonal cross-section [38, 39].

Initially, Pt seeds were found to be nucleated which act as seeds for subsequent growth of Ag NWs. These Pt NPs serve as seeds for the heterogeneous nucleation and growth of Ag [38]. Formation and growth of Ag NWs may be driven by the deposition of Ag atoms on {111} planes of these Pt NPs. The presence of PVP on Ag {100} plane could be a reason for the one dimensional growth along the longitudinal axis of Ag NWs. Also, the PVP could benefit the formation of Ag NWs by strongly attaching to the Ag {100} and {110} rather than {111} facets [40]. The density of PVP molecules bound to the side surfaces of the NWs is very high compared to that of edges of the Ag NWs, which allows growth along the NRs axis leading to high aspect ratio NWs.

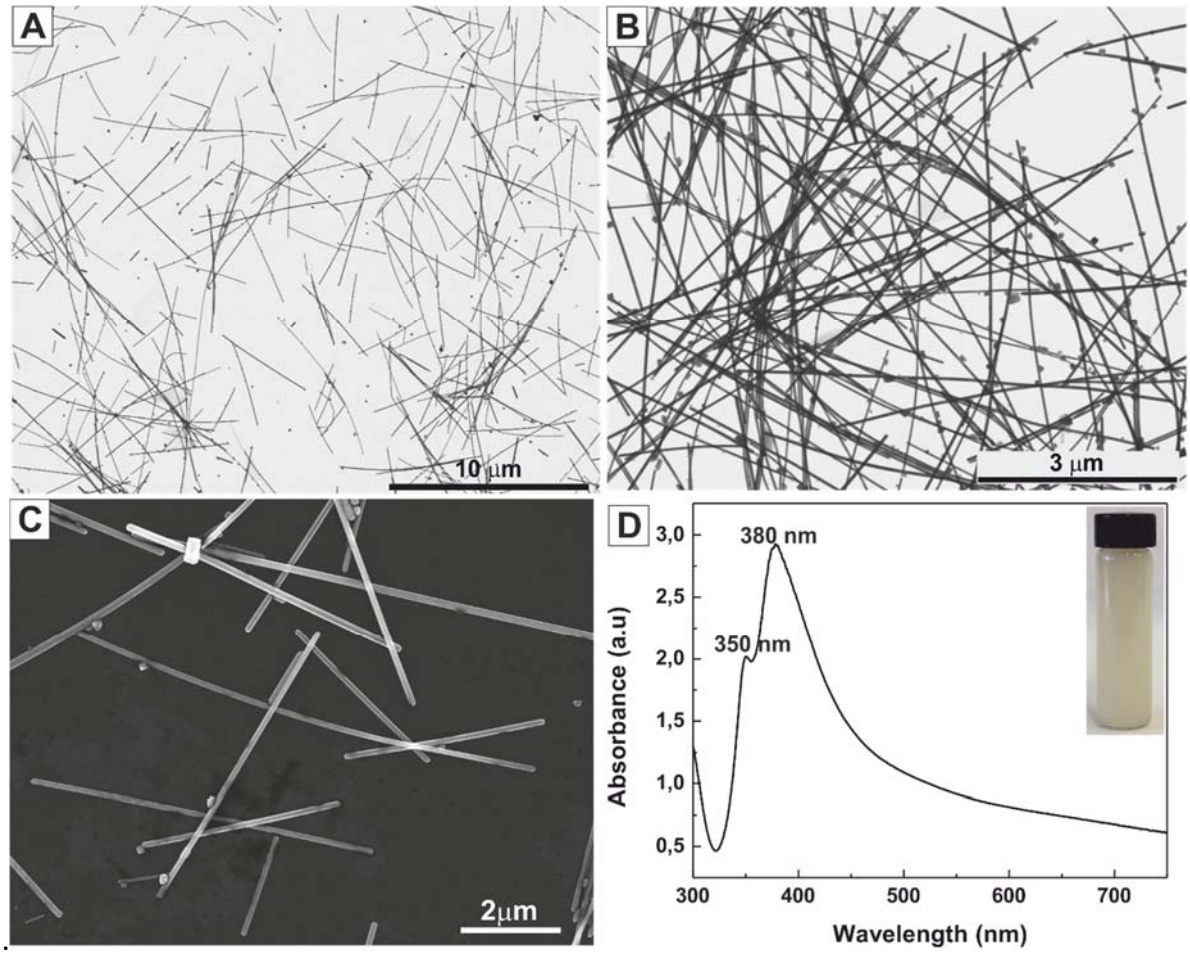

Figure 3.1 A. Low magnification TEM **B.** TEM, and **C.** SEM images of Ag NWs. **D.** UV-Vis spectrum of Ag NWs, inset shows a photograph of aqueous dispersion of Ag NWs.

Using these Ag NWs as sacrificial templates, AgAu multidomain NTs were produced. **Figure 3.2** shows electron microscopy images of the obtained structures. Due to the large difference in contrast between the hollow and solid regions, TEM and particularly HAADF-STEM are especially useful techniques for resolving their morphology and internal structure. **Figure 3.2A-G** shows TEM and HAADF-STEM images, where the production of NTs with periodic domains with a well-defined interface corresponding to sequential solid and hollow regions can be clearly observed. Importantly, the original dimensionality and the pentagonal cross section of the Ag NWs are largely retained, indicating that the partial GRR did not compromise the overall morphology of the NPs. Details of the solid (bright contrast regions) and hollow regions (dark contrast regions) are shown in **Figure 3.2E**, revealing a well-defined interface between domains (**Figure 3.2F**) and the overlapping of different twinned pentagonal sections (**Figure 3.2G**).

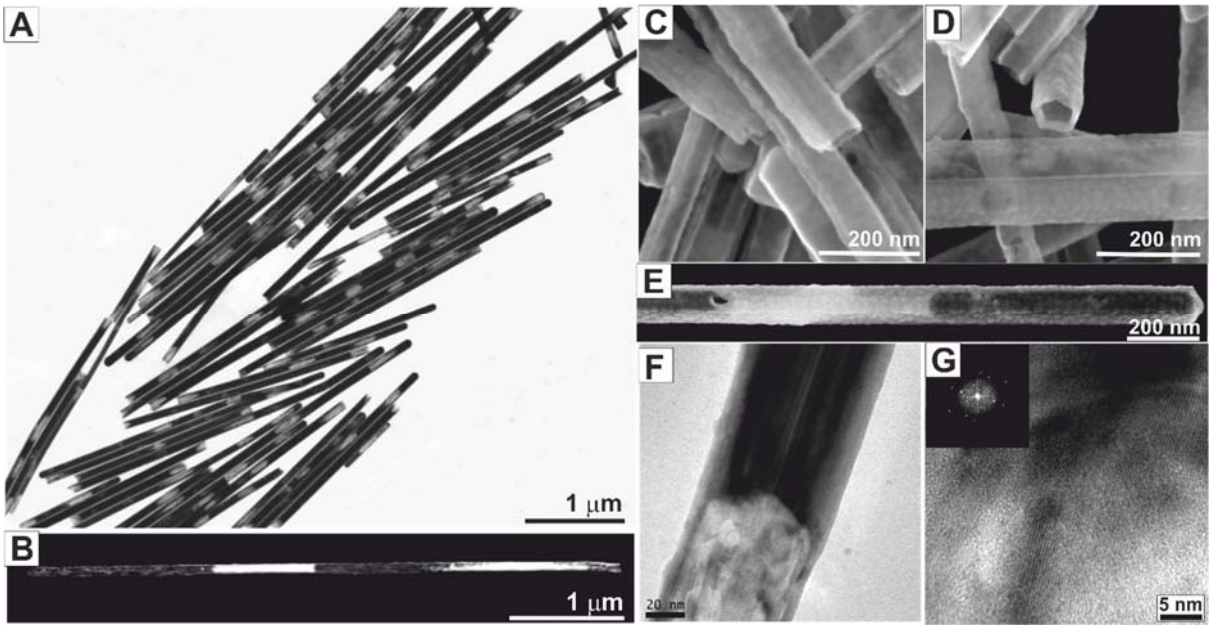

Figure 3.2 A. Low magnification TEM, **B.** HAADF-STEM. **C-E**, STEM **F**. TEM and **G**.HR-TEM of AgAu multidomain NTs.

EDS line-scanning elemental analysis obtained through the red arrow of a bimetallic AgAu multidomain NT show in the STEM-HAADF image in **Figure 3.3** the multidomain NT has an average diameter of 88 nm, the EDS analysis reveal similar results to the maps shown in **Figure 3.4** where the solid part is mostly composed of Ag and the hollow part is composed of an AgAu alloy.

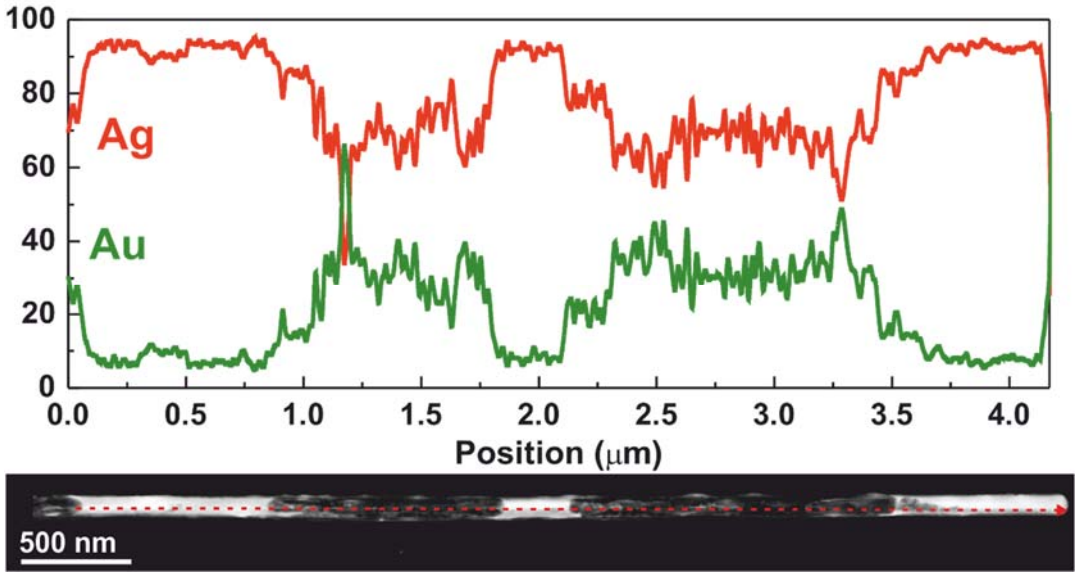

Figure 3.3 STEM-HAADF image of a multidomain NT. The EDS line scan results (Ag in red, Au in green) obtained through the red arrow. Intensities are arbitrary units and normalized.

EDS elemental mapping (**Figure 3.4,** red rectangular region) of a ~90 nm diameter AgAu multidomain NT, clearly shows that solid regions are composed mostly of Ag (red colour), covered by an outer ~8 nm Au rich layer (green colour). Furthermore, hollow domains have a higher Au composition compared with their solid parts, in general, containing ~55% Ag and ~45% Au, suggesting the successful incorporation of Au into the Ag phase of the alloy formation.

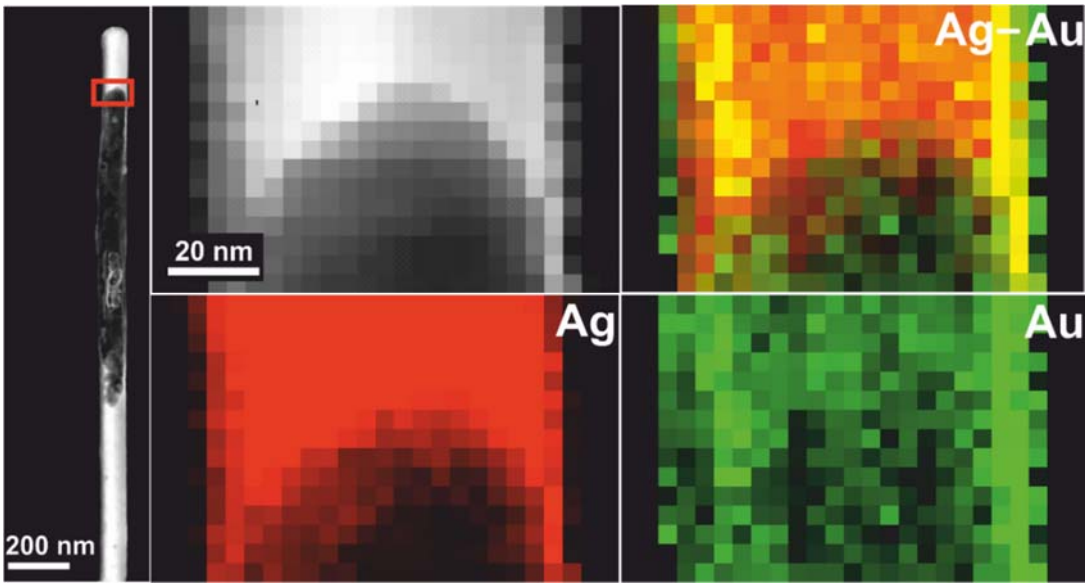

Figure 3.4 STEM image of an AgAu multidomain NT. EDS maps of the red rectangular region: Simultaneous STEM-HAADF, elemental Ag (in red) and Au (in green) maps and their composite.

3.3.2 Formation mechanism of AgAu multidomain NTs. The morphological and structural evolution from Ag NWs to multidomain AgAu NTs by changing the amount of $HAuCl_4$ added is displayed in **Figure 3.5**. Immediately after the addition of the Au precursor to the mixture containing Ag NWs, CTAB and AA, some of the Au^{3+} ions turn to Au^0 by the direct action of AA while the rest remain in the reaction system [41], assisting the GRR that starts to take place [42].

At the initial stages of the reaction, TEM images reveal the formation of small periodic pinholes at specific sites of the Ag NW, evidencing that the GRR initiated at the side surfaces of the Ag NW through a pitting process (**Figure 3.5B**) [43]. Once the reaction had started, the addition of more Au^{3+} promoted further Ag dissolution and larger pinholes were formed (**Figure 3.5C-D**). At this stage, the Au ions were then deposited on the surface of the Ag

template. Because of the matching between both crystalline structures (Ag and Au are fcc) and lattice constant of 4.0786 and 4.0863 Å for Ag and Au respectively, this deposition was epitaxial and homogeneous, forming a thin Au layer, that prevented the Ag atoms beneath from reacting with the Au precursor. A further increase of the amount of Au^{3+} ions in solution promoted the formation of larger cavities along the axis of the Ag NWs (**Figure 3.5E**). At this stages, the Au^0 remaining in solution by the direct action of AA directly deposited at the surface of the Ag NWs, increasing the thickness of the Au layer. Later, the addition of increasing amounts of Au precursor, further assisted the complete Ag NWs dissolution, leading to the formation of hollow Au NTs **(Figure 3.5F)**. The obtained multidomain and hollow bimetallic AgAu NTs exhibited an intense absorption due to their SPR [44] [45]. The UV-vis spectra (**Figure 3.5G**) of the nanostructures shown in **Figure 3.5** evolves with an increase in the amount of $HAuCl_4$ added to the reaction media which can be ascribed to the formation of AgAu alloy NWs, in particular modifications of composition (from Ag to AgAu) and morphology (from void to partially hollow) of the hybrid nanostructures. Thus, the main absorbance peak at 380 nm corresponding to the transverse mode of the SPR band of Ag NWs [45] red-shifts and broadens to longer wavelengths while an additional peak appears around 600 nm indicative of the newly formed hollow regions [44].

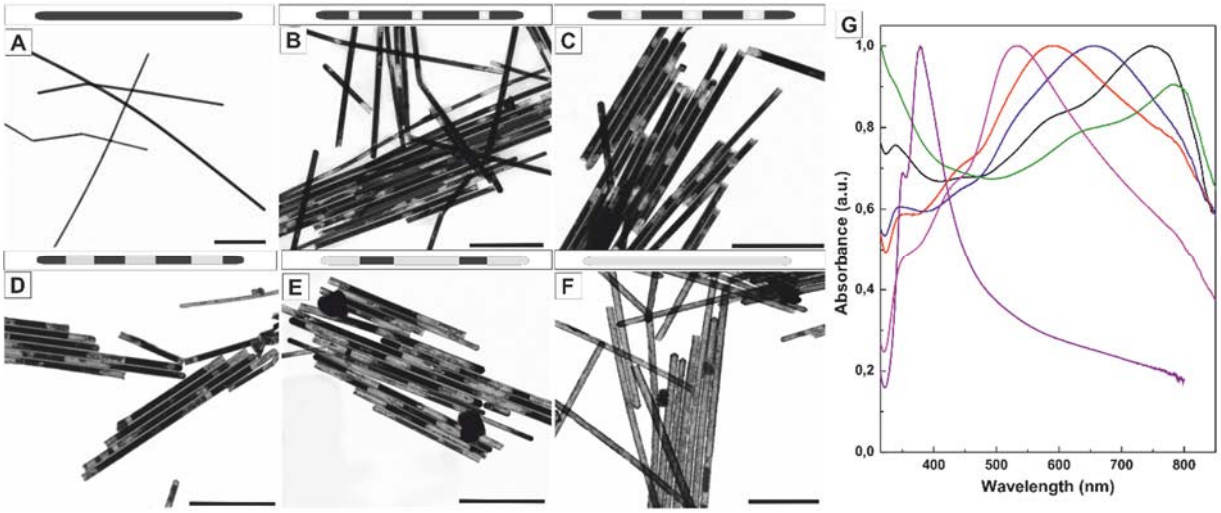

Figure 3.5 TEM images and schematic illustration of Ag nanowires **A.** before and **B-F**. After they reacted with different volumes of 1mM $HAuCl_4$ solution: **B.** 0.1 mL; **C.** 0.2 mL; **D.** 0.3 mL; **E.** 0.4 mL and **F.** 0.5 mL. Scale bar represent 1 μm for all images. **G.** UV-Vis spectra of the Ag NWs before (purple) and after reaction with different volumes of 1 mM $HAuCl_4$. 0.1 mL (magenta); 0.2 mL (red); 0.3 mL (blue); 0.4 mL (black); 0.5 mL (green).

In this synthesis, CTAB and AA play a key role in the formation of the bimetallic AgAu multidomain NTs by adjusting the reduction rate of Au ions and allowing the control of the periodic multidomain structure of the NTs. This can be explained by the different reactivity of the Au^{3+} ions in the presence of CTAB and/or AA. The reduction potentials of Au^{3+} ions in different oxidation states are Au^{3+}/Au^{+} = 1.36 V, Au^{3+}/Au^{0} = 1.5 V, and Au^{+}/Au^{0} = 1.83 V. Therefore, it is clear that the reduction of $Au^{3+} \rightarrow Au^{+}$ is more favourable than that of $Au^{3+} \rightarrow Au^{0}$, and that the less favourable reduction of $Au^{+} \rightarrow Au^{0}$ favours Au^{3+} ions to be directly reduced to Au^{0} [41]. Consequently, stabilizing Au^{+} states slows down the corrosion process. In this chemical scenario, CTAB not only serves as a surfactant and stabilizer for the nanostructures, but also acts as an inducing agent for the epitaxial deposition of Au, since CTAB solubilizes the AgCl formed during the GRR [42], leading to the formation of hollow structures with smooth surfaces. Thus, control experiments showed that in the absence of CTAB, Au was rapidly and irregularly deposited on the surface of the Ag NW in a sponge like structure, as is shown in **Figure 3.6A.** These irregular Au deposition occurs because the precipitation of AgCl crystals (K_{ps} 1.8 x 10^{-10}) formed during the GRR act as templates for the deposition [31]. Likewise, in the absence of AA, the stronger etching power of Au^{3+} (Au^{3+}/Au^{0} = 1.5V vs SHE vs. Ag^{+}/Ag^{0} 0.8V vs SHE) promotes the fast Ag oxidization, which is translated into a lack of control in the geometry and size of the inner voids (**Figure 3.6B**). A similar absence of control was found when the experiments were performed in the absence of both, CTAB and AA, where Au was deposited irregularly on the surface of the Ag NW and obtained NTs presented an uncontrolled inner etching (**Figure 3.6C**). As expected, these limitations in the formation process translate into a lack of control of the optical properties of the obtained structures as is shown in the UV-Vis spectra showed in **Figure 3.6D**.

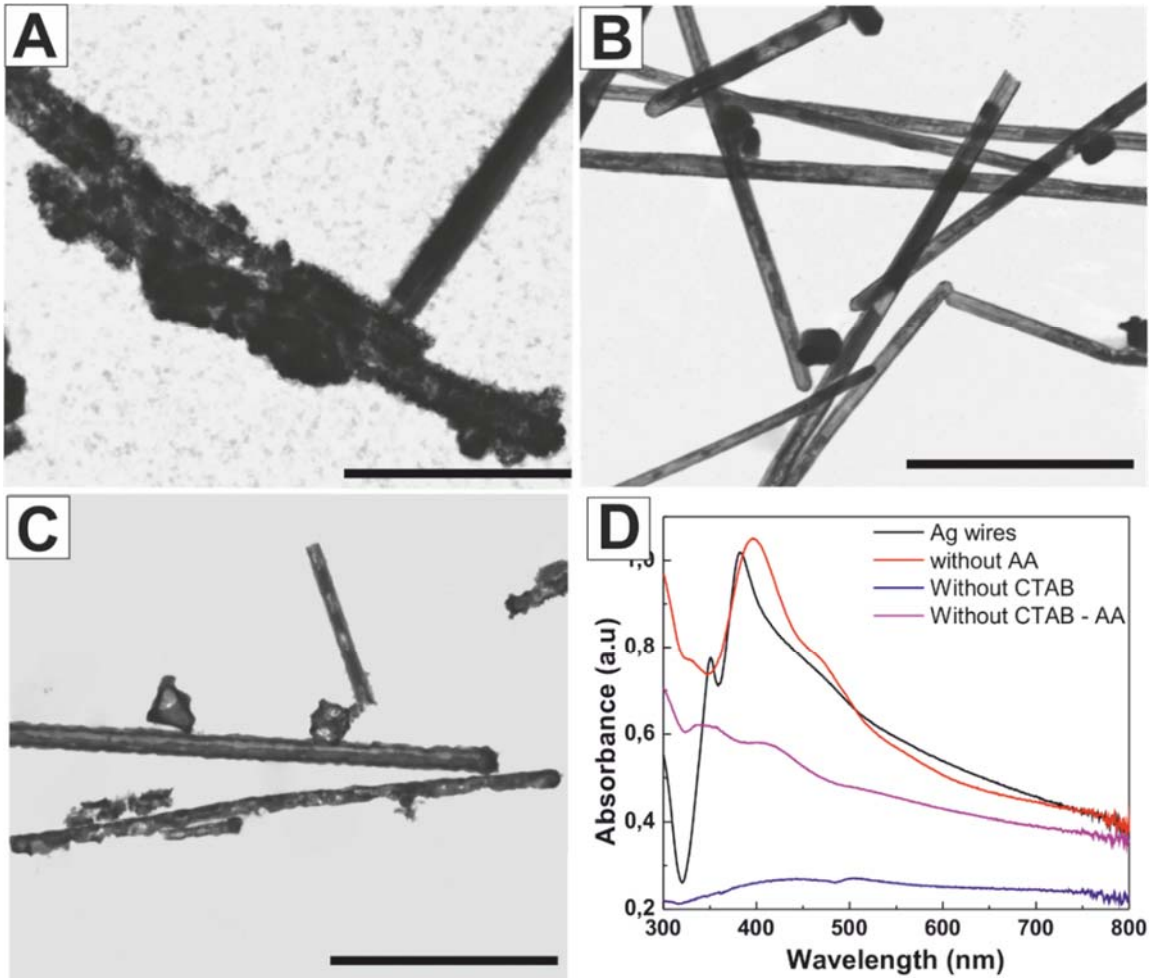

Figure 3.6 TEM images of AgAu nanostructures synthesized **A.** in the absence of CTAB, **B.** in the absence of AA and **C.** in the absence of CTAB and AA **D.** UV-Vis spectra of the Ag NWs before (black) and after reaction in absence of AA (red), in absence of CTAB (blue) and in absence of both CTAB and AA (magenta). Scale bar represent 1 μm for all images.

3.3.3 AgAuPt and AgAuPd trimetallic NTs. The second step involved the use of bimetallic AgAu multidomain NTs as templates for the production of trimetallic AgAuPt or AgAuPd NTs. This was achieved by the GRR of the Ag remaining in the solid regions of the multidomain AgAu NTs by the addition of controlled amounts of Pt^{2+} or Pd^{+4} precursors in the presence of CTAB.

As evidenced in **Figure 3.7**, the addition of controlled amounts of Pt^{+2} or Pd^{+4} solutions results in the formation of hollow trimetallic AgAuPt (red square) or AgAuPd (green square) NTs. Low-magnification TEM and HAADF-STEM images (**Figure 3.7 A, B**, and **Figure 3.7 E, F**) reveal that obtained ternary structures present larger hollow regions, ascribed to the GRR of the remained Ag not exchanged previously.

High-resolution TEM (HRTEM) images from the middle portion of an individual AgAuPt NT (**Figure 3.7C**) and from the tip of a multi-twinned AgAuPd NT (**Figure 3.7G**) reveal the presence of a continuous Pt- or Pd-rich wall with a thickness of ~25 nm and ~9nm respectively. Corresponding power spectra (FFT) in the inset image of **Figure 3.7C,G** reveal d-spacing values larger than expected for the respective metallic phases (Ag/Au/Pt 0.23 nm), suggesting that NTs are rich in a ternary alloy of AgAu and Pt or Pd respectively. SEM image of the AgAuPt NTs (**Figure 3.7D**) reveals the rough surface of the obtained structures, homogeneously covered by small Pt crystallites. In contrast, AgAuPd NTs (**Figure 3.7H**) presented rather smooth surfaces. These differences in growth mode of both metals are attributed to the different affinities of the metals (Pt and Pd) with the substrate (AgAu). Thus, the poor miscibility (higher lattice mismatch) between AgAu and Pt is known to follow a Volmer-Weber type of growth, widely characterized by the nucleation and growth of islands on the surface of the substrate.

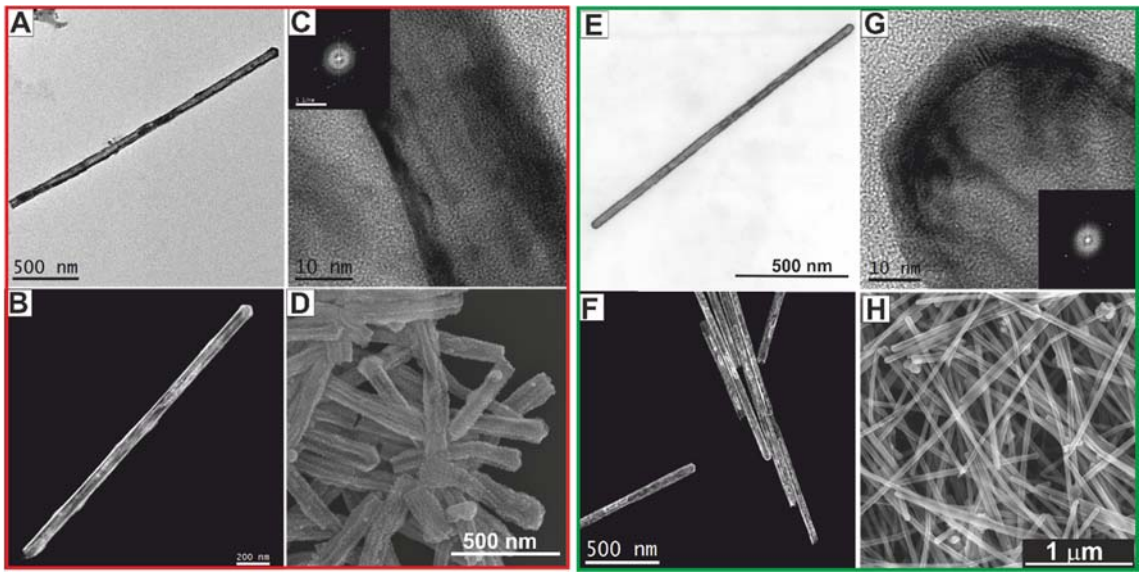

Figure 3.7 A. TEM **B.** STEM **C.** HR-TEM and **D.** SEM images of AgAuPt NTs. **E.** TEM **F.** STEM **G.** HR-TEM and **H.** SEM images of AgAuPd NTs. Insets in **C** and **G** are showing the corresponding fast Fourier transform (FFT).

To better understand the distribution of Ag, Au and Pt or Pd in the ternary NTs, elemental EDS mapping were performed. Obtained results are summarized in **Figure 3.8**, where the elemental maps (**Figure 3.8B** and **F**) of the blue dotted rectangular regions of individual AgAuPt (red square) and AgAuPd (green square) NTs are shown. In both cases, a homogeneous distribution of the constituent elements is observed. However, some

differences between both types of ternary NTs are detected when studying the corresponding elemental profiles. Thus line-scanning profile analysis taken from the purple rectangular region in **Figure 3.8C** reveals, for AgAuPt NTs, an outer layer richer in Au and Pt compared to the Ag with an average composition of Ag 31%, Au 34% and Pt 35%. This observation is in agreement with the homogeneously covered NT surface by small Pt crystallite, as was explained before. In contrast, for trimetallic AgAuPd NTs (**Figure 3.8G**), Ag and Pd present a higher intensity than Au and an average composition of Ag 38%, Au 28% and Pd 34%.

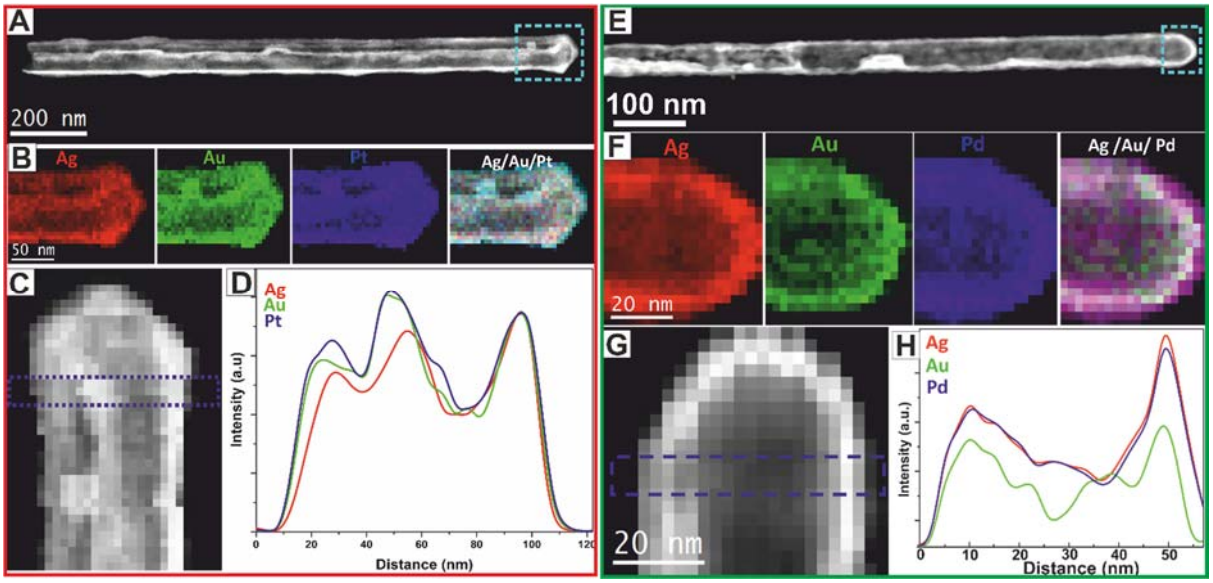

Figure 3.8 A. HAADF-STEM image of an AgAuPt NT. **B.** EDS maps of the rectangular region: Ag (red), Au (green) and Pt (blue). and composite of AgAuPt of the rectangular region in A. **C.** HAADF-STEM image of the tip of a AgAuPt NT. **D.** Intensity profiles along the red rectangular region indicated in **C**, Ag (red), Au (green) and Pt (blue). **E.** HAADF-STEM image of a AgAuPd NT. **F.** EDS maps of the rectangular region: Ag (red), Au (green) and Pd (blue). and composite of AgAuPd of the rectangular region in **E. G**. HAADF-STEM image of the tip of a AgAuPd NT. **H.** Intensity profiles along the red rectangular region indicated in C, Ag (red), Au (green) and Pt (blue).

3.3.4 AgAuPdPt tetrametallic NTs. The final step involved the use of trimetallic AgAuPd multidomain NTs as templates for the production of tetrametallic AgAuPdPt NTs. For the synthesis of this trimetallic multidomain NTs, substoichometric amounts of Pd precursor were added to the reaction (see methods for details). In **Figure 3.9A** HAADF-STEM images of trimetallic AgAuPd multidomain NTs are shown, solid and hollow domains are clearly visible.

EDS elemental mapping presented in **Figure. 3.9B** shows that the solid regions are rich in Ag, whereas the hollow regions are rich in Au and Pd. EDS line-scanning analysis presented in **Figure. 3.9C** confirms these observations.

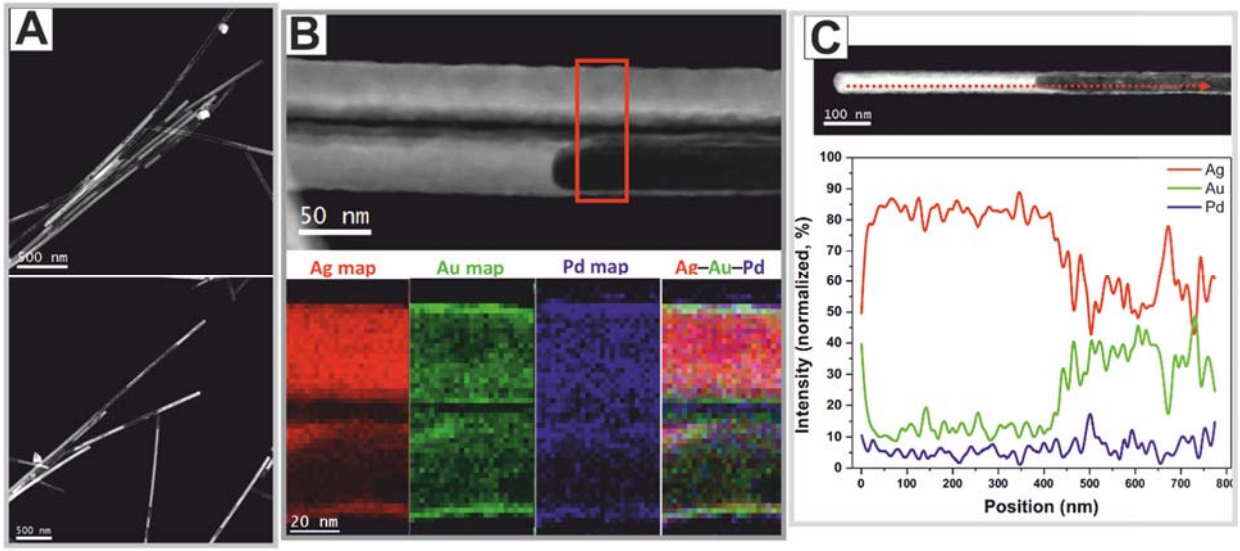

Figure. 3.9 A. HAADF-STEM images. **B.** EDS elemental analysis and **C.** EDS line scanning of trimetallic AgAuPd multidomain NTs.

Starting with these trimetallic AgAuPd multidomain NTs, the addition of the Pt^{2+} in the presence of CTAB allows a GRR of the remaining Ag solid regions, driving the production of tetrametallic AgAuPdPt NTs. The obtained product consists of well-dispersed hollow NTs of several microns in length (**Figure 3.10 A-B**) with a continuous crystalline shell with a thickness of ~11 nm. A highly magnified TEM image (**Figure 3.10C**) of the tip region of an individual tetrametallic AgAuPdPt NT clearly shows that the product is multifaceted and has a rough surface. HR-TEM analysis of this image (red square region) reveals that the NT is crystalline with a corresponding power spectrum (inset) composed of the contributions of more than one facet of the NT (**Figure 3.10D**). The analysis of the upper region of the same tube (green square) reveals the presence of small crystals (~ 8 nm) along the NT. A detailed study is shown in **Figure 3.10F** whose corresponding power spectrum suggests that the image is formed by an overlapping of different planes of these small crystals and the NT.

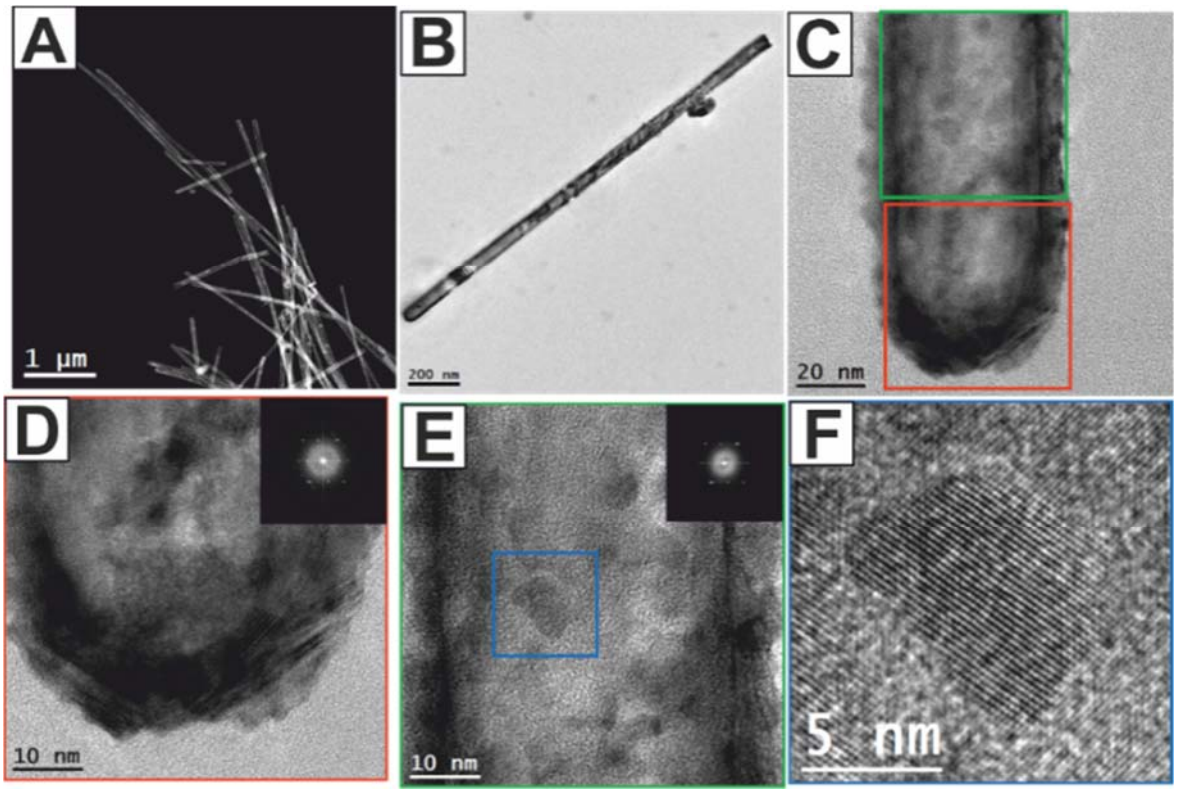

Figure. 3.10 A. HAADF-STEM. **B.** Low magnification TEM. **C.** TEM and **D.** HR-TEM images of the red square in **C.** Inset power spectrum of the AgAuPdPt NT. **E.** HR-TEM image of the green square in **C.** Inset power spectrum. **F.** HR-TEM image of the blue square in **E.**

The EDS elemental mapping of the white region in **Figure. 3.11A** distinctly confirms that the tetrametallic NTs consist of Ag, Au, Pt and Pd metals homogeneously distributed all over the sample (**Figure 3.11B**), particularly in the outer shell. Indeed, from the intensity profiles (red rectangle region in **Figure 3.11C**), the average composition is Ag 30%, Au 20%, Pd 20% and Pt 30%, which further confirms the tetrametallic composition of the NTs (**Figure 3.11D**).

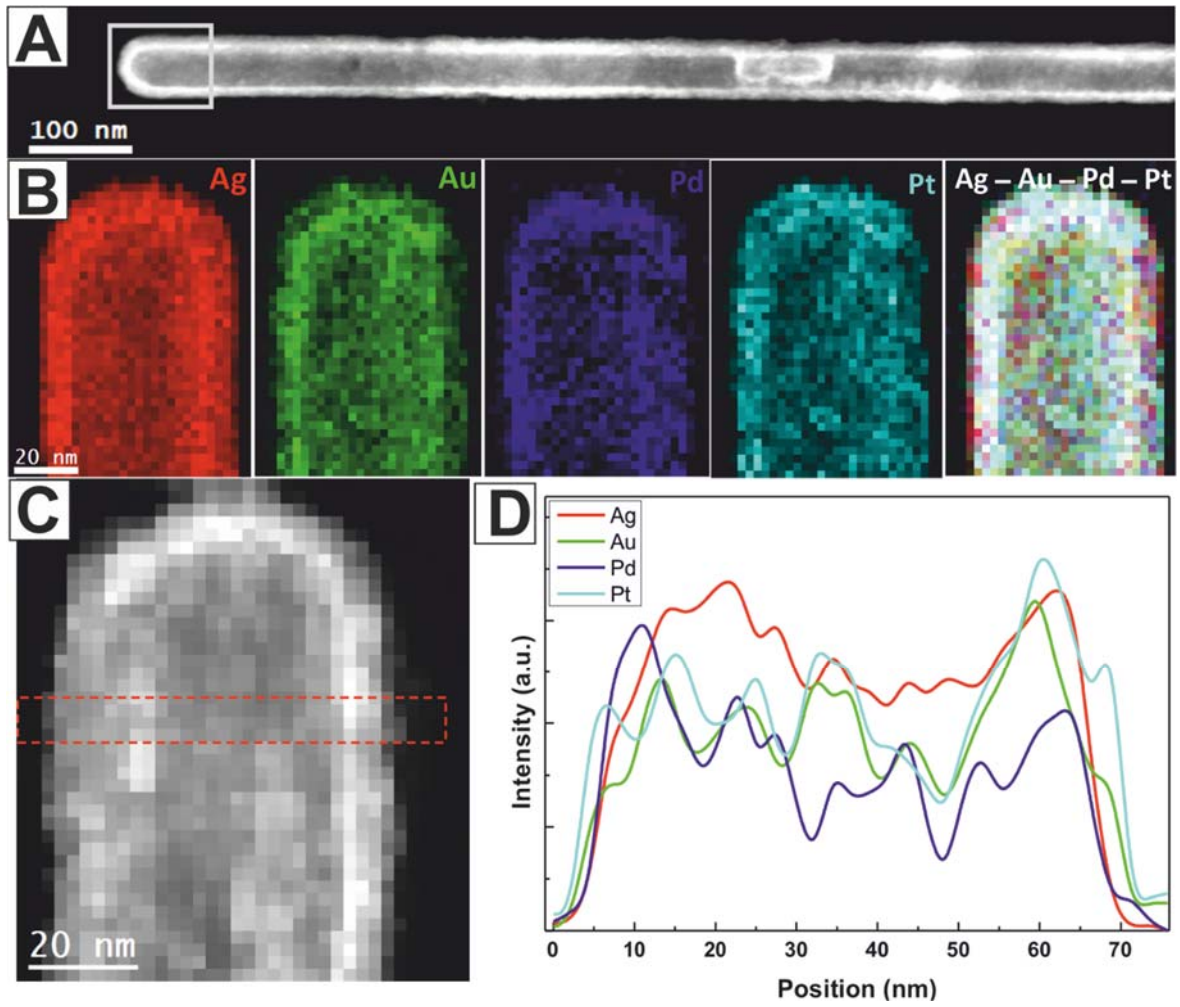

Figure 3.11 A. HAADF-STEM image of an AgAuPdPt NT. **B.** EDS maps of the red rectangular region: Ag (red), Au (green), Pd (blue) and Pt (turquoise) and composites of AgAuPdPt NT. **C.** HAADF-STEM image of the tip of a AgAuPdPt NT. **D.** Intensity profiles along the red rectangular region indicated in I, Ag (red), Au (green) Pd (blue) and Pt (turquoise)

To determine the effect of the sequential combination of GRR in the controlled attacking of Ag NWs, a control experiment involving the simultaneous addition of the three metal precursors was performed. Obtained results are summarized in **Figure 3.12**, where it can be seen how, in these conditions, the control of the morphology and composition of the NTs is completely lost, further evidencing the uncontrolled deposition of the 4 different metals involved in the GRR. In detail, most of the NTs are un-homogeneously covered by bright large domains (**Figure 3.12A-C**) with a crystallographic phase compatible with a fcc lattice, oriented along the [011] zone axis (green square, **Figure 3.12D**). Interestingly, elemental EDS mapping of an individual NT (**Figure 3.12E**), reveals that the external coverage of the hollow structures is mainly composed of Ag (in red). While Au, Ag and Pd signals could

be easily detected and mapped (displayed in green, red and blue), a Pt signal is almost inexistent and its intensity is too low for an accurate analysis.

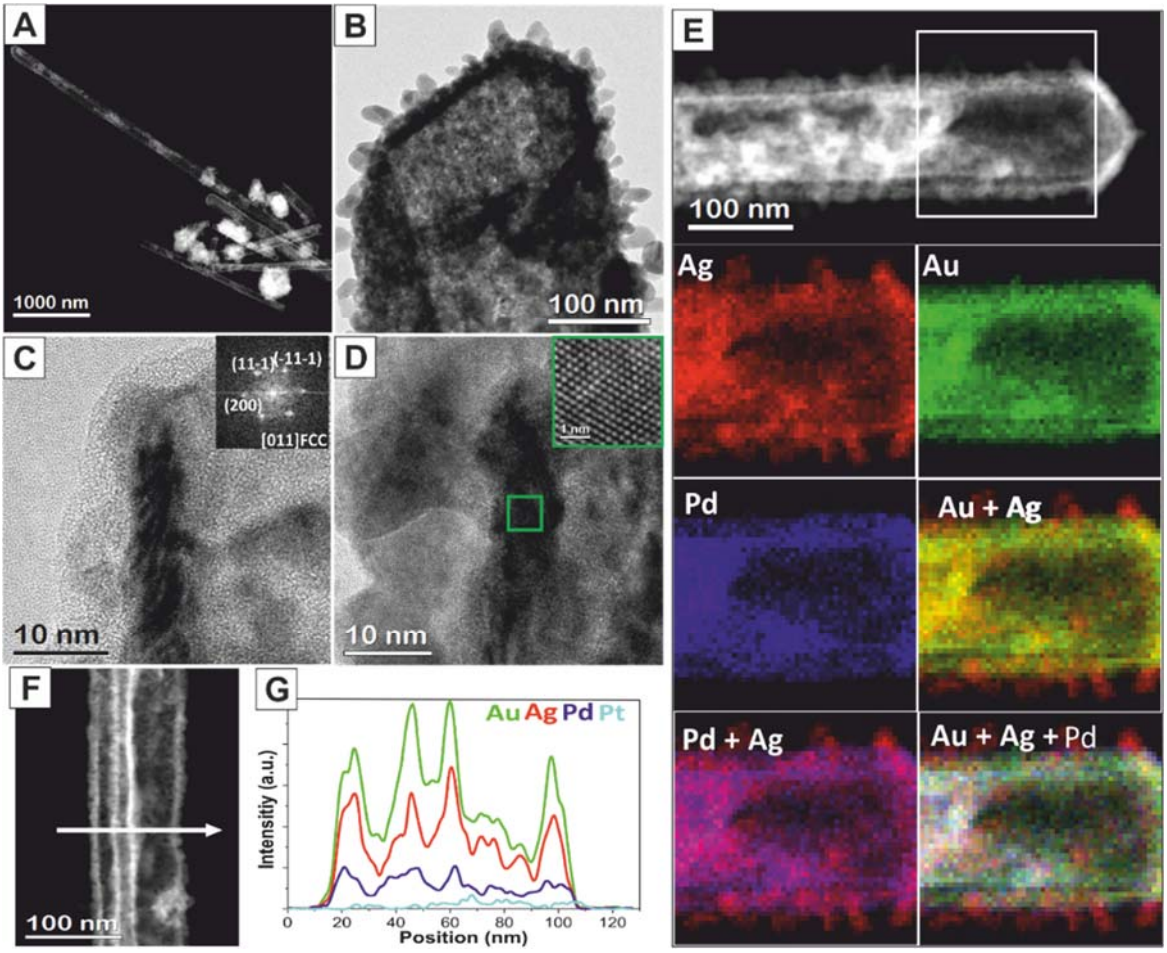

Figure 3.12 A. HAADF-STEM. **B-C.** TEM. **D.** HR-TEM of AgAuPdPt NTs. **E.** HAADF-STEM and EDS maps of the rectangular region; Ag (red), Au (green), Pd (blue) and composites. **F.** HAADF-STEM image. **G.** Intensity profiles along the white arrow indicated in **F.** Ag (red), Au (green), Pd (blue), Pt (turquoise).

X-ray diffraction (XRD) patterns of all the nanostructures previously presented in this chapter are displayed in **Figure 3.13**, which show distinct diffraction peaks for each NTs that can be indexed to the (111), (200), (220) and (311) reflections of the face centered cubic (fcc) structure of the metal, showing the pure crystalline nature of the prepared NTs. It can be observed a displacement in the (100) peak from ~38.1^{o} to 38.4^{o} for trimetallic AgAuPd NTs and 38.6^{o} for trimetallic AgAuPt Nts and tetrametallic AgAuPdPt NTs. Same behaviour is also visible with the peak indexed to the (200) reflection. The (100) and (200) reflections of the

trimetallic and tetrametallic nanostructures appears between the values of the pure metals, suggesting the presence of an alloy.

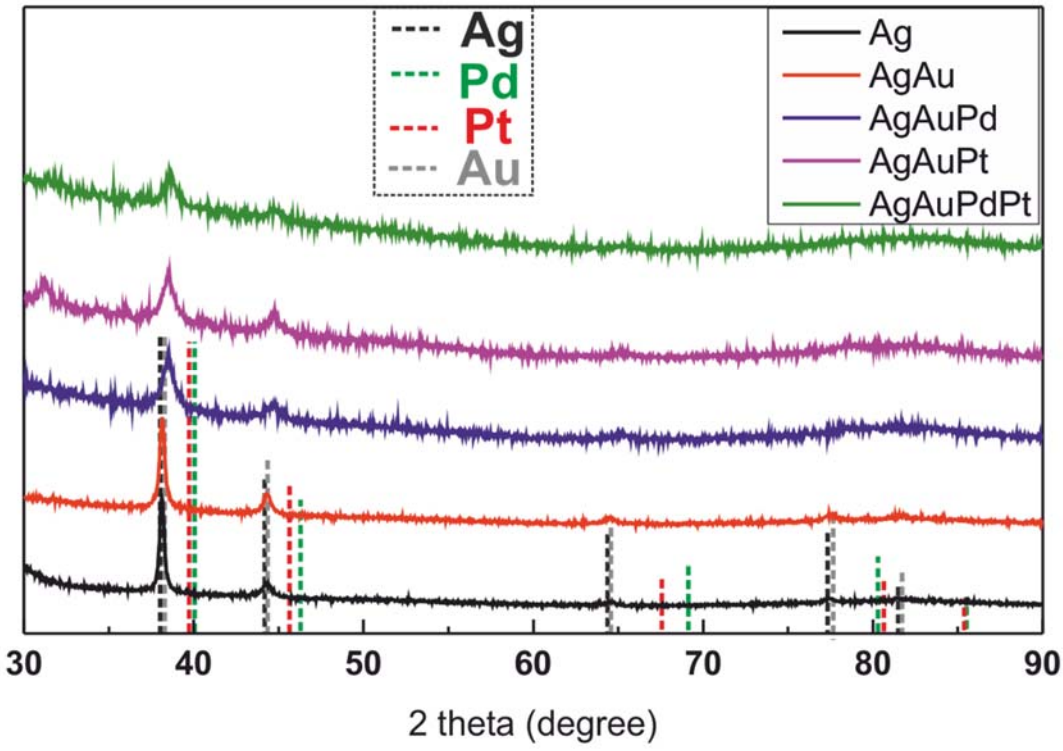

Figure 3.13. XRD patterns of the Ag NWs (black), AgAu multidomain NT (red), AgAuPd NTs (blue), AgAuPt NTs (pink) and AgAuPdPt NTs (green). Dotted lines correspond to JCPDS standard for Ag (Black, 04-0783), Pd (green, 05-0681), Pt (red, 04-0802) and Au (grey, 04-0784).

3.3.5 Surface Reactivity. One of the main interests in these multimetallic NTs is their use as catalysts, in which activity (activation energies), selectivity (binding energies) and importantly, reusability (stability of high-index crystal facets) are expected to strongly depend on their surface atomic structure, composition and accessibility. To study this point, the catalytic performance of the as-obtained multimetallic NTs using the reduction of 4-nitrophenol to 4-aminophenol by sodium borohydride ($NaBH_4$) as model reaction (**Scheme 3.2**) was evaluated [46]. The reaction was easily monitored by UV-vis spectroscopy following the decrease of the absorption peak of 4-nitrophenolate at λ_{max} = 400nm. During the entire process, the nanostructures acted as a catalyst to transfer electrons from BH_4^- to 4-nitrophenolate ions, enabling their reduction. Additionally, in the reaction system, the

concentration of BH_4^- was much higher than the concentration of 4-nitrophenol, so it was possible to consider its concentration as constant during the reaction.

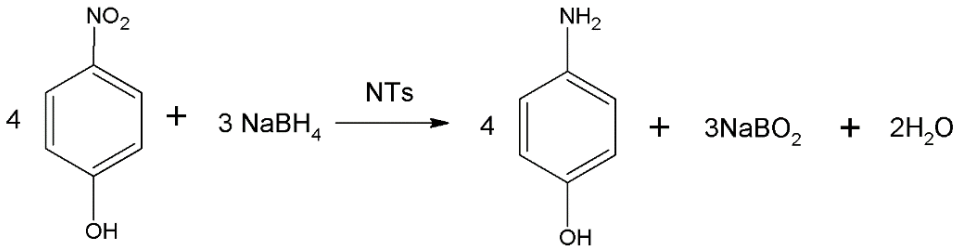

Scheme 3.2 Reduction of 4-nitrophenol to 4-aminophenol by $NaBH_4$, catalysed by multimetallic NTs.

The reduction process of 4-nitrophenol to 4-aminophenol was monitored by measuring the temporal evolution of UV-Vis absorption spectra of the reaction mixture in the presence of Ag NWs, bimetallic AgAu multidomain NTs, trimetallic AgAuPd, AgAuPt NTs and tetrametallic AgAuPdPt NTs synthesized step by step or with the simultaneous addition of the noble metal precursors (**Figure 3.14A-F**). To facilitate comparison, the characteristic absorption band at 400 nm was also plotted, offering a good linear correlation with first order kinetics (**Figure 3.14G-H**). As can be seen, the fastest reduction rate was found for tetrametallic AgAuPdPt NTs, evidencing that the presence of the four metals in a single structure synergistically enhanced the catalytic performance of the sample. The catalytic activity of trimetallic samples was found to slightly decrease, as the AgAuPd NTs were more active for the investigated reaction than the AgAuPt NTs. This can be explained in terms of Pd having greater catalytic activity than Pt. As expected, bimetallic AgAu multidomain NTs presented an even lower catalytic activity, on average for times lower than the tetrametallic catalysts. Finally, the Ag NWs were not able to efficiently catalyse the reduction reaction, which translated into a very low reaction rate constant, 2 orders of magnitude lower than that obtained for multimetallic NTs.

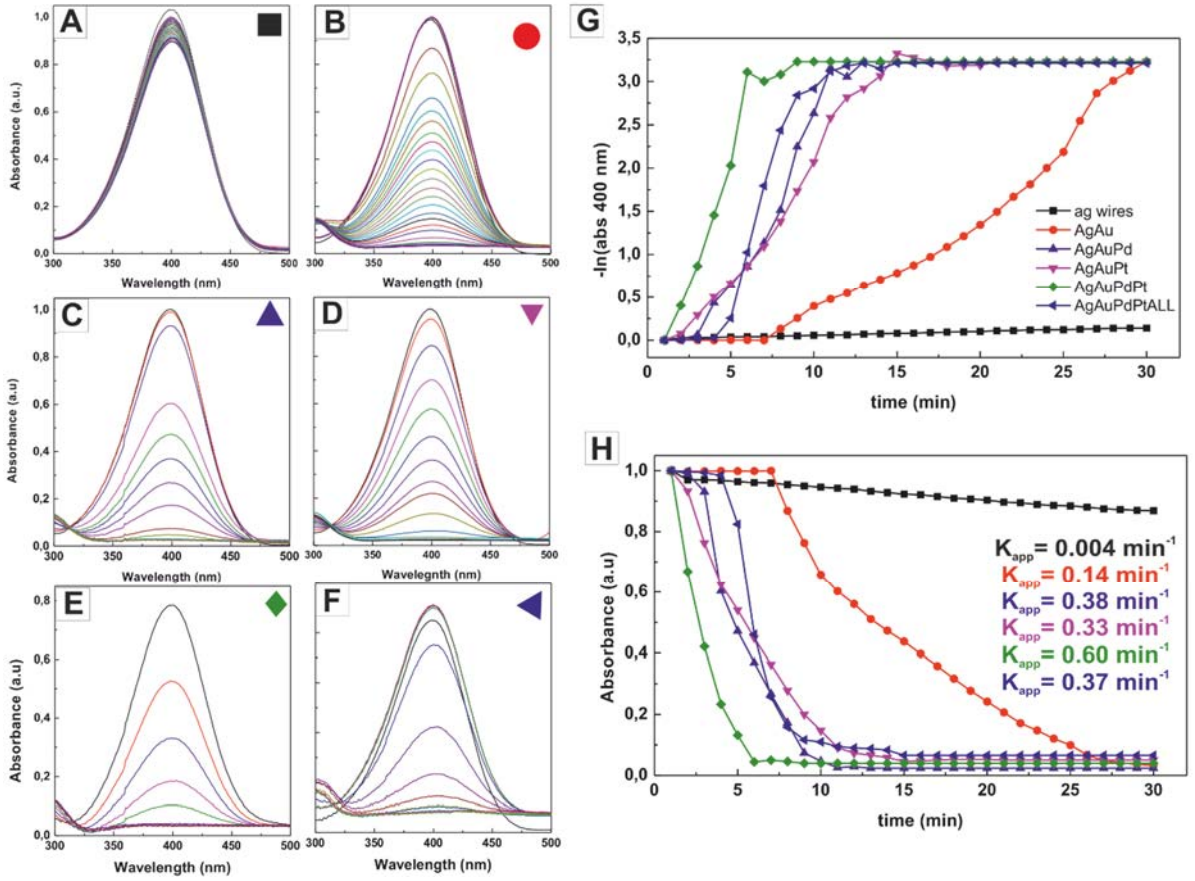

Figure 3.14 Time dependent UV-vis absorption spectra of the catalytic reduction of 4-nitrophenol to 4-aminophenol in the presence of: **A.** Ag NWs; **B.** AgAu multidomain NTs; **C.** AgAuPd NTs; **D.** AgAuPt NTs; **E.** AgAuPdPt NTs; **F.** AgAuPdPt (simultaneous addition). **G.** Kinetic trace of the absorbance at 400 nm during the reduction of 4-nitrophenol to 4-aminophenol. **H.** Kinetic rate constants.

3.4 References

1. Samal, A.K., et al., *Size Tunable Au@Ag Core–Shell Nanoparticles: Synthesis and Surface-Enhanced Raman Scattering Properties.* Langmuir, 2013. **29**(48): p. 15076-15082.
2. Chen, Z., et al., *Supportless Pt and PtPd Nanotubes as Electrocatalysts for Oxygen-Reduction Reactions.* Angewandte Chemie International Edition, 2007. **46**(22): p. 4060-4063.
3. Lim, B., et al., *Pd-Pt Bimetallic Nanodendrites with High Activity for Oxygen Reduction.* Science, 2009. **324**(5932): p. 1302-1305.
4. Zhou, S., G.S. Jackson, and B. Eichhorn, *AuPt Alloy Nanoparticles for CO-Tolerant Hydrogen Activation: Architectural Effects in Au-Pt Bimetallic Nanocatalysts.* Advanced Functional Materials, 2007. **17**(16): p. 3099-3104.
5. He, J., et al., *Facile Fabrication of Ag−Pd Bimetallic Nanoparticles in Ultrathin TiO2-Gel Films: Nanoparticle Morphology and Catalytic Activity.* Journal of the American Chemical Society, 2003. **125**(36): p. 11034-11040.
6. Scott, R.W.J., et al., *Bimetallic Palladium−Gold Dendrimer-Encapsulated Catalysts.* Journal of the American Chemical Society, 2004. **126**(47): p. 15583-15591.
7. Mahmoud, M.A., F. Saira, and M.A. El-Sayed, *Experimental Evidence For The Nanocage Effect In Catalysis With Hollow Nanoparticles.* Nano Letters, 2010. **10**(9): p. 3764-3769.
8. He, W., et al., *AuPt Alloy Nanostructures with Tunable Composition and Enzyme-like Activities for Colorimetric Detection of Bisulfide.* Scientific Reports, 2017. **7**: p. 40103.
9. Gu, X., et al., *Au-Ag alloy nanoporous nanotubes.* Nano Research, 2009. **2**(5): p. 386-393.
10. Hong, X., et al., *Ultrathin Au-Ag bimetallic nanowires with Coulomb blockade effects.* Chemical Communications, 2011. **47**(18): p. 5160-5162.
11. Peng, Z., H. You, and H. Yang, *Composition-Dependent Formation of Platinum Silver Nanowires.* ACS Nano, 2010. **4**(3): p. 1501-1510.
12. Kim, S.M., et al., *Synthesis of bimetallic Pt/Pd nanotubes and their enhanced catalytic activity in methanol electro-oxidation.* Journal of Materials Chemistry A, 2013. **1**(48): p. 15252-15257.
13. Yin, A.-X., et al., *Shape-Selective Synthesis and Facet-Dependent Enhanced Electrocatalytic Activity and Durability of Monodisperse Sub-10 nm Pt−Pd Tetrahedrons and Cubes.* Journal of the American Chemical Society, 2011. **133**(11): p. 3816-3819.
14. Wang, L. and Y. Yamauchi, *Controlled Aqueous Solution Synthesis of Platinum–Palladium Alloy Nanodendrites with Various Compositions Using Amphiphilic Triblock Copolymers.* Chemistry – An Asian Journal, 2010. **5**(12): p. 2493-2498.
15. Choi, B.-S., et al., *Multimetallic Alloy Nanotubes with Nanoporous Framework.* ACS Nano, 2012. **6**(6): p. 5659-5667.
16. Gu, J., Y.-W. Zhang, and F. Tao, *Shape control of bimetallic nanocatalysts through well-designed colloidal chemistry approaches.* Chemical Society Reviews, 2012. **41**(24): p. 8050-8065.
17. Yu, Y., et al., *Architectural Design of Heterogeneous Metallic Nanocrystals—Principles and Processes.* Accounts of Chemical Research, 2014. **47**(12): p. 3530-3540.
18. Zhang, H., et al., *Fabrication of catalytically active Au/Pt/Pd trimetallic nanoparticles by rapid injection of NaBH4.* Materials Research Bulletin, 2014. **49**: p. 393-398.
19. Venkatesan, P. and J. Santhanalakshmi, *Designed Synthesis of Au/Ag/Pd Trimetallic Nanoparticle-Based Catalysts for Sonogashira Coupling Reactions.* Langmuir, 2010. **26**(14): p. 12225-12229.
20. Khanal, S., et al., *Trimetallic nanostructures: the case of AgPd-Pt multiply twinned nanoparticles.* Nanoscale, 2013. **5**(24): p. 12456-12463.
21. Yang, J., J. Yang, and J.Y. Ying, *Morphology and Lateral Strain Control of Pt Nanoparticles via Core–Shell Construction Using Alloy AgPd Core Toward Oxygen Reduction Reaction.* ACS Nano, 2012. **6**(11): p. 9373-9382.

22. Kang, S.W., et al., *One-Pot Synthesis of Trimetallic Au@PdPt Core–Shell Nanoparticles with High Catalytic Performance.* ACS Nano, 2013. **7**(9): p. 7945-7955.
23. Wang, L. and Y. Yamauchi, *Autoprogrammed Synthesis of Triple-Layered Au@Pd@Pt Core−Shell Nanoparticles Consisting of a Au@Pd Bimetallic Core and Nanoporous Pt Shell.* Journal of the American Chemical Society, 2010. **132**(39): p. 13636-13638.
24. Song, Y. and S. Chen, *Trimetallic Ag@AuPt Neapolitan nanoparticles.* Nanoscale, 2013. **5**(16): p. 7284-7289.
25. Sun, Y. and Y. Xia, *Shape-Controlled Synthesis of Gold and Silver Nanoparticles.* Science, 2002. **298**(5601): p. 2176-2179.
26. Sun, Y., et al., *Synthesis and Optical Properties of Nanorattles and Multiple-Walled Nanoshells/Nanotubes Made of Metal Alloys.* Journal of the American Chemical Society, 2004. **126**(30): p. 9399-9406.
27. Chen, J., et al., *Optical Properties of Pd−Ag and Pt−Ag Nanoboxes Synthesized via Galvanic Replacement Reactions.* Nano Letters, 2005. **5**(10): p. 2058-2062.
28. Jing, H. and H. Wang, *Structural Evolution of Ag–Pd Bimetallic Nanoparticles through Controlled Galvanic Replacement: Effects of Mild Reducing Agents.* Chemistry of Materials, 2015. **27**(6): p. 2172-2180.
29. Zhang, H., et al., *Facile Synthesis of Pd–Pt Alloy Nanocages and Their Enhanced Performance for Preferential Oxidation of CO in Excess Hydrogen.* ACS Nano, 2011. **5**(10): p. 8212-8222.
30. Netzer, N.L., et al., *Gold-silver bimetallic porous nanowires for surface-enhanced Raman scattering.* Chemical Communications, 2011. **47**(34): p. 9606-9608.
31. Rodrigues, T.S., et al., *AgAu Nanotubes: Investigating the Effect of Surface Morphologies and Optical Properties over Applications in Catalysis and Photocatalysis.* Journal of the Brazilian Chemical Society, 2017. **28**: p. 1630-1638.
32. Luo, W.-B., et al., *Porous AgPd–Pd Composite Nanotubes as Highly Efficient Electrocatalysts for Lithium–Oxygen Batteries.* Advanced Materials, 2015. **27**(43): p. 6862-6869.
33. Schaefer, S., et al., *Double-Walled Ag–Pt Nanotubes Fabricated by Galvanic Replacement and Dealloying: Effect of Composition on the Methanol Oxidation Activity.* Nano, 2015. **10**(06): p. 1550085.
34. Chen, L., et al., *Advanced Catalytic Performance of Au–Pt Double-Walled Nanotubes and Their Fabrication through Galvanic Replacement Reaction.* Chemistry – A European Journal, 2013. **19**(35): p. 11753-11758.
35. Sun, H., et al., *Charge transfer accelerates galvanic replacement for PtAgAu nanotubes with enhanced catalytic activity.* Nano Research, 2016. **9**(4): p. 1173-1181.
36. Weiner, R.G., A.F. Smith, and S.E. Skrabalak, *Synthesis of hollow and trimetallic nanostructures by seed-mediated co-reduction.* Chemical Communications, 2015. **51**(42): p. 8872-8875.
37. Peng, Y., et al., *AgAuPt nanocages for highly sensitive detection of hydrogen peroxide.* RSC Advances, 2015. **5**(11): p. 7854-7859.
38. Sun, Y., et al., *Uniform Silver Nanowires Synthesis by Reducing AgNO3 with Ethylene Glycol in the Presence of Seeds and Poly(Vinyl Pyrrolidone).* Chemistry of Materials, 2002. **14**(11): p. 4736-4745.
39. Nair, K.G., D. Jayaseelan, and P. Biji, *Direct-writing of circuit interconnects on cellulose paper using ultra-long, silver nanowires based conducting ink.* RSC Advances, 2015. **5**(93): p. 76092-76100.
40. Jiang, X.C., et al., *Twinned Structure and Growth of V-Shaped Silver Nanowires Generated by a Polyol−Thermal Approach.* The Journal of Physical Chemistry C, 2011. **115**(5): p. 1800-1810.
41. Ghosh, T., B. Satpati, and D. Senapati, *Characterization of bimetallic core-shell nanorings synthesized via ascorbic acid-controlled galvanic displacement followed by epitaxial growth.* Journal of Materials Chemistry C, 2014. **2**(13): p. 2439-2447.

42. González, E., J. Arbiol, and V.F. Puntes, *Carving at the Nanoscale: Sequential Galvanic Exchange and Kirkendall Growth at Room Temperature.* Science, 2011. **334**(6061): p. 1377-1380.
43. Yingpu, B. and L. Gongxuan, *Controlled synthesis of pentagonal gold nanotubes at room temperature.* Nanotechnology, 2008. **19**(27): p. 275306.
44. Sun, Y., *Silver nanowires - unique templates for functional nanostructures.* Nanoscale, 2010. **2**(9): p. 1626-1642.
45. Sun, Y., et al., *Crystalline Silver Nanowires by Soft Solution Processing.* Nano Letters, 2002. **2**(2): p. 165-168.
46. Aditya, T., A. Pal, and T. Pal, *Nitroarene reduction: a trusted model reaction to test nanoparticle catalysts.* Chemical Communications, 2015. **51**(46): p. 9410-9431

Chapter 4

Silver Nanorods

In this chapter, a high yield, simple, and robust one-pot polyol method for the production of low aspect ratio (2.8) green silver nanorods (Ag NRs) is presented. In this method, the presence of tannic acid (TA), favours the nucleation of decahedral seeds needed for the production of monodisperse Ag NRs. These Ag NRs were further used as sacrificial templates to produce Au hollow nanostructures via galvanic replacement reaction with $HAuCl_4$ at room temperature. The synthesis, characterization and possible mechanism for the formation of Ag NRs is presented.

4.1 Introduction

Silver NRs are emerging as interesting materials with increasing importance, from the perspectives of both fundamental science and potential plasmonic and electronic applications [1-3]. Their unique size and shape-dependent physical and chemical properties make them attractive for many technologies including, among others, optical and flexible electronic devices, catalysis, surface enhanced Raman scattering (SERS)-active platforms, nanocarriers and (bio)sensing [1, 4-6].

The reproducible fabrication of highly monodisperse Ag NRs with controlled sizes is a challenging task. The first studies, pioneered by Murphy and co-workers [7], reported the production of cylindrical Ag NRs in water by the use of CTAB as a shape-directing agent and citrate-stabilized Ag seeds, which opened the possibility of solution phase methods for the growth of anisotropic metal nanostructures. However, the abundant presence of self-nucleating spherical and anisotropic (platelets and prisms) by-products, hamper reproducible synthesis. These restrictions arise from the difficulties in controlling the anisotropic growth of the Ag crystals after the nucleation of the Ag seeds, typically attributed to the lack of control of their crystal structure (a mixture of single crystal and penta-twinned phases) [8]. In this regard, the controlled production of Ag seeds with a decahedral structure has been reported as a necessary requirement to break the fcc symmetry and grow Ag anisotropic structures [9,

10]. However, this synthetic crystallographic control of Ag seeds is still difficult to achieve and only a few strategies have reported the controlled production of decahedral Ag seeds via complex time-consuming photochemical irradiation methods [11, 12]. Alternatively, high quality Ag NRs with a pentagonal cross section have been produced via seeded-growth strategies using well-faceted decahedral seeds of another metal, mainly Au or Pd [3, 9, 13-17]. An aqueous approach for the synthesis high aspect ratio Ag NRs and NWs using sodium citrate in the presence of sodium dodecylsulfonate, although the synthetic procedure is simple, the lack of monodispersity of the final products is an important factor to take into account [18].

The problem of seed crystalline dispersity has been partially overcome when producing long Ag nanowires (Ag NWs) by the solution-phase seeded-growth polyol approach [19-25], pioneered by Xia and co-workers. Although extensive research has been performed in this system [24-26], this route has been limited to the production of high aspect ratio Ag NWs with relatively large diameters (> 40 nm) and, more importantly, highly polydisperse lengths up to 50 μm. In this regard, especially interesting is the work of El-Sayed and co-workers [27] who reported the possibility of obtaining short Ag NRs of ∼20 nm in diameter and different lengths, by the temporal quenching of the Ag NWs growth process. Nevertheless, this technique resulted in very low Ag conversion rates and reaction yields.

However, the relatively large and polydisperse size of standard Ag seeds, the lack of synthetic control of their crystallinity (often a mixture between single crystal and dodecahedral), and the tendency to form abundant by- products in their production, limit the control of the final Ag NR morphology [11, 12]. Additionally, there are multiple synthetic steps involved in most preparation procedures, which entail tedious post-processing protocols and limit the accurate, reproducible and robust production of Ag NR structures. As a result, it remains difficult to synthesize Ag NRs with controlled sizes and low aspect ratios in high yields and with fairly monodisperse distributions.

Herein, we take advantage of a well-established polyol synthesis of Ag nanostructures to report a simple and robust kinetically controlled one-pot method for the synthesis of short Ag NRs in high yield. With this method, ~94% of Ag precursor was converted into Ag products with a high degree of morphological control (>80% of the products were Ag NRs). These short Ag NRs have an exceptional colloidal stability and a high absorbance in the visible range. Here

the controlled formation and growth of Ag NRs with an average length of 55 nm and diameter of 19 nm is achieved by the use of tannic acid (TA) as co-reducing agent at substoichiometric concentrations [28, 29] in the ethylene glycol (EG) reduction of CF_3COOAg in the presence of high molecular weight PVP (MW 1,300,000). As previously reported,[29-31] the use of a co-reducer favours the massive nucleation of monodisperse seeds, which further grow by the incorporation of the remaining precursor in solution, leading to the high yield production of highly monodisperse low aspect ratio (2.8) Ag NRs. These Ag NRs can be further grown or used as sacrificial templates to produce Au hollow nanostructures via galvanic replacement reaction (GRR) with $HAuCl_4$, which reveals their homogeneous crystal structure.

4.2 Materials and methods.

4.2.1 Materials

Ethyleneglycol anhydrous, 99.8% (EG), silver trifluoroacetate (CF_3COOAg), silver nitrate ($AgNO_3$), hydrochloric acid (HCl), polyvinylpyrrolidone (PVP, MW 1,300,000; 350,000), tannic acid (TA), gold (III) chloride trihydrate >99,9% ($HAuCl_4 \cdot 3H_2O$) and cetyltrimethylammonium bromide ≥ 99% (CTAB) were purchased from Sigma-Aldrich. All chemicals were used as received without further purification. Distilled water passed through a Millipore system (ρ = 18.2 mΩ) was used in all experiments.

4.2.2 Methods

4.2.2.1 Synthesis of Ag NRs. In a typical procedure, 5 mL of EG were added to a 100 mL three necked round bottom flask, and heated under magnetic stirring in an oil bath pre-set to 170°C. After 10 min, 60 μL of TA (30 mM in EG to a final concentration 0.25mM) was injected into the flask. 0.5 mL of HCl solution (3 mM in EG) was then injected into the reaction solution, followed by the addition of 1.25 mL PVP, (20 mg/mL) into the reaction solution. Finally, 0.4 mL of CF_3COOAg (282 mM in EG) was added into the mixture. After 20 min the reaction was stopped by placing the reaction flask in an ice-water bath. Resultant Ag NPs were purified by centrifugation (8000g) in order to remove the EG the excess of TA and PVP, and further redispersed in MQW before sample characterization.

4.2.2.2 Synthesis of AgAu hollow alloy NRs. In a typical procedure, 0.25 mL of Ag NRs (10^{12} NPs/mL) were dispersed in 2 mL of MilliQ water, then 1 mL of CTAB (20 mM) and 10 μL

of ascorbic acid (15 mM) were added. 0.3 mL of a solution of $HAuCl_4$ (1mM) was injected at a rate of 25 μL/min using a syringe pump. The reaction was stirred for 30 min and the product were collected by centrifugation (8000g for 10 min) and then suspended in water for further characterization.

4.2.2.3 Characterization

Absorption spectra of the as synthesized Ag NPs were acquired with a Shimadzu UV-2401 PC spectrophotometer. An aliquot of the NPs solution was placed in a cuvette, and spectral analysis was performed in the 300−800 nm range at room temperature.

The morphology and size of the NPs were visualized using FEI Magellan 400L XHR SEM, in transmission mode, operated at 20 kV. STEM/ HAADF images were obtained in a FEI Tecnai G2 F20 S-TWIN HR(S) TEM, operated at an accelerated voltage of 200 kV. A droplet of the sample was drop cast onto a piece of ultrathin carbon-coated 200-mesh copper grid (Ted-pella, Inc.) and left to dry in air. XRD data were collected on a PANalytical X'Pert diffractometer using a Cu Kα radiation source.

4.3 Results

4.3.1 Synthesis of Ag NRs. In the method present in this chapter, EG acts as both, solvent and reducing agent. In a typical synthesis of Ag NRs, an EG solution, containing a specific amount of CF_3COOAg, high molecular weight PVP (MW 1,300,000) and TA, is heated to 170°C in a silicon oil bath under magnetic stirring for 20 min. The solution turns from yellow to orange, red and finally intense green after 15 minutes as shown in **Figure 4.5** inset. It is then cooled down and prepared for analysis.

HAADF-STEM images of the obtained product, shown in **Figure 4.1A** and **D**, together with TEM images, shown in **Figure 4.1B**, demonstrate that the as-obtained product consists of uniform Ag NRs with an average length of 55.6 ± 9.3 nm and average diameter of 19.3 ± 3.0 nm (see **Figure 4.1C**). The average aspect ratio of these Ag NRs is 2.8. The image contrast variations within the same Ag NRs as shown in **Figure 4.1E,** suggest the presence of a multi-twinned structure. This is confirmed in **Figure 4.1F** which shows an HR-TEM image of a single Ag NR, in which the presence of twin boundaries is clearly visible. From one of the facets on the edge, it is possible to identify the face centered cubic (f.c.c.) Ag phase. Details of the red

squared region and its corresponding fast Fourier transformation patterns are shown on **Figure 4.1G**, indicating that the NR is composed of f.c.c. Ag phase with a lattice parameter of a = 0.408 nm, and this particular facet is visualized along its [011] zone axis.

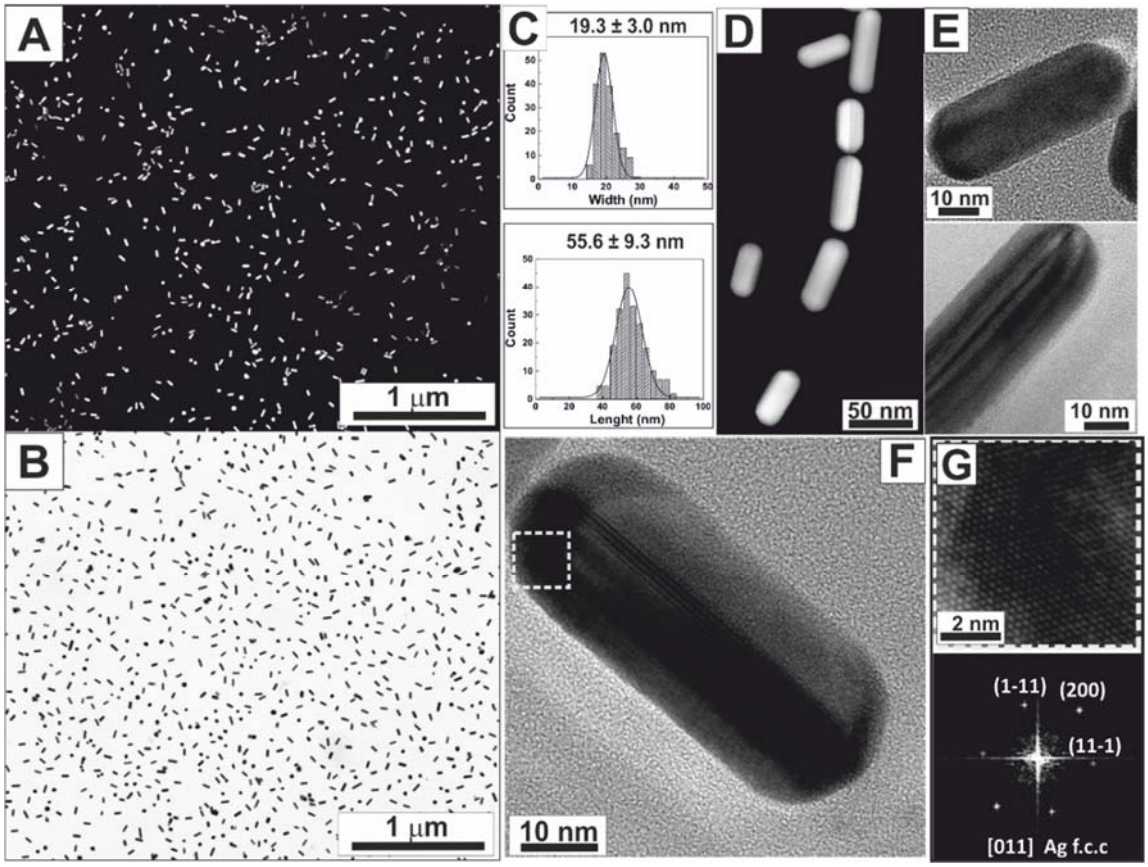

Figure 4.1 A. Low magnification HAADF-STEM image. **B.** Low magnification TEM image **C.** Particle size distribution of Ag NRs. Upper: width, bottom: Length. **D.** HAADF-STEM image **E** and **F**. TEM images of Ag NRs. **G**. HRTEM image of the red squared area in F and its corresponding power spectrum

Figure 4.2A shows the UV−Vis spectrum of the as synthesized Ag NRs. Interestingly, these Ag NRs exhibit two strong absorption bands, located at 410 and 625 nm, which can be assigned to the transverse and longitudinal SPRs respectively. The as-prepared colloidal sample appears intense green, as displayed in the **Figure 4.2B**, which is definitely different from the colour of spherical Ag NPs (yellow) and Ag NWs (white) [22, 28]. **Figure 4.2C** shows the measured XRD patterns, in which four diffraction peaks can be seen, indexed as (111), (200), (220) and (311) planes, which can be attributed to the fcc structure of Ag (JCPDS file No. 04-0783, red dot lines). The alterations in the XRD peak intensity profile with respect to the standards (the 111 peak is enhanced), and the differences in the peak width measured at

medium height (the 111 peak is narrower), accounts for the anisotropic growth of the rods in the [111] crystal direction. No diffractions peaks due to impurities, Ag precursor or Ag_2O were observed.

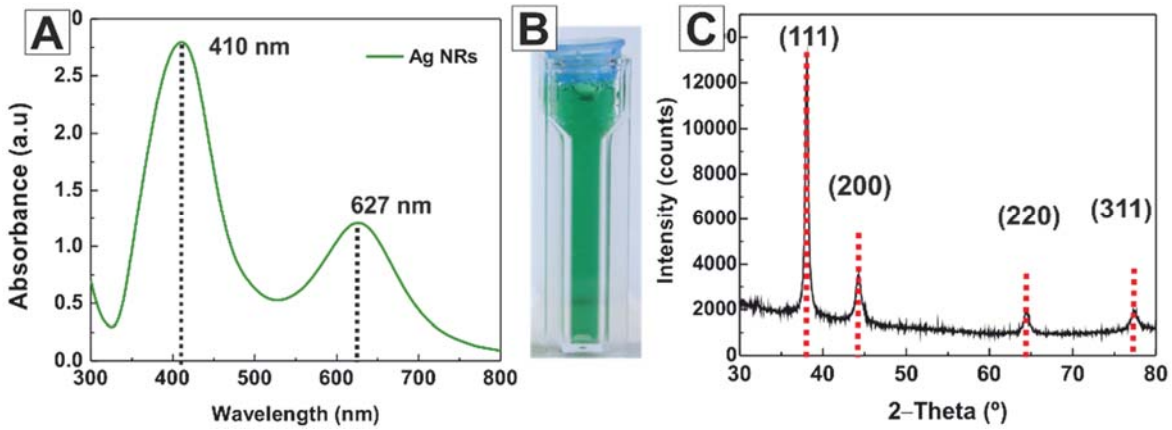

Figure 4.2 A. UV–Vis spectrum of the as synthesized Ag NRs **B.** Photograph of aqueous dispersion of Ag NRs. **C.** XRD patterns of Ag NRs, in red bulk positions and relative intensities of the different diffraction peaks.

In order to evaluate the reproducibility of the method, four independent syntheses were performed. The results shown in **Figure 4.3**, suggest a good reproducibility of the method, due to the high abundance of Ag NRs in all cases (>80%). The average width and length are 20.8 ± 2.2 and 56.3 ± 6.7 nm, respectively. The average position of the transversal and longitudinal absorptions bands are 405 ± 5.3 and 615 ± 8.0 nm respectively.

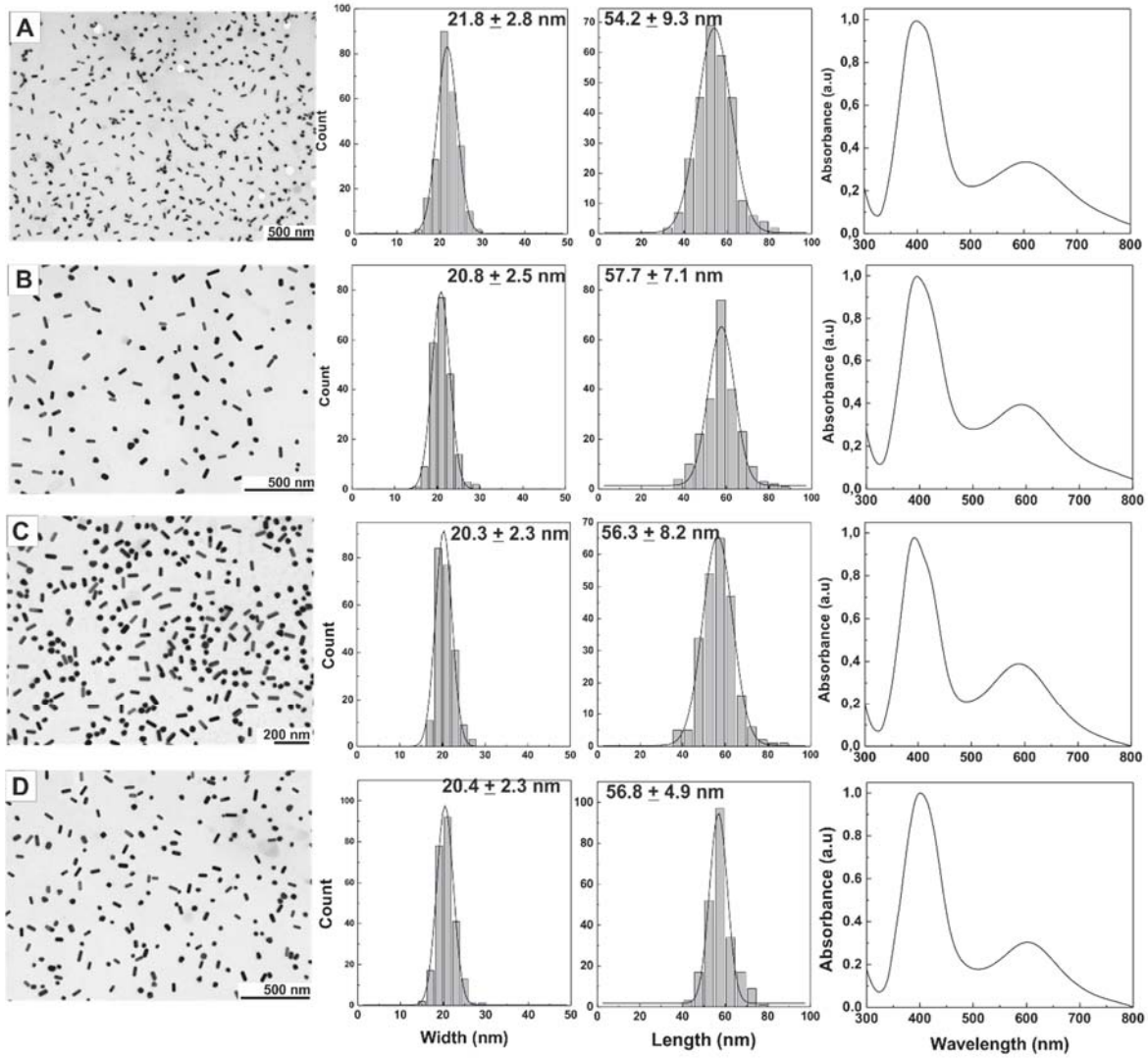

Figure 4.3 TEM images, particle size distribution and UV-vis spectra of 4 (**A-D**) synthesis of Ag NRs.

Regarding the mechanism, the key factors for the reproducible production of Ag NRs in high yields are i) the use of TA as a co-reducing agent, ii) the presence of high molecular weight PVP (MW 1,300,000), iii) relatively high temperatures, and iv) the use of CF_3COOAg as source of Ag^+ ions.

4.3.1.1. Effect of tannic acid (TA). In detail, the role of TA at low concentration is to produce the initial rapid reduction of a fraction of the Ag precursor [28], which at the given conditions, results in the production of decahedral seeds. Once the TA has been exhausted, EG slowly reduces the remaining Ag precursor promoting the uniform growth of the formed seeds, avoiding conditions for new nucleation of NPs and consequently the formation of by-products, as shown in **Scheme 4.1** [28, 32].

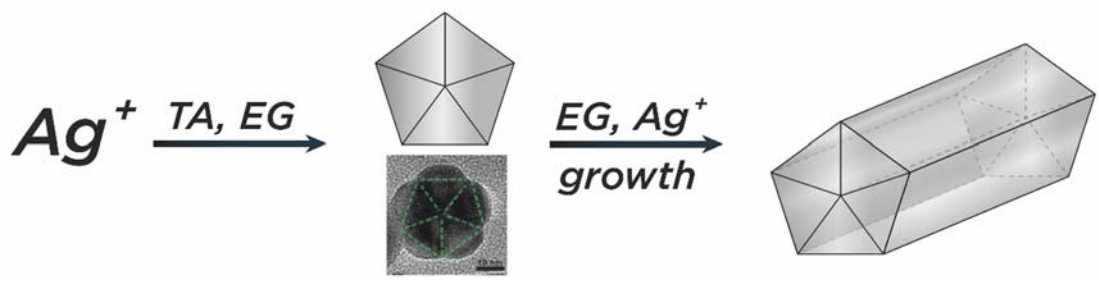

Scheme 4.1 Representation of Ag NRs formation. Decahedral seeds are produced by reduction of Ag^+ precursor in the presence of TA. Further growth of these Ag seeds with remaining Ag produces Ag NRs.

In control experiments, the yield of Ag NRs dramatically decreased (down to 10%) by performing the reaction in the absence of TA, leading to the production of a large number of by-products such as spherical NPs, nanoplateles and NCs, and only a small fraction of Ag NRs, which were heterogeneous in length and diameter (**Figure 4.4A**, left). As expected, the effect of TA on the final yield and morphology of Ag NRs was concentration dependent. Thus, when the final concentration of TA was increased from 0.0025 mM to 0.025 mM (**Figure 4.4A**, center and right) the amount of by-products decreased. When the concentration was fixed at 0.25 mM Ag NRs, a high morphological control (>80%) was obtained (**Figure 4.4C**).

4.3.1.2 Effect of PVP. As previously discussed, the formation of decahedral seeds is necessary for the anisotropic growth of Ag NRs [33] assisted by the presence of high molecular weight PVP. It is well known that the high molecular weight of PVP binds preferentially on the side of {100} facets of the multiple twined Ag crystals [11, 34-37] leading to the facile deposition of Ag atoms onto the {111} facets. In addition, variations in the molecular weight of PVP also allow control of the morphology and yield of the final products. Thus, while the use of PVP with a high molecular weight (MW 1,300,000) favoured the formation of uniform Ag NRs, experiments performed using a PVP with a lower molecular weight (MW 360,000) led to the formation of Ag NRs with a low aspect ratio (2.2), together with a large amount of spherical by-products, as shown in **Figure 4.4B.** When the PVP with the lowest molecular weight (MW 10,000) was used, the reaction aggregate after a few minutes of the addition of the Ag precursor. These results indicate the importance of the PVP molecular weight or length for the colloidal stabilization of the Ag nanostructures formed during the polyol reaction.

4.3.1.3 Effect of Ag Precursor. Another control parameter is the reactivity of the Ag precursor. The formation of Ag NRs of low aspect ratio was successfully achieved when using CF_3COOAg as a precursor, while the choice of $AgNO_3$, widely used in the standard polyol synthesis, consistently led to the formation of heterogeneous Ag NWs together with different by-products, as shown in **Figure 4.4D**, this result was probably due to the higher stability of the trifluoroacetate group [38, 39], since as previous studies suggest the nitrate group may decompose at elevated temperatures generating ionic and/or gaseous oxidant species which can interfere with the NRs formation process [39].

4.3.1.4 Effect of temperature. Results demonstrate that the morphology of Ag NRs also strongly depends on the reduction rate of Ag^+ ions, which is ultimately determined by the reaction temperature. Thus, running the reaction at 120°C the reducing strength of EG was not enough to drive the growth of Ag NRs, resulting in a final spherical product (**Figure 4.4E**, left), whereas the increase in temperature to 170°C increased the abundance of Ag NRs (**Figure 4.4.E**, centre). When the reaction was carried out at reflux (197°C), the number of by-products increased dramatically (**Figure 4.4E**, right). Taken together, we found that the best results were obtained at 170°C, with PVP of high molecular weight (MW 1,300,000), using CF_3COOAg as silver precursor, in the presence of TA at 0.25 mM and traces of HCl (**Figure 4.4C**).

As previously reported [40, 41], the addition of small amounts of HCl has an outstanding impact on the control of the final structure of Ag NRs, which can be associated with Ag surface adsorption. Thus, the presence of Cl^- assists the anisotropic growth of the Ag NRs via the stabilization of certain facets to direct the synthesis toward a precise crystallographic structure by forming AgCl domains [42].

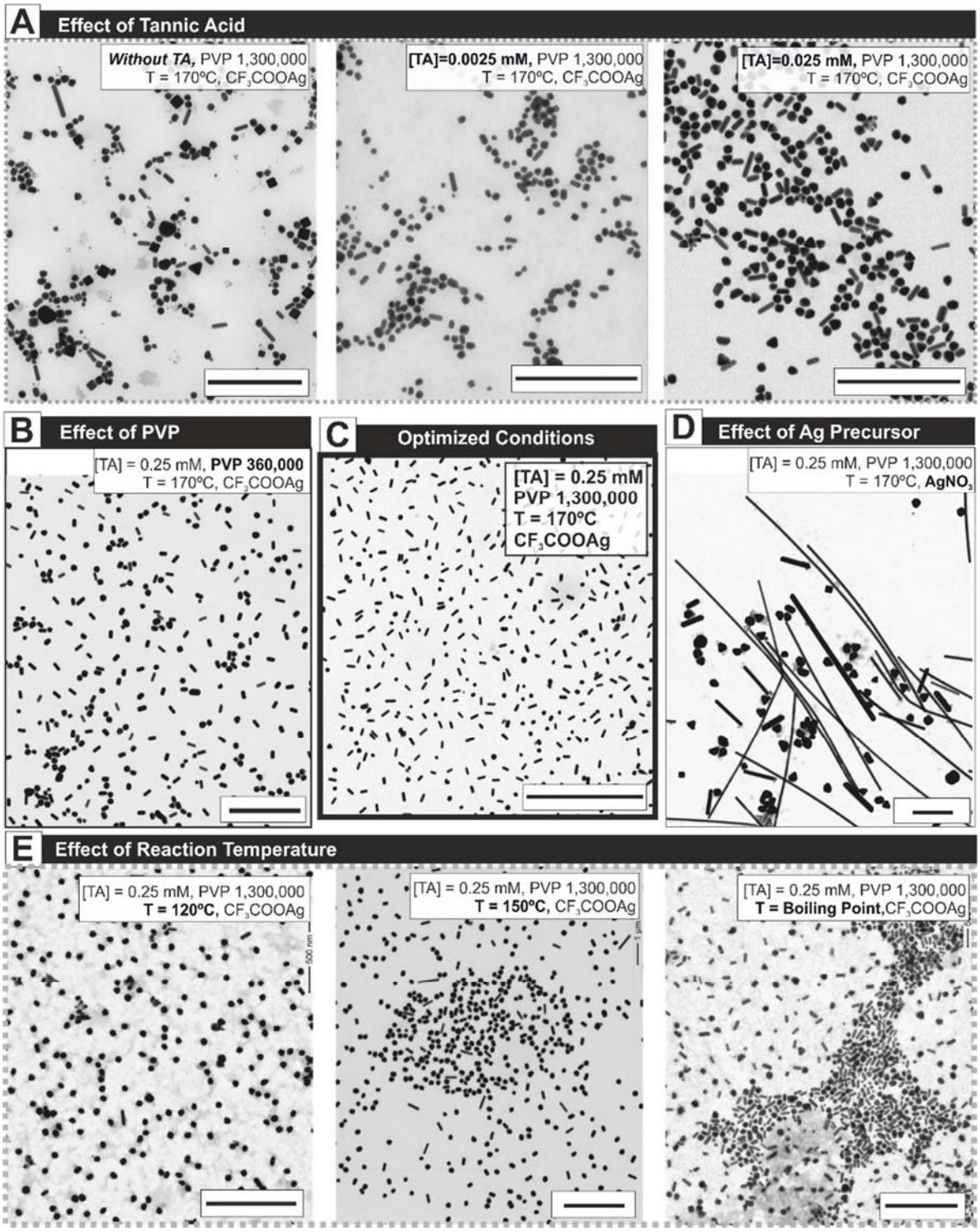

Figure 4.4 TEM image of samples obtained according to variation of: **A.** Concentration of TA. **B.** PVP molecular weight. **C.** TEM image of samples obtained after optimization of reaction parameters. **D.** Ag precursor. **E.** Reaction temperature. Scale bar is 500 nm for all images.

The different sets of experiments performed suggest the possibility of controlling (to some extent) the aspect ratio of the final Ag NRs by carefully adjusting synthetic conditions, in particular the reaction time. Thus, by decreasing the reaction time, the aspect ratio of the observed Ag NRs was lower (see **Figure 4.5**). However, this is associated with a decrease in the reaction yield, which suggests that Ag NRs grow by incorporation of Ag precursor from solution. The time-dependent UV-vis spectra in **Figure 4.5** show a systematic red-shift of longitudinal and transversal plasmonic bands, which can be univocally associated with an increase in the aspect ratio of Ag NRs.

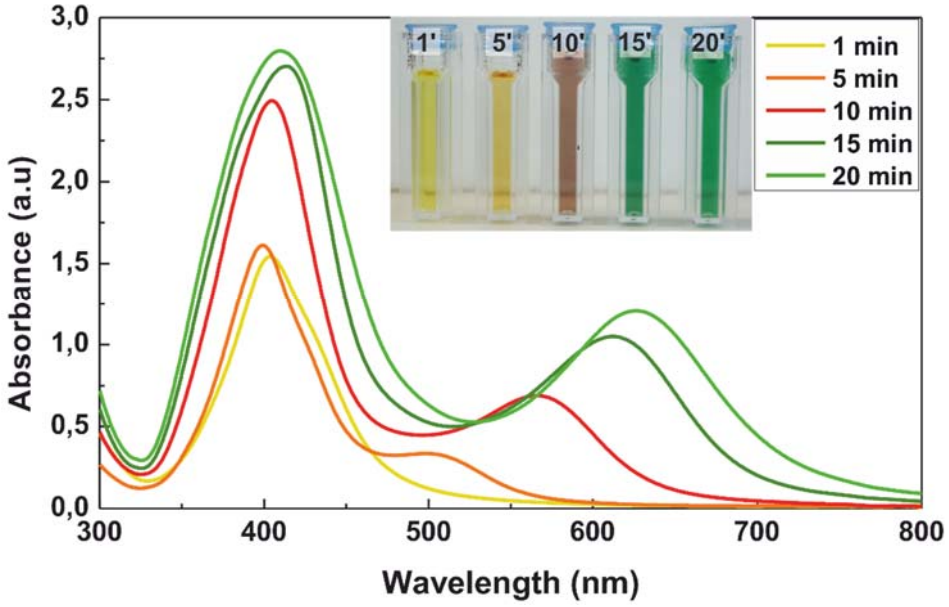

Figure 4.5. Time-dependent UV-vis spectra and photographs of aqueous dispersion of Ag NR at different times, 1 min, 5 min, 10 min, 15 min and 20 min.

4.3.2. Synthesis of hollow AgAu NRs. The produced Ag NRs can be transformed into noble-metal hollow AgAu NRs, via GRR at room temperature [43, 44]. This reaction, sensitive to the chemical (oxidation state) and the physical (accessibility) nature of the surface and core Ag atoms, has been reported as standard techniques to produce exotic noble metal structures with hollow interiors, exhibiting unique physicochemical properties [43, 45, 46]. **Figure 4.6A** shows TEM and HR-TEM images of the Au-based hollow nanostructures obtained by adding a specific amount of $HAuCl_4$ to an aqueous suspension of the Ag NRs in the presence of CTAB. As previous studies show, the use of CTAB as complexing agent assists the formation of Au complexes [47, 48], which controls the reactivity of the Au salt [49], solubilizing at the same time the Ag insoluble species (AgCl) formed during the reaction [43]. As a result, highly

crystalline hollow AgAu alloy nanostructures were obtained. Details of the indicated regions in **Figure 4.6A** (FFT shown in inset) reveal the crystallinity of the obtained alloy structures, composed of an fcc AgAu phase [43]. **Figure 4.6B** shows HAADF-STEM images of the final hollow nanostructures where it can be clearly seen how they are faceted and retain the 5-twinned rod-like morphology of the original Ag NRs.

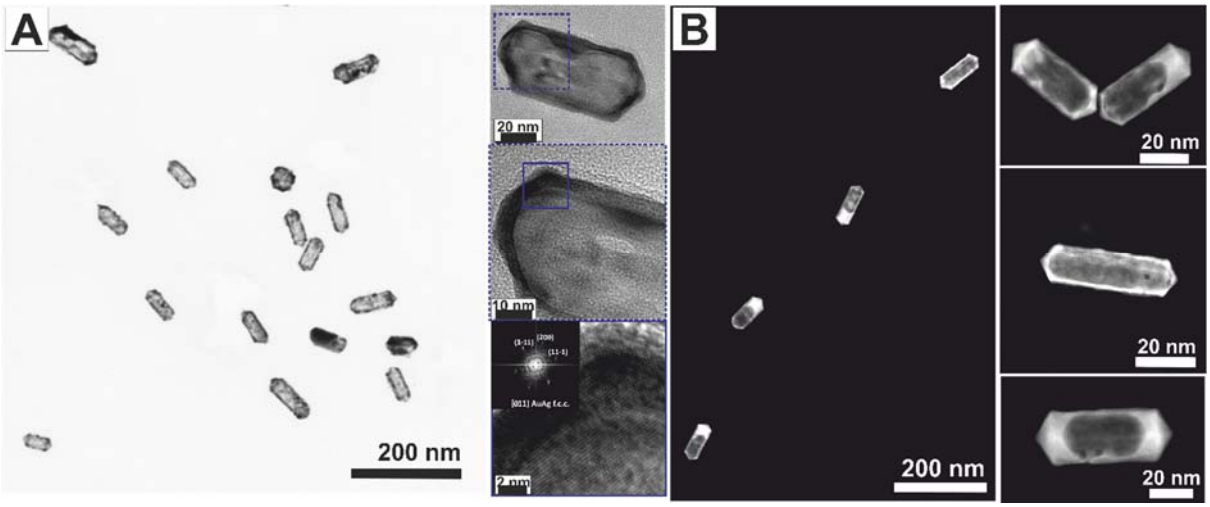

Figure 4.6. A. TEM and HR-TEM images of hollow AgAu alloy NRs. Inset is the corresponding power spectrum of the HR-TEM image. **B.** HAADF STEM images of hollow AgAu alloy NRs.

Figure 4.7A shows the STEM-EDS line scans obtained over the longitudinal (blue) and transverse (yellow) section of the hollow NRs. Elemental mapping profiles of Ag (red line) and Au (green line) indicate that end tips of the NR were mostly rich in Ag and covered by an outer thin (< 1nm) Au layer. Interestingly, despite the high uniformity, some of the obtained hollow structures presented some in-homogeneities in terms of degree of voiding. This is associated with the limited range in GRR for mass transfer. **Figure 4.7B** shows the UV-vis absorption spectra of a colloidal solution of as-synthesized Ag NRs before (dotted line), and after (hollow AgAu NRs, solid line), the addition of Au^{3+} precursor solution. Interestingly, the characteristic Ag absorption band at ~410 nm progressively vanishes while a new band at ~700 nm, corresponding to the LSPR band of the hollow AgAu NRs, gradually rises. Such hollow nanostructures strongly absorb in the water window (near infra-red) which opens their applicability in biomedicine such as photo-thermally triggered drug release, optical imaging, and cancer phototherapy [50].

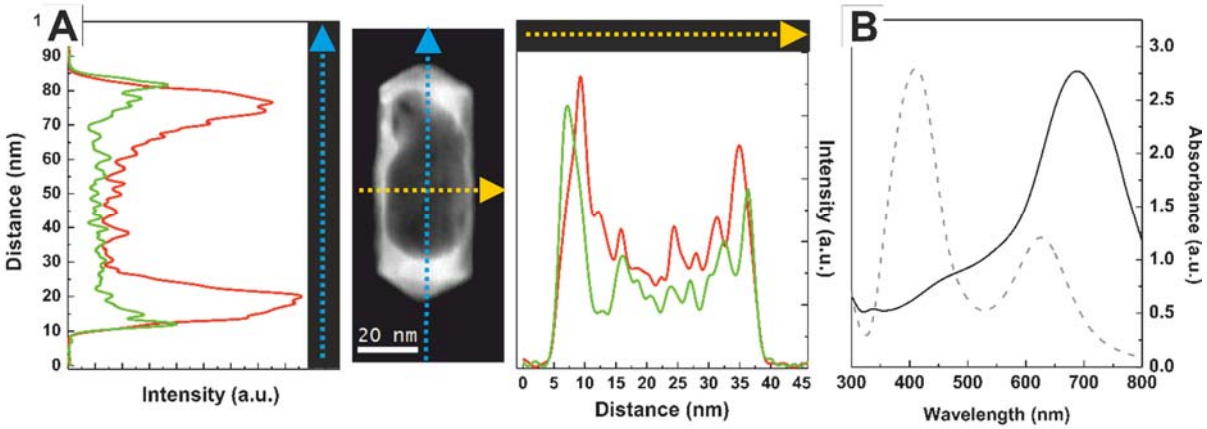

Figure 4.7. A. HAADF-STEM images of a single hollow AgAu alloy NR and EDS line scan results through the blue (left) and yellow (right) arrow, where red line correspond to Ag and green line to Au. **B.** UV-Vis absorption spectra of Ag NRs (grey-dotted line) and AgAu hollow alloy NRs (black line).

4.4 References

1. Rycenga, M., et al., *Controlling the Synthesis and Assembly of Silver Nanostructures for Plasmonic Applications.* Chemical Reviews, 2011. **111**(6): p. 3669-3712.
2. Jakab, A., et al., *Highly Sensitive Plasmonic Silver Nanorods.* ACS Nano, 2011. **5**(9): p. 6880-6885.
3. Tian, X.-D., et al., *Synthesis of Ag Nanorods with Highly Tunable Plasmonics toward Optimal Surface-Enhanced Raman Scattering Substrates Self-Assembled at Interfaces.* Advanced Optical Materials: p. 1700581-n/a.
4. Wiley, B., et al., *Shape-Controlled Synthesis of Metal Nanostructures: The Case of Silver.* Chemistry – A European Journal, 2005. **11**(2): p. 454-463.
5. Liu, Y., et al., *Polyvinylpyrrolidone–Poly(ethylene glycol) Modified Silver Nanorods Can Be a Safe, Noncarrier Adjuvant for HIV Vaccine.* ACS Nano, 2016. **10**(3): p. 3589-3596.
6. Karthiga, D., et al., *Determination of mercury(ii) ions in aqueous solution using silver nanorods as a probe.* Analytical Methods, 2016. **8**(18): p. 3756-3762.
7. Jana, N.R., L. Gearheart, and C.J. Murphy, *Wet chemical synthesis of silver nanorods and nanowires of controllable aspect ratio.* Chemical Communications, 2001(7): p. 617-618.
8. Zhang, Q. and Y. Yin, *Beyond spheres: Murphy's silver nanorods and nanowires.* Chemical Communications, 2013. **49**(3): p. 215-217.
9. Xiang, Y., et al., *Gold Nanorod-Seeded Growth of Silver Nanostructures: From Homogeneous Coating to Anisotropic Coating.* Langmuir, 2008. **24**(7): p. 3465-3470.
10. Luo, M., et al., *Facile Synthesis of Ag Nanorods with No Plasmon Resonance Peak in the Visible Region by Using Pd Decahedra of 16 nm in Size as Seeds.* ACS Nano, 2015. **9**(10): p. 10523-10532.
11. Pietrobon, B., M. McEachran, and V. Kitaev, *Synthesis of Size-Controlled Faceted Pentagonal Silver Nanorods with Tunable Plasmonic Properties and Self-Assembly of These Nanorods.* ACS Nano, 2009. **3**(1): p. 21-26.

12. Zhang, J., M.R. Langille, and C.A. Mirkin, *Synthesis of Silver Nanorods by Low Energy Excitation of Spherical Plasmonic Seeds.* Nano Letters, 2011. **11**(6): p. 2495-2498.
13. Becker, J., et al., *Plasmonic Focusing Reduces Ensemble Linewidth of Silver-Coated Gold Nanorods.* Nano Letters, 2008. **8**(6): p. 1719-1723.
14. Seo, D., et al., *Ag−Au−Ag Heterometallic Nanorods Formed through Directed Anisotropic Growth.* Journal of the American Chemical Society, 2008. **130**(10): p. 2940-2941.
15. Jiang, R., et al., *Unraveling the Evolution and Nature of the Plasmons in (Au Core)–(Ag Shell) Nanorods.* Advanced Materials, 2012. **24**(35): p. OP200-OP207.
16. Zhang, W., et al., *Growth of Au@Ag Core–Shell Pentatwinned Nanorods: Tuning the End Facets.* Chemistry – A European Journal, 2013. **19**(38): p. 12732-12738.
17. Xu, H., et al., *Synthesis of high-purity silver nanorods with tunable plasmonic properties and sensor behavior.* Photonics Research, 2017. **5**(1): p. 27-32.
18. J.-Q., H., et al., *A Simple and Effective Route for the Synthesis of Crystalline Silver Nanorods and Nanowires.* Advanced Functional Materials, 2004. **14**(2): p. 183-189.
19. Chen, C., et al., *Study on the growth mechanism of silver nanorods in the nanowire-seeding polyol process.* Materials Chemistry and Physics, 2008. **107**(1): p. 13-17.
20. Guo, S., S. Dong, and E. Wang, *Rectangular Silver Nanorods: Controlled Preparation, Liquid−Liquid Interface Assembly, and Application in Surface-Enhanced Raman Scattering.* Crystal Growth & Design, 2009. **9**(1): p. 372-377.
21. Jiu, J., et al., *Preparation of Ag nanorods with high yield by polyol process.* Materials Chemistry and Physics, 2009. **114**(1): p. 333-338.
22. Sun, Y., et al., *Crystalline Silver Nanowires by Soft Solution Processing.* Nano Letters, 2002. **2**(2): p. 165-168.
23. Sun, Y., et al., *Polyol Synthesis of Uniform Silver Nanowires: A Plausible Growth Mechanism and the Supporting Evidence.* Nano Letters, 2003. **3**(7): p. 955-960.
24. Sun, Y., et al., *Uniform Silver Nanowires Synthesis by Reducing AgNO3 with Ethylene Glycol in the Presence of Seeds and Poly(Vinyl Pyrrolidone).* Chemistry of Materials, 2002. **14**(11): p. 4736-4745.
25. Wiley, B.J., et al., *Maneuvering the Surface Plasmon Resonance of Silver Nanostructures through Shape-Controlled Synthesis.* The Journal of Physical Chemistry B, 2006. **110**(32): p. 15666-15675.
26. Maiyalagan, T., *Synthesis, characterization and electrocatalytic activity of silver nanorods towards the reduction of benzyl chloride.* Applied Catalysis A: General, 2008. **340**(2): p. 191-195.
27. Mahmoud, M.A. and M.A. El-Sayed, *Different Plasmon Sensing Behavior of Silver and Gold Nanorods.* The Journal of Physical Chemistry Letters, 2013. **4**(9): p. 1541-1545.
28. Bastús, N.G., et al., *Synthesis of Highly Monodisperse Citrate-Stabilized Silver Nanoparticles of up to 200 nm: Kinetic Control and Catalytic Properties.* Chemistry of Materials, 2014. **26**(9): p. 2836-2846.
29. Piella, J., N.G. Bastús, and V. Puntes, *Size-Controlled Synthesis of Sub-10-nanometer Citrate-Stabilized Gold Nanoparticles and Related Optical Properties.* Chemistry of Materials, 2016. **28**(4): p. 1066-1075.
30. Lim, S.I., et al., *Synthesis of Platinum Cubes, Polypods, Cuboctahedrons, and Raspberries Assisted by Cobalt Nanocrystals.* Nano Letters, 2010. **10**(3): p. 964-973.
31. Lim, S.I., et al., *Exploring the Limitations of the Use of Competing Reducers to Control the Morphology and Composition of Pt and PtCo Nanocrystals.* Chemistry of Materials, 2010. **22**(15): p. 4495-4504.
32. Bastús, N.G., J. Comenge, and V. Puntes, *Kinetically Controlled Seeded Growth Synthesis of Citrate-Stabilized Gold Nanoparticles of up to 200 nm: Size Focusing versus Ostwald Ripening.* Langmuir, 2011. **27**(17): p. 11098-11105.

33. Huang, H., et al., *Five-Fold Twinned Pd Nanorods and Their Use as Templates for the Synthesis of Bimetallic or Hollow Nanostructures.* ChemNanoMat, 2015. **1**(4): p. 246-252.
34. Al-Saidi, W.A., H. Feng, and K.A. Fichthorn, *Adsorption of Polyvinylpyrrolidone on Ag Surfaces: Insight into a Structure-Directing Agent.* Nano Letters, 2012. **12**(2): p. 997-1001.
35. Saidi, W.A., H. Feng, and K.A. Fichthorn, *Binding of Polyvinylpyrrolidone to Ag Surfaces: Insight into a Structure-Directing Agent from Dispersion-Corrected Density Functional Theory.* The Journal of Physical Chemistry C, 2013. **117**(2): p. 1163-1171.
36. Tsuji, M., et al., *Effects of chain length of polyvinylpyrrolidone for the synthesis of silver nanostructures by a microwave-polyol method.* Materials Letters, 2006. **60**(6): p. 834-838.
37. Xia, X., et al., *Recent Developments in Shape-Controlled Synthesis of Silver Nanocrystals.* The Journal of Physical Chemistry C, 2012. **116**(41): p. 21647-21656.
38. Ruditskiy, A. and Y. Xia, *Toward the Synthesis of Sub-15 nm Ag Nanocubes with Sharp Corners and Edges: The Roles of Heterogeneous Nucleation and Surface Capping.* Journal of the American Chemical Society, 2016. **138**(9): p. 3161-3167.
39. Zhang, Q., et al., *Facile Synthesis of Ag Nanocubes of 30 to 70 nm in Edge Length with CF3COOAg as a Precursor.* Chemistry – A European Journal, 2010. **16**(33): p. 10234-10239.
40. Gómez-Graña, S., et al., *Au@Ag Nanoparticles: Halides Stabilize {100} Facets.* The Journal of Physical Chemistry Letters, 2013. **4**(13): p. 2209-2216.
41. Li, Q., et al., *Crystalline structure-dependent growth of bimetallic nanostructures.* Nanoscale, 2012. **4**(22): p. 7070-7077.
42. Lohse, S.E., et al., *Anisotropic Noble Metal Nanocrystal Growth: The Role of Halides.* Chemistry of Materials, 2014. **26**(1): p. 34-43.
43. González, E., J. Arbiol, and V.F. Puntes, *Carving at the Nanoscale: Sequential Galvanic Exchange and Kirkendall Growth at Room Temperature.* Science, 2011. **334**(6061): p. 1377-1380.
44. Xia, X., et al., *25th Anniversary Article: Galvanic Replacement: A Simple and Versatile Route to Hollow Nanostructures with Tunable and Well-Controlled Properties.* Advanced Materials, 2013. **25**(44): p. 6313-6333.
45. Sun, Y. and Y. Xia, *Shape-Controlled Synthesis of Gold and Silver Nanoparticles.* Science, 2002. **298**(5601): p. 2176-2179.
46. Yazdi, S., et al., *Reversible Shape and Plasmon Tuning in Hollow AgAu Nanorods.* Nano Letters, 2016. **16**(11): p. 6939-6945.
47. Genç, A., et al., *Tuning the Plasmonic Response up: Hollow Cuboid Metal Nanostructures.* ACS Photonics, 2016. **3**(5): p. 770-779.
48. Rodríguez-Fernández, J., et al., *Spatially-Directed Oxidation of Gold Nanoparticles by Au(III)–CTAB Complexes.* The Journal of Physical Chemistry B, 2005. **109**(30): p. 14257-14261.
49. Varón, M., J. Arbiol, and V.F. Puntes, *High Aspect Ratio Gold Nanorods Grown with Platinum Seeds.* The Journal of Physical Chemistry C, 2015. **119**(21): p. 11818-11825.
50. Bogart, L.K., et al., *Nanoparticles for Imaging, Sensing, and Therapeutic Intervention.* ACS Nano, 2014. **8**(4): p. 3107-3122.

Chapter 5

Hybrid Nanostructures

In this chapter, a facile one-pot approach for the production of heterodimer $AgCeO_2$, $Ag@CeO_2$ core-shell and hybrid $AuCeO_2$ NPs is presented. This novel and facile procedure is based on an assisted redox approach that involves the noble metal and the cerium precursors. In the case of $AgCeO_2$ nanostructures, the adjustment of synthetic conditions, such as pH, allows the formation of heterodimer or core-shell nanostructures.

5.1 Introduction

The design of new protocols for the production of complex hybrids NPs in order to expand their functionalities is an important field of research [1]. Atomic compositional and morphological control at the nanoscale allows the possibility of achieving new combinations of materials with enhanced or even new properties via the additive and synergic coupling between individual components [2]. Therefore, well defined hybrid metal-metal oxide NPs have attracted enormous attention because of their combined optic [3], magnetic [4], and catalytic properties [5], that cannot be obtained in monometallic NPs. The results from these studies show that the production of metal-metal oxide hybrid nanostructures should go beyond the simple combination of both materials in a single structure and involve control of the spatial distribution of each individual domain in both the structure and interface.

Despite recent advances in the production of hybrid NPs, a long-standing barrier has been the control of each component and the independent adjustment of the interface of these systems with enough precision. One of the main direct benefits of combining different NP functionalities is their use in improving both activity and selectivity in catalysis.

To date, a series of core@shell noble metal@oxides, such as $Au@TiO_2$ [6], $Au@SiO_2$ [7], $Pt@CeO_2$ [8], $Au@CeO_2$ [9], have been synthesized using templating strategies. In the metal/CeO_2 systems, the synergistic effect occurring at the interface can increase the performance (activity, selectivity and reusability) for a wide variety of reactions [10, 11]. Many of these synergic effects depend on the atomic interactions between the metal and the oxide

materials [12], which are influenced by their size and interfacial area. The first attempts to produce metal/CeO_2 nanocomposites involved the random mixing of large CeO_2 NPs and noble metal NPs, or the thermal treatment of oxide powders impregnated with a metal precursor [10]. There have been a number of recent improvements in the morphological and compositional control of metal/CeO_2 NPs using colloidal seeded growth strategies. These strategies have allowed the production of well-defined morphologies, including core@shell structures based on the growth of a CeO_2 shell onto a metallic core [13-16], one-step synthesis of noble metal@CeO_2 [17, 18], nanostructures and Au-CeO_2 Janus-like NPs [19]. However, the preparation of these NPs often requires multiple and complex steps, e.g. Kaneda and co-workers adopted a reverse micelle technique followed by calcination to produce Ag@CeO_2 [14, 15] and Au@CeO_2 [13] core-shell NPs with remarkable catalytic properties. Despite these developments, there have been no reports on the production of well-defined heterodimer $AgCeO_2$ NPs. As a result, a general, simple one pot aqueous approach between a Ag precursor and $Ce(NO_3)_3.6H_2O$ for the preparation of stable colloidal solutions of monodisperse heterodimer $AgCeO_2$ nanostructures, is herein presented. Furthermore, by slightly modifying reaction conditions, this approach can be used to obtain both Ag@CeO_2 core-shell nanostructures and $AuCeO_2$ hybrid NPs.

5.2 Materials and methods

5.2.1 Materials

Silver trifluoroacetate (CF_3COOAg), silver nitrate ($AgNO_3$), cerium(III) nitrate hexahydrate ($Ce(NO_3)_3$), sodium hydroxide (NaOH), gold (III) chloride trihydrate >99,9% ($HAuCl_4 . 3H_2O$) and sodium citrate tribasic dihydrate (SC), were purchased from Sigma-Aldrich. All chemicals were used as received without further purification. Distilled water passed through a Millipore system (ρ = 18.2 mΩ) was used in all experiments.

5.2.2 Methods

5.2.2.1 Synthesis of heterodimer $AgCeO_2$ NPs. In a typical procedure, 500 mL of MQW were added into a 1L three necked round bottom flask, 1.47 g of SC was added. The solution was heated until 100˚C under magnetic stirring. Prior to boiling, 5 mL of $AgNO_3$ 25 mM and 5 mL of $Ce(NO_3)_3$ 25 mM were sequentially injected to the solution, and it was heated at 100˚C

for 4 hours. After heating, the solution had an orange colour and a UV-Vis spectrum was acquired.

5.2.2.2 Synthesis of core-shell Ag@CeO_2 NPs. In a typical procedure, 500 mL of MQW were added to a 1L three necked round bottom flask, 1.47 g of SC was added. The pH of the solution was adjusted to pH 10 with the addition of a few drops of a NaOH solution. The solution was heated until 100˚C under magnetic stirring. Prior to boiling, 5 mL of $AgNO_3$ 25 mM and 5 mL of $Ce(NO_3)_3$ 25 mM were sequentially injected to the solution, and it was heated at 100˚C for 4 hours After heating, the solution had an orange colour and a UV-Vis spectrum was acquired.

5.2.2.3 Synthesis of hybrid AuCeO_2 NPs. In a typical procedure, 500 mL of MQW were added into a 1L three necked round bottom flask, 1.47 g of SC was added. The solution was heated until 100˚C under magnetic stirring. Prior to boiling, 5 mL of $HAucl_4$ 25 mM and 5 mL of $Ce(NO_3)_3$ 25 mM were sequentially injected to the solution, and it was heated at 100˚C for 4 hours. After heating the solution had a reddish colour and a UV-Vis spectrum was acquired.

5.2.2.4 Characterization. Absorption spectra of the as synthesized NPs were acquired with a Shimadzu UV-2401 PC spectrophotometer. The morphology, size and chemical composition of the NPs were visualized using FEI Magellan 400L XHR SEM, in transmission mode operated at 20 kV. TEM, HR-TEM, and STEM/ HAADF images were obtained with a FEI Tecnai G2 F20 S-TWIN HR(S) TEM, operated at an accelerated voltage of 200 kV. A droplet of the sample was drop cast onto a piece of ultrathin carbon-coated 200-mesh copper grid (Ted-pella, Inc.) and left to dry in air XRD data were collected on a PANalytical X'Pert diffractometer using a Cu Kα radiation source.

5.3 Results

5.3.1 Synthesis of heterodimer AgCeO_2 NPs. Colloidal solutions of heterodimer $AgCeO_2$ NPs were obtained by the reaction of $AgNO_3$ with $Ce(NO_3)_3$ at equimolar concentrations, in a refluxing aqueous solution of SC (10 mM) (see section 5.2.2.1 for experimental details). After the injection of the Ag and Ce precursors into the SC solution, the solution turned from transparent to yellow, and then after 1 hour to orange (See **Figure 5.1B**), indicative of the formation of heterodimer $AgCeO_2$ NPs. The reaction was continued for 4 hours until no further changes in the UV-Vis spectra were observed (**Figure 5.3**). UV-vis

spectrum of the as synthesized heterodimer $AgCeO_2$ NPs is presented in **Figure 5.1A** (black line). As can be observed, the heterodimer particles exhibit two intense absorption bands around 250 nm (see **Figure 5.3B**) and 412 nm corresponding to the CeO_2 and SPR of the Ag NPs respectively. It has been reported [20] that 19 nm citrate stabilized Ag NPs show a SPR band near 404 nm (**Figure 5.1B** red line). The difference in the SPR band between these citrate stabilized NPs and the heterodimer $AgCeO_2$ NPs in this study can be explained by the interaction between the plasmonic Ag and the small CeO_2 domains. Such a redshift has been observed previously in core@shell NPs [21]. The simultaneous addition of the cerium precursor had an effect on the final morphology of the Ag NPs, since, without the addition of $Ce(NO_3)_3$ the resulting Ag NPs synthesized in SC 10 mM were formed by anisotropic nanostructures as depicted in **Figure 5.1C.** The colour of the solution was also different as is shown in the inset of **Figure 5.1C**. As expected, this UV-Vis spectrum was quite different to the one obtained for the heterodimer NPs with a SPR band at 407 nm (**Figure 5.1A**, blue line).

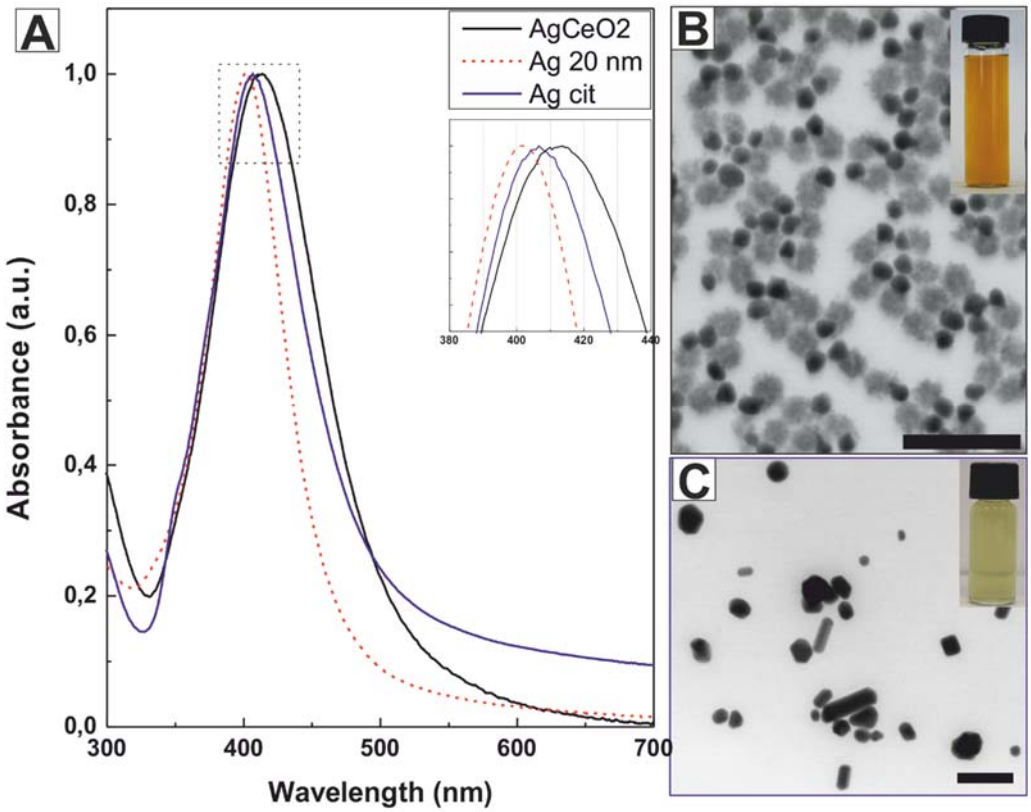

Figure 5.1 A. UV–Vis spectra of $AgCeO_2$ NPs (black line), Ag 20 nm NPs (red line) and Ag synthesized in SC 10 mM (blue line) **B**. TEM image of $AgCeO_2$ NPs. **C.** TEM image of Ag NPs synthesized in SC 10 mM. Insets show a photographs of the corresponding colloidal solution. Scale bar represent 100 nm for all images.

TEM (**Figure 5.2A**) and HAADF-STEM (**Figure 5.2B**) images of $AgCeO_2$ NPs, reveal the formation of highly monodisperse heterodimer hybrid nanostructures composed of two pseudo-spherical domains with average diameters of 19.1 ± 3.1 nm for the Ag domain (**Figure 5.2C**) and 24.7 ± 3.6 nm for the CeO_2 domain (**Figure 5.2D**). In the HAADF-STEM images (**Figure 5.2B**), the Ag NPs with brighter contrast can be clearly distinguished from CeO_2 NPs with grey contrast.

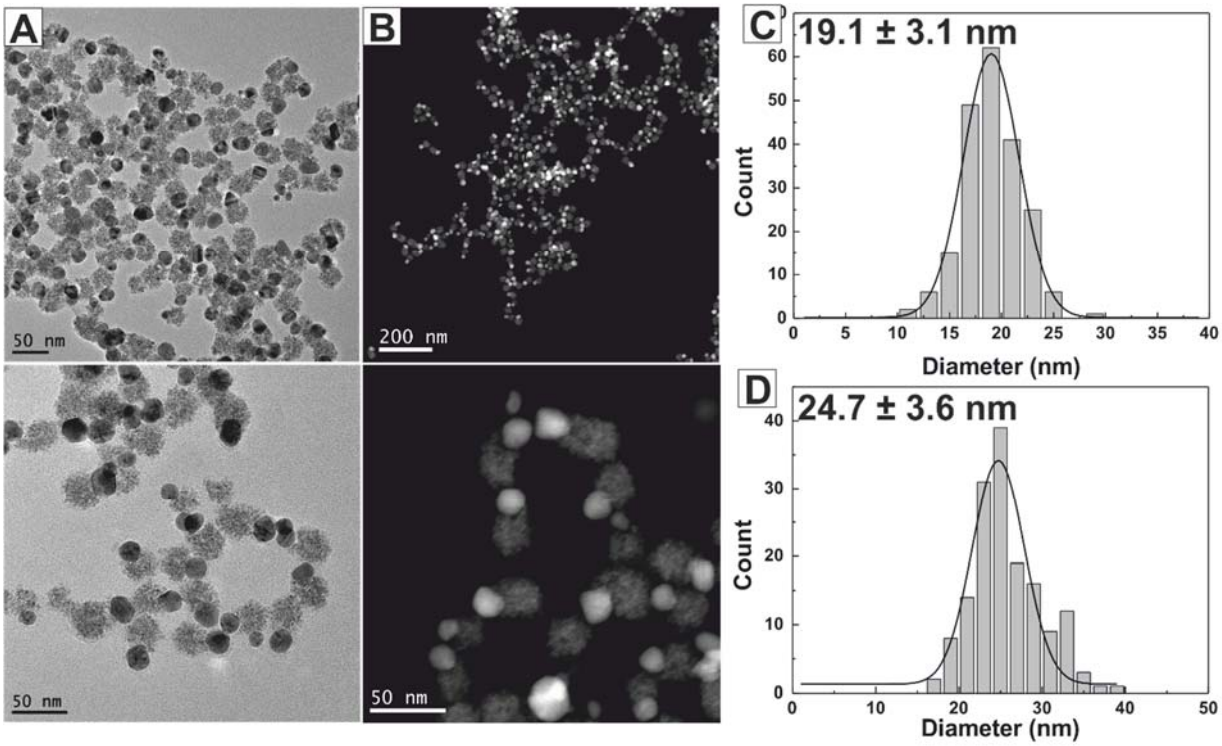

Figure 5.2 A. TEM images and **B**. HAADF-STEM of heterodimer $AgCeO_2$ NPs. **C.** Size distribution of Ag domain. **D.** Size distribution of CeO_2 domain.

The growth of the heterodimer nanostructures is reflected in the SPR absorption band obtained by UV-Vis (**Figure 5.3B**). **Figure 5.3A** shows a photograph of aliquots of the reaction of heterodimer $AgCeO_2$ taken at different reaction times. At shorter times (30 min) poorly defined $AgCeO_2$ NPs are shown by TEM image, which correlate with the appearance of a broad band at 403 nm, characteristic of small Ag NPs [20]. In **Figure 5.3C**, CeO_2 NPs can also be observed. At longer times, the SPR absorption band at 403 nm increases and presents a small redshift until 410 nm, as well as the number of heterodimer NPs also rises, the absorption band in the near UV region increases which is indicative of the formation of CeO_2 species.

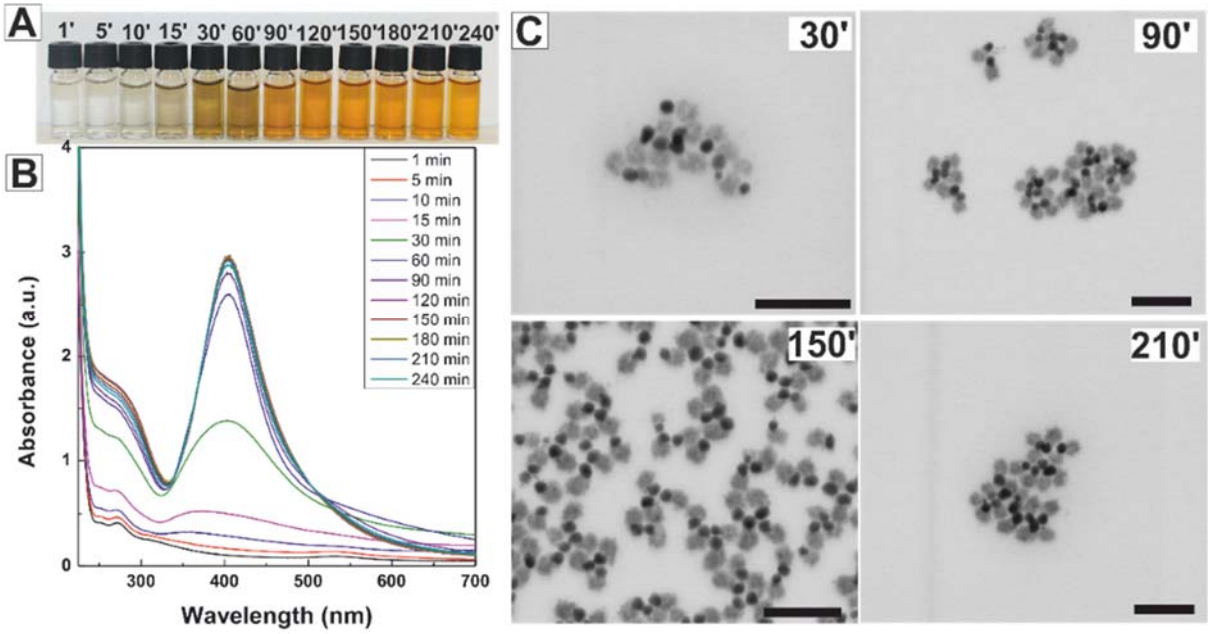

Figure 5.3 A. Photographs of the vials at different times of reaction. **B.** UV-vis spectra of heterodimer $AgCeO_2$ NPs growth **C.** TEM images of heterodimer $AgCeO_2$ NPs at different time of reaction. Scale bars represent 100 nm for all images.

Figure. 5.4A shows a HR-TEM image obtained from an individual heterodimer $AgCeO_2$ NP. The Ag domain consists of a multi-twinned NP and the CeO_2 part consists of multiple nanocrystallites having sizes about ~3 nm. Detail of the red squared region (**Figure 5.4B)** reveals the presence of multiple crystallites merged together. The corresponding power spectrum of the region (**Figure 5.4C**) shows that these nanocrystallites are composed of a face centred cubic CeO_2 phase with a lattice parameter of a= 0.5412 nm. Multifaceted Ag NPs were found to be composed of face centred cubic Ag phases with a lattice parameter of a= 0.4085 nm. As shown in the inset in **Figure 5.4A** (green square), the orientation of the Ag NP allows us to visualize only the {111} plane of the f.c.c. Ag phase.

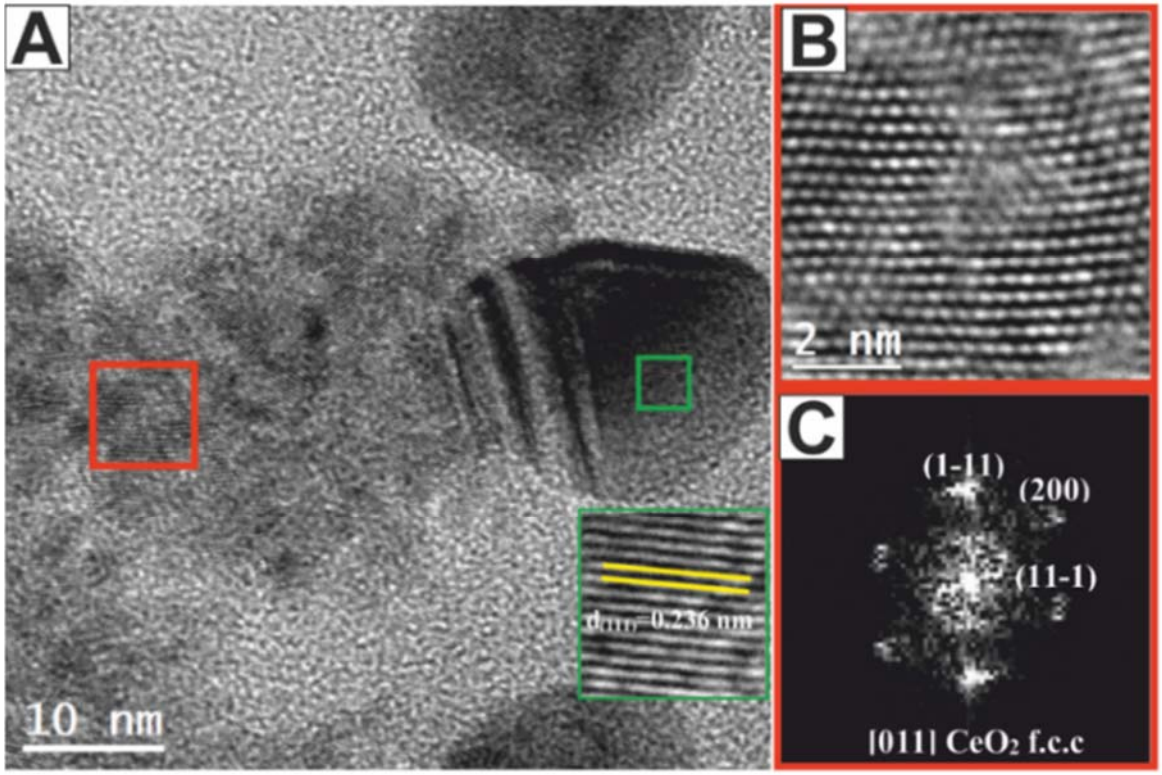

Figure 5.4 A. HRTEM image of a heterodimer $AgCeO_2$ NP. Inset shows the detail of the green squared region. **B.** Detail of the red squared region and **C.** its corresponding power spectrum.

Figure 5.5A shows a HR-TEM image of two heterodimer $AgCeO_2$ NPs. The interface of both domains is highlighted in the yellow square (**Figure 5.5B**). Its corresponding power spectrum (FFT) is presented in **Figure 5.5C** in which the diffraction spots corresponding to the {111} planes of f.c.c. CeO_2 phase (d = 0.312 nm) are marked with red circles and the diffraction spots corresponding to the {111} planes of f.c.c. Ag phases (d = 0.236 nm) are marked with green circles. **Figure 5.5D** shows a false coloured inverse FFT, revealing the quasi-epitaxial relationship between the Ag and CeO_2 NPs. As marked with grey parentheses, Ag {111} planes are aligned with the CeO_2 {111} planes. In addition, and due to the different lattice parameter, there are four Ag {111} planes for each three CeO_2 {111} planes (lattice mismatch of 24%).

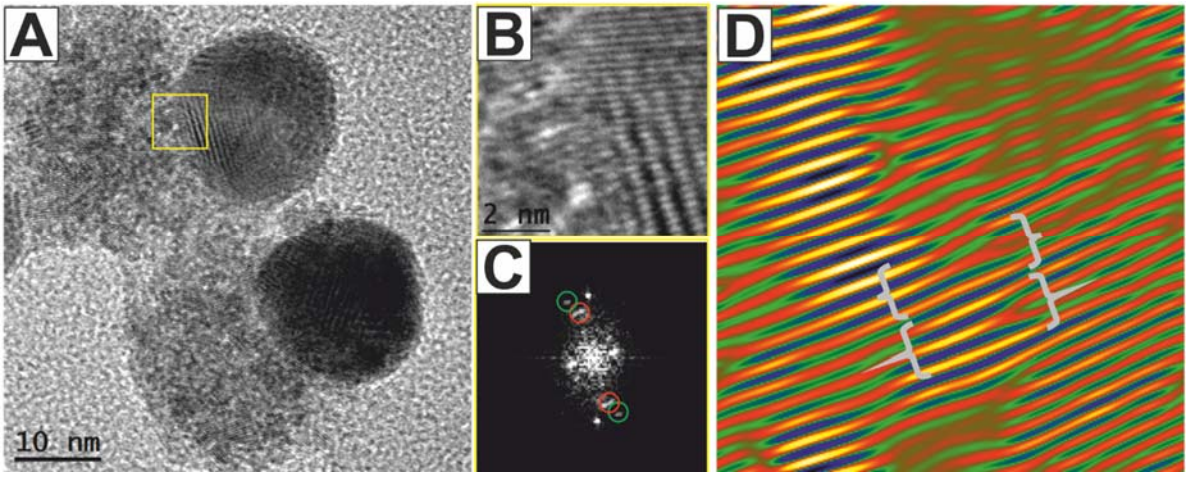

Figure 5.5 A. HRTEM image of heterodimer $AgCeO_2$ NPs. **B.** Detail of the yellow squared region **C.** its corresponding power spectrum (FFT) **D.** Inverse FFT showing the epitaxy between Ag and CeO_2 NPs.

The elemental chemical composition, obtained by EELS (**Figure 5.6A**), of a single heterodimer $AgCeO_2$ NP, clearly demonstrates that the heterodimers are composed of pure Ag and CeO_2 phases. Elemental maps of individual Ag (blue), Ce (red), O (green) and composite are shown in **Figure 5.6B**.

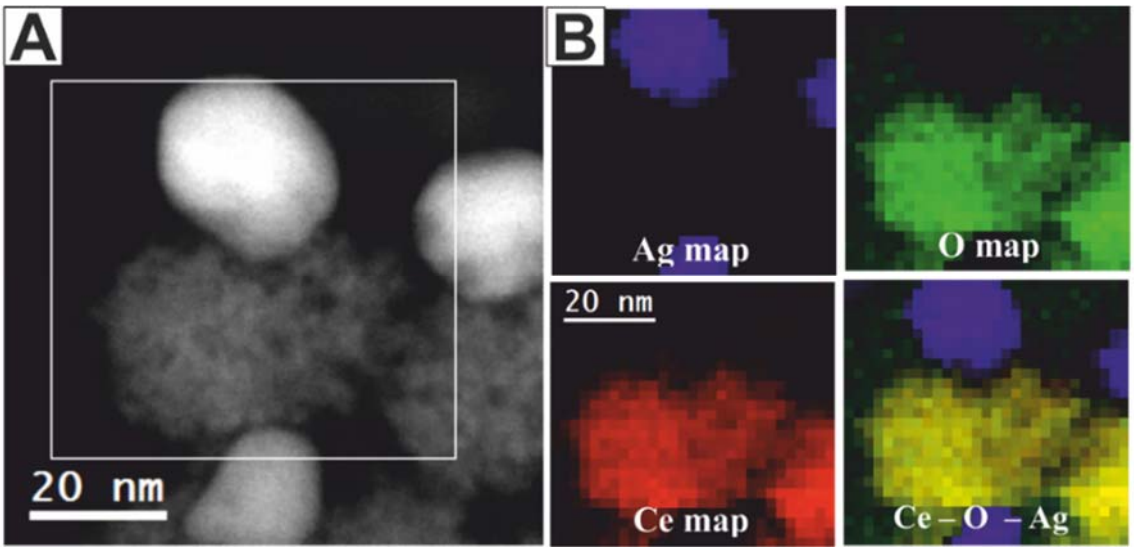

Figure 5.6 A. HAADF-STEM image of heterodimer $AgCeO_2$ NPs. **B.** EELS chemical composition maps obtained from the area indicated in the white rectangle in **A**. Ce (red), O (green) and Ag (blue) maps and their composite. The scale bar is the same for all composition maps.

The crystal structure of the heterodimer $AgCeO_2$ NPs was also investigated by XRD, shown in **Figure 5.7.** Two series of peaks can be seen in the diffraction pattern, which are clearly associated with the cubic fluorite CeO_2 phase (JCPDS 34-0394) (**Figure 5.7**, blue line) and the fcc structure of Ag (JCPDS file No. 04-0783) (**Figure 5.7**, red line). The peak positions are attributed to Ag (111), (200), (220), (311) and (222) planes of a face-centred cubic structure and CeO_2 (111), (200), (220), (311) planes of fluorite structure. The lattice parameters, *a*, 5.510 Å for CeO_2 and 4.101 Å for Ag , were found to be slightly higher than the reference values of CeO_2 (5.411 Å [22]) and Ag (4.079 Å [23]), indicating an interaction between both domains. The crystallite size of CeO_2 calculated by the Scherrer equation corresponds to 5.83 nm which agrees with the size measured from TEM images. No peaks corresponding to other Ag-containing or Ce-containing phases were detected in the XRD patterns of the as-synthesized heterodimer.

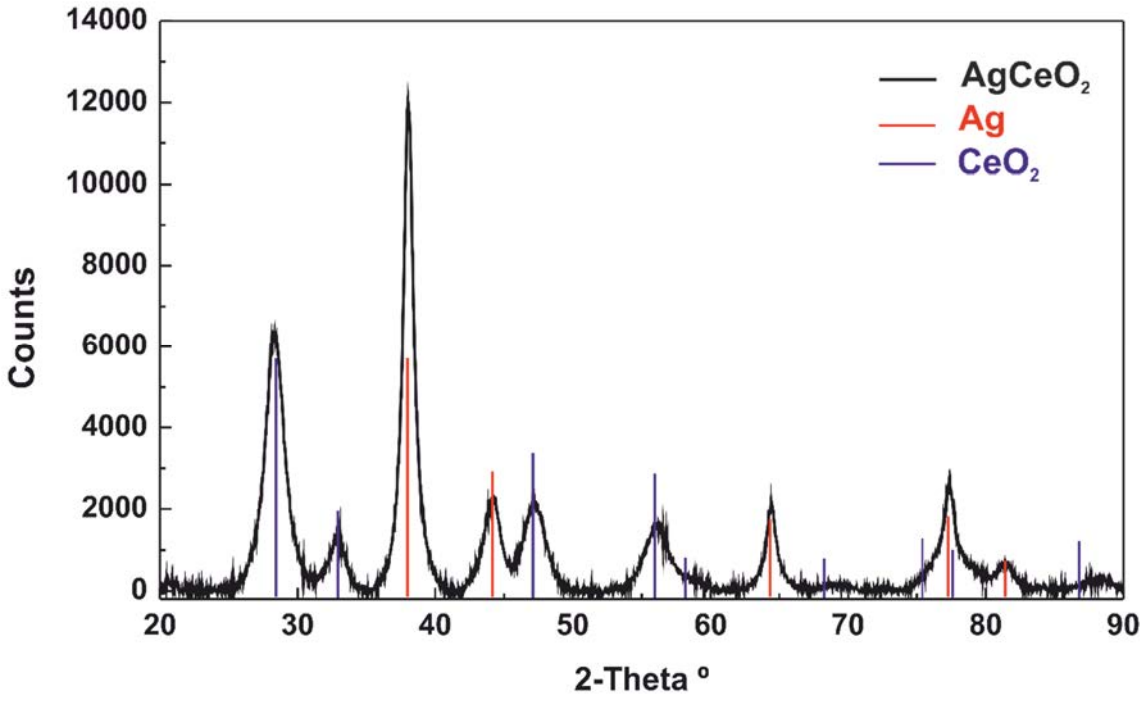

Figure 5.7 XRD diffraction pattern of heterodimer $AgCeO_2$ NPs (black line), Ag (red line) and CeO_2 (blue line).

In order to evaluate the reproducibility of the method, five independent synthesis were performed. Results shown in **Figure 5.8** suggest an excellent reproducibility of the synthetic methodology presented because the heterodimer morphology of the resulting $AgCeO_2$ nanostructures is the same for all the synthesis. Furthermore, the LSPR band positions

due to the Ag domain absorption of all synthesis are the same and correspond to 409 nm. In the same way, the absorption due to the CeO_2 domain appears around 250 nm.

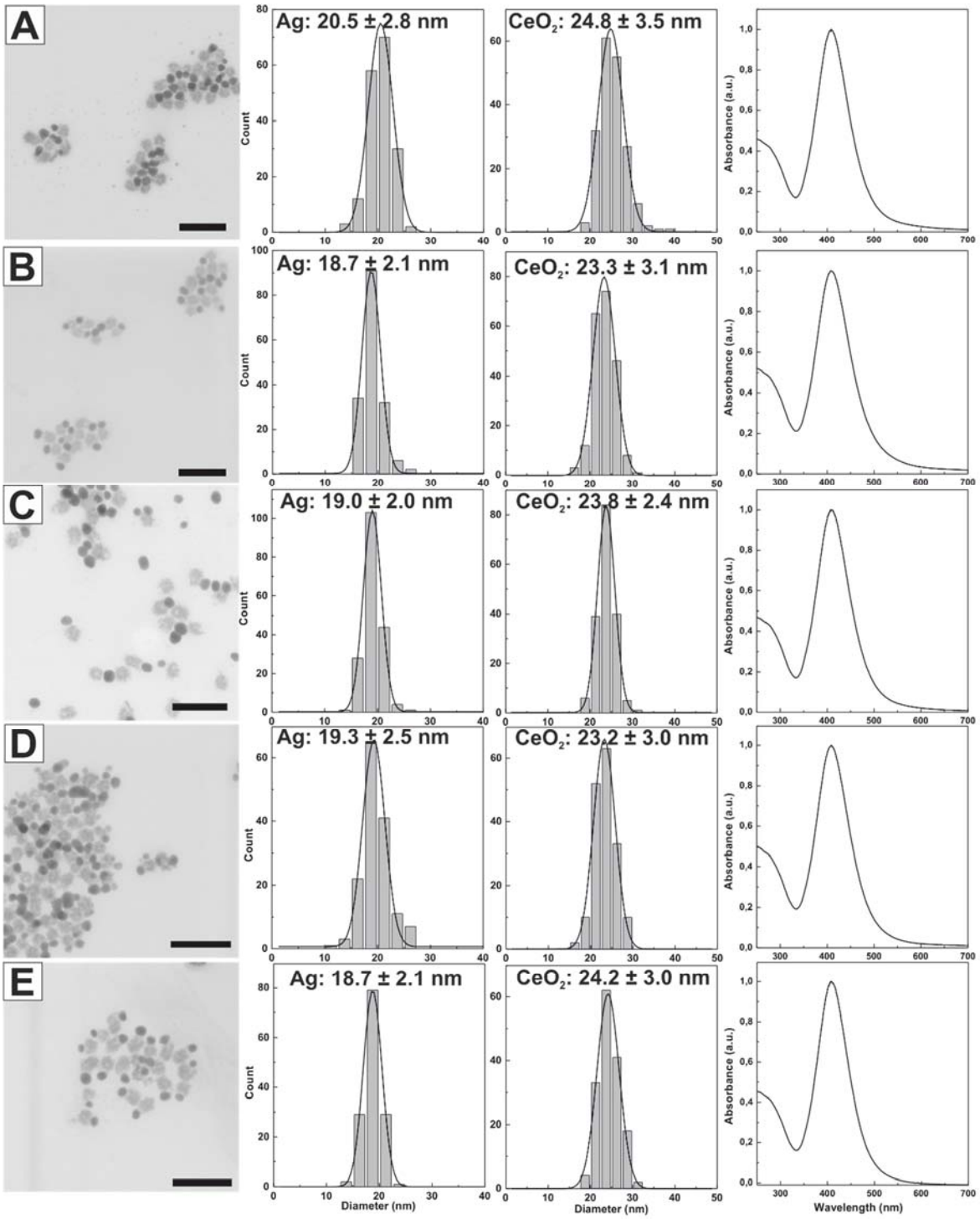

Figure 5.8 TEM images, Ag domain size distribution, CeO_2 domain size distribution and UV-Vis spectra of 5 (**A-E**) synthesis of heterodimer $AgCeO_2$ nanostructures. Scale bars represent 100 nm for all images.

The following results clearly demonstrate that the adjustment of synthetic parameters allow the control of the final morphology of the hybrid nanostructures.

5.3.1.1 Effect of Ag precursor. In the first instance, the effect of the Ag precursor in the reaction was studied. Remarkably, when CF_3COOAg was used instead of $AgNO_3$, with all the other reaction parameters kept constant, no significant differences were observed and heterodimer $AgCeO_2$ NPs with the same morphology were obtained, as can be observed in **Figure 5.9A-B**. Analysis of TEM (**Figure 5.9A**) and HAADF-TEM (**Figure 5.9B**) images of the heterodimer $AgCeO_2$ synthesized using CF_3COOAg, shows that the size of the Ag domain is slightly smaller (15.2 ± 3.8 nm) than in the case of $AgNO_3$ (19.1 ± 3.1 nm). This can be corroborated with the SPR band of heterodimer $AgCeO_2$ NPs synthesized with CF_3COOAg which has a strong absorption band at 405 nm (**Figure 5.9C**) corresponding to a smaller size of the Ag domain, this value its slightly higher than 15 nm Ag NPs (401 nm) [20], due to the interaction between the Ag and CeO_2 domains.

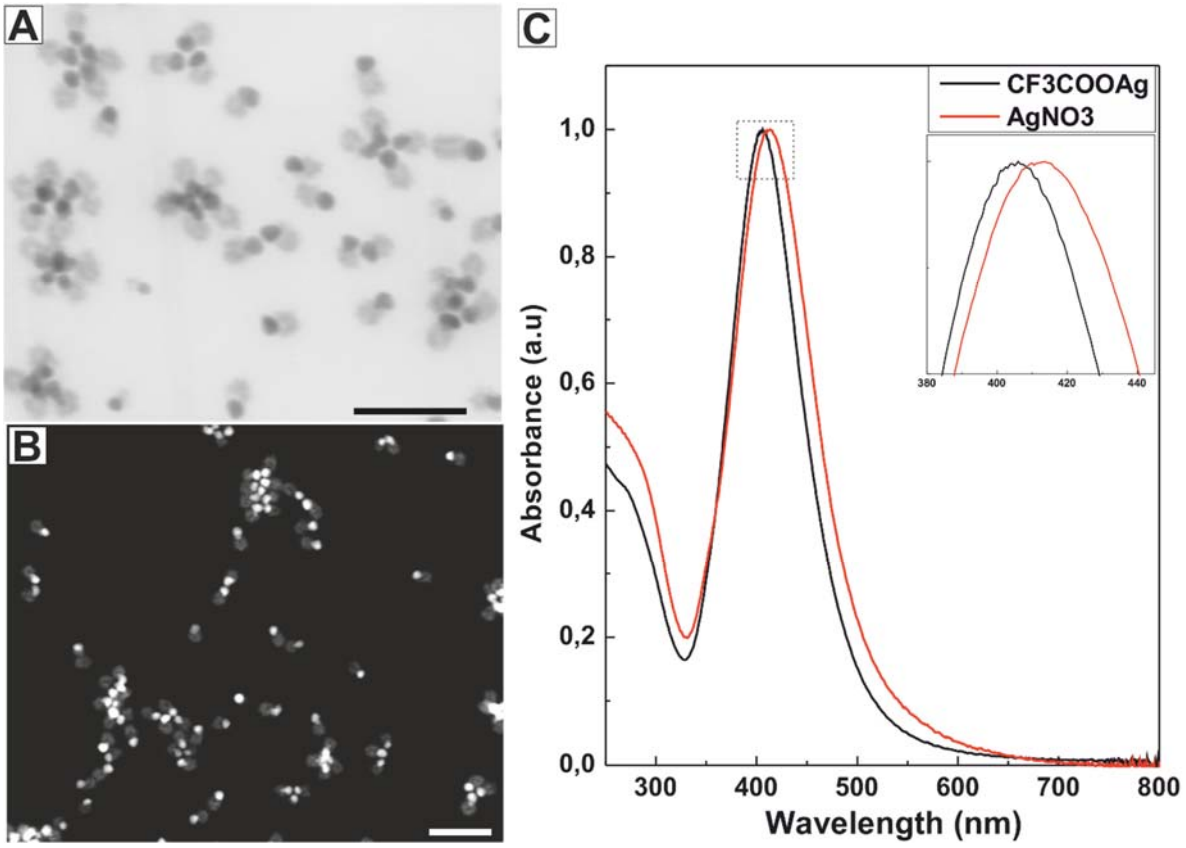

Figure 5.9 A. TEM and **B.** HAADF-TEM images of heterodimer $AgCeO_2$ NPs synthesized with CF_3COOAg as Ag precursor. **C.** UV-Vis spectra of heterodimer $AgCeO_2$ NPs synthesized with CF_3COOAg (black line) and $AgNO_3$ (red line) as Ag precursor. Scale bars represent 100 nm.

5.3.2 Synthesis of core-shell Ag@CeO_2 NPs. It is well established that reaction pH defines the reactivity of the noble metal precursor and the protonation state of the citrate ions, finally determining the reaction mechanism, and therefore the final NPs morphology [20, 24, 25]**.** At different pH, the reactivity of Ag^+ and Ce^{3+} precursors changes. When the reaction was carried out at an initial pH 10 adjusted with NaOH, the colour of the reaction changed from yellow to brown in less than one minute. Finally, after 4 hours of reaction, the final colour of the solution was orange as is shown in the inset of **Figure 5.10B**. The morphology of the resulting NPs, corresponded to a mixture between core@shell Ag@CeO_2 nanostructure, heterodimer AgCeO_2 NPs, polydisperse Ag NPs and CeO_2 nanosponge-like structures, as displayed in **Figure 5.10B**. At this pH, the reactivity of the Ce^{3+} precursor increased allowing the formation of core@shell nanostructures, while the reactivity of Ag^+ decreased and the size of the resulting core was smaller than in the case of the heterodimer nanostructures. The abundance of core-shell Ag@CeO_2 NPs was 46% with an overall diameter of 19.3 ± 2.1 nm, where the core was formed by Ag NPs with an average size of 8.5 ± 1.2 nm, and the shell corresponded to the CeO_2 domain with a thickness of ~5nm. The remaining 54% corresponded to a mixture of heterodimer AgCeO_2 NPs (30 %), CeO_2 NPs (18%), and Ag NPs (6%). UV-Vis spectra (**Figure 5.10A,** red line) show a peak at 406 nm which was redshifted in comparison with Ag NPs of similar sized (397 nm for 10 nm Ag NPs [20]) due to the interaction between the core and shell domains. When the reaction was done at an initial pH of 5 adjusted with HNO_3, the reaction proceeded very slowly, and only after 15 minutes the colour of the reaction started to change to pale yellow. The inset photograph in **Figure 5.10C** shows that after 4 hours of reaction the final colour of the solution remained yellow. TEM image in **Figure 5.10C** shows that no hybrid structures were obtained when the initial pH was 5 and only Ag NPs with an average size of 20.6 ± 3.8 nm were formed. The UV-vis- spectra (**Figure 5.10A**) show a sharp absorption band at 403 nm which corresponds to reported values for Ag NPs of this size [20]. Therefore, at acidic pH values the cerium precursor cannot be oxidized to form CeO_2 NPs.

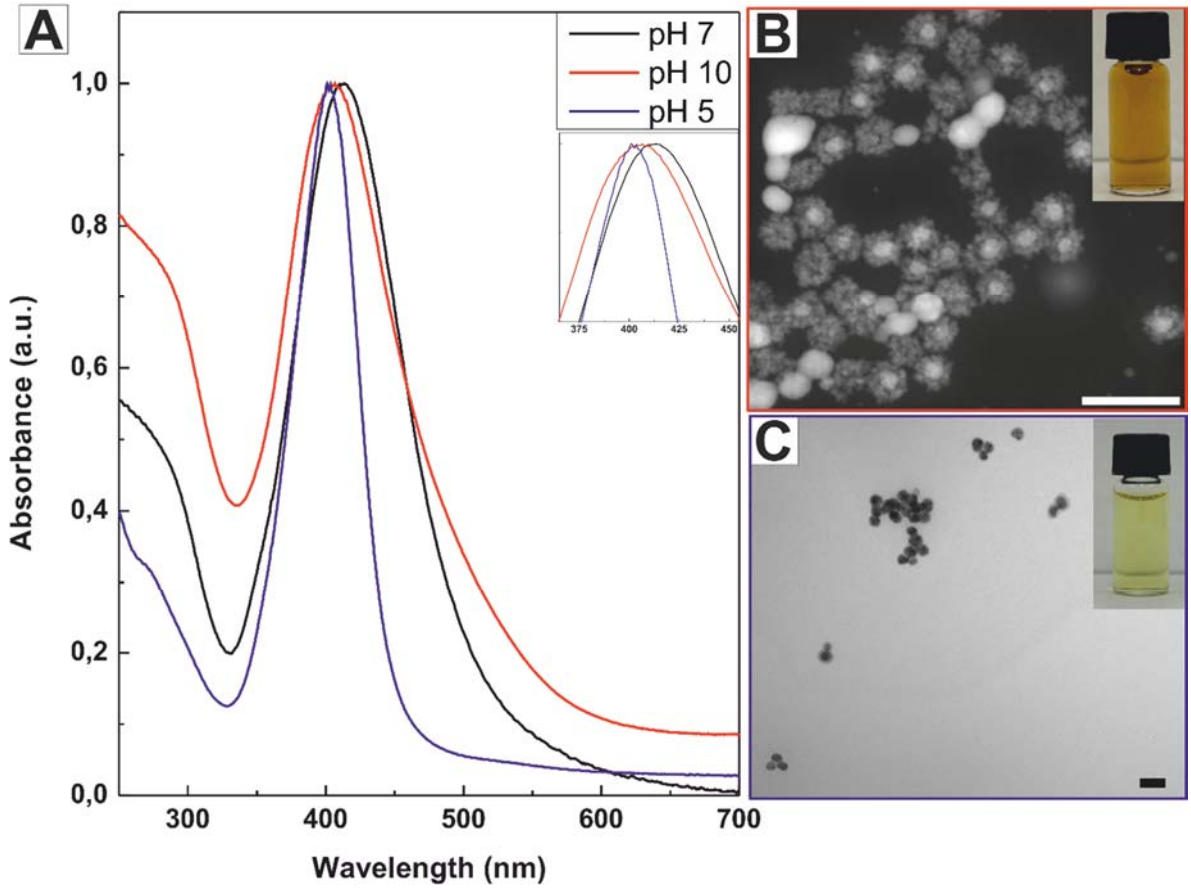

Figure 5.10 A. UV-Vis spectra of hybrid $AgCeO_2$ NPs synthesized at pH 7 (black line), pH 10 (red line) and pH 5 (blue line). **B.** HAADF-STEM image of $Ag@CeO_2$ NPs synthesized at pH 10. **C.** TEM image of $AgCeO_2$ NPs synthesized at pH 5. Scale bars represent 50 nm for all images.

The elemental chemical composition, obtained by EELS (**Figure 5.10**), of a single $Ag@CeO_2$ core-shell NPs, clearly demonstrate that the nanostructure is composed of an Ag core and a CeO_2 shell. Elemental maps of individual Ag (blue), Ce (red), O (green) are shown in **Figure 5.11**.

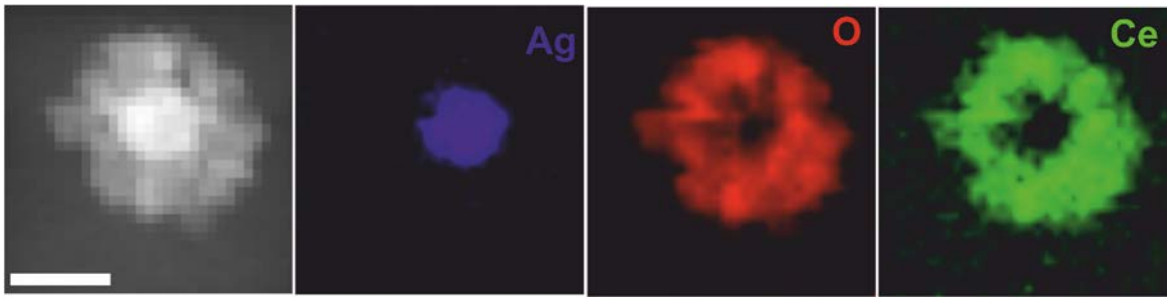

Figure 5.11. HAADF-STEM image of a core-shell $Ag@CeO_2$ NP. EELS chemical composition maps. Ag in blue, O in red and Ce in green. The scale bar is the same for all the images.

5.3.3 Synthesis of hybrid $AuCeO_2$ NPs. Following the same procedure described for the production of heterodimer $AgCeO_2$ in section 5.2.2.1, but using $HAuCl_4$ as a metal precursor, colloidal solutions of monodisperse hybrid $AuCeO_2$ nanostructures were obtained. **Figure 5.12A-B** present a HAADF-STEM and TEM images of as synthesized NPs and reveal the formation of hybrid nanostructures. The contrast difference in the microscope images clearly show that the particles are formed by a gold core, surrounded by CeO_2 crystallites. After the injection of the Au^{+3} precursor, the solution turned instantaneously from transparent to dark, and after a few hours to dark red as shown in **Figure 5.12C**. By means of the size distribution analysis shown in **Figure 5.12D**, the average diameter of the hybrid $AuCeO_2$ nanostructures was 9.4 ± 2.0 nm, whereas the average diameter of the Au core was 4.4 ± 1.2 nm and 2.8 ± 0.7 nm for the CeO_2 crystallites.

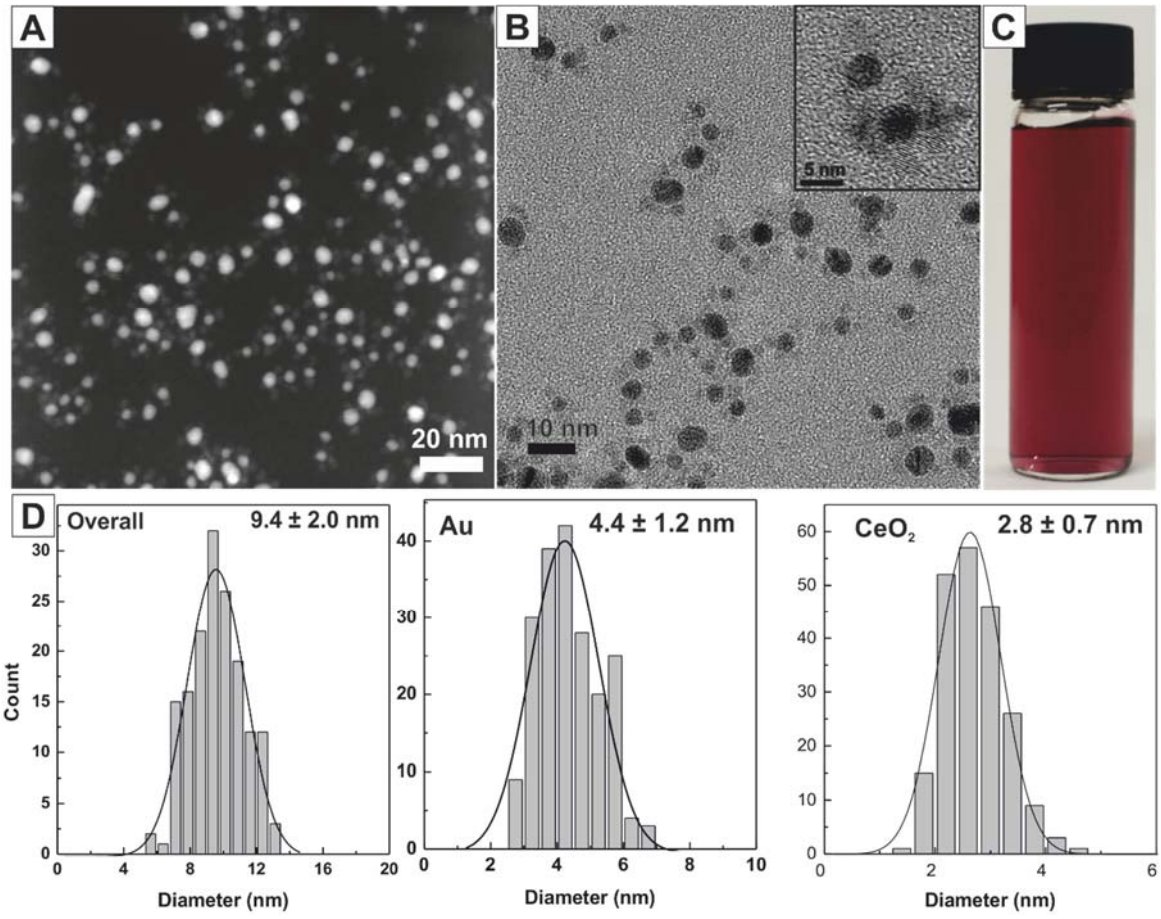

Figure 5.12. A. STEM-HAADF, **B.** TEM images and. **C.** Photograph of aqueous dispersion of hybrid $AuCeO_2$ NPs. **D.** Size distribution of overall hybrid NPs, Au core and CeO_2 crystallites.

As also seen in the HRTEM image (**Figure 5.13**), this sample consists of CeO_2 crystallites around a ~5 nm Au core NP forming a core@shell nanostructure. On the right, detail of the red squared region and its corresponding power spectrum, which reveals that the shell nanocrystallite have f.c.c. CeO_2 phase as the $AgCeO_2$ sample showed in **Figure 5.4**.

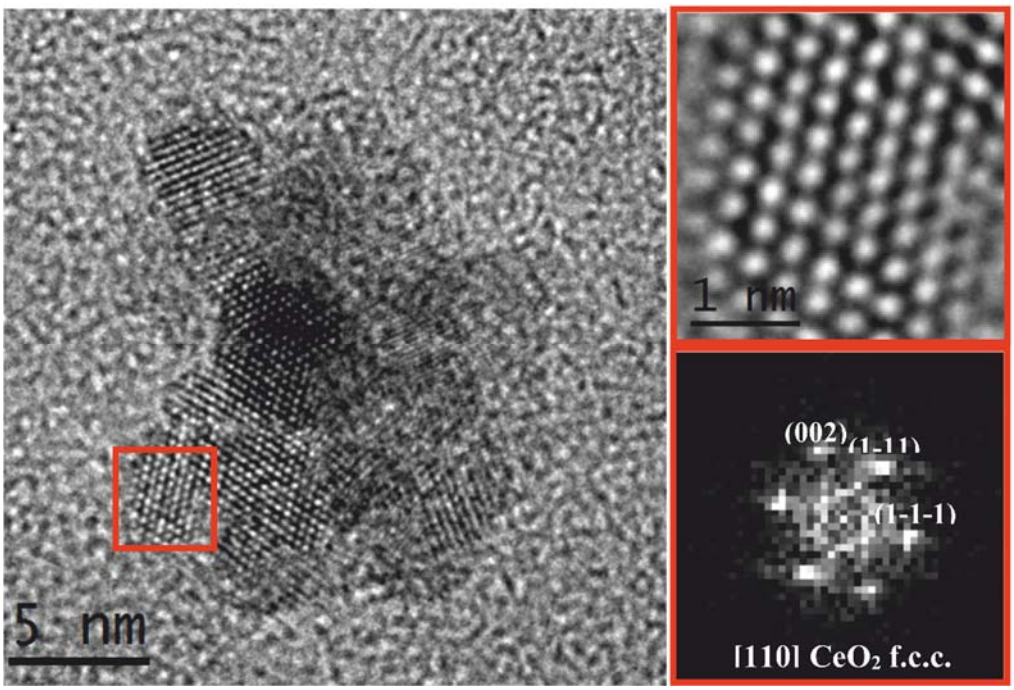

Figure 5.13 : HRTEM image showing the polycrystalline shell around the Au core. On the right, detail of the red squared region and its corresponding power spectrum revealing that the shell is composed of the f.c.c. CeO_2 phase, are presented.

Evidence of the hybrid structure can be seen in the absorption UV-Vis spectra displayed in **Figure 5.14A.** In this image, the peak around 270 nm corresponds to CeO_2 nanostructures while the SPR band at 525 nm can be assigned to the Au NPs. The 5 nm Au NPs present a SPR band at 510 nm [26] and the redshift obtained in the case of the hybrid $AuCeO_2$ NPs was caused by the interaction between the CeO_2 and the Au. The crystal structure of the hybrid $AuCeO_2$ nanostructure was further investigated by X-ray diffraction. As shown in **Figure 5.14B,** two series of peaks were present in the diffreaction pattern, which could be clearly assigned to the cubic fluorite CeO_2 phase and the to the cubic Au phase. The XRD analysis of hybrid $AuCeO_2$ NPs, showed peak positions attributed to Au (111), (200), (222), (311) and (212) planes of a face-cantered cubic structure and CeO_2 (111), (200), (220), (311) planes of fluorite structure.

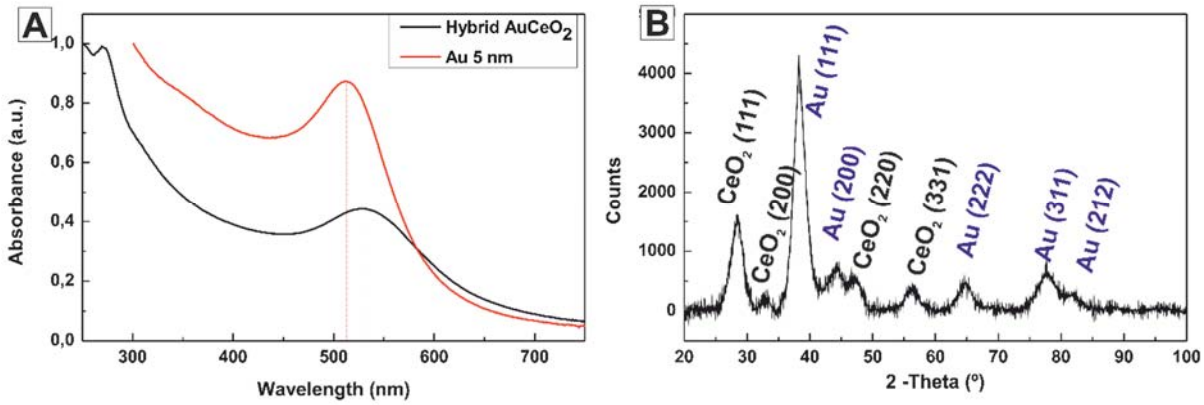

Figure 5.14 A. UV-Vis spectra of hybrid $AuCeO_2$ NPs in black, and 5 nm Au NPs in red. **B.** XRD pattern of hybrid $AuCeO_2$ NPs.

Figure 5.15 shows EELS chemical composition maps of Ce (green), O (red) and Au (blue) maps from the $Au@CeO_2$ nanostructures in the STEM-HAADF image. As seen in these maps, the nanostructure is composed of an Au core and a CeO_2 shell. The Ce and O are distributed quite homogeneously throughout the NPs.

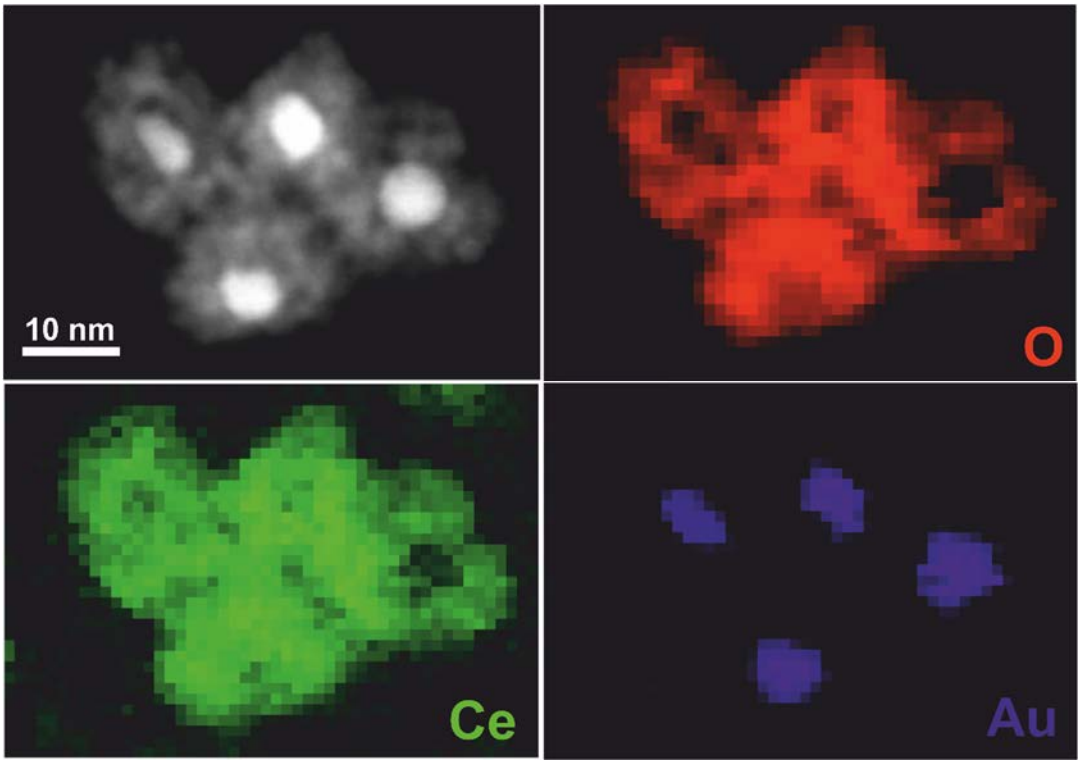

Figure 5.15 HAADF-STEM image of core-shell $Au@CeO_2$ NPs. EELS chemical composition maps. O in red, Au in blue and Ce in green. The scale bar is the same for all the images.

5.3.4. Insights into the formation mechanism. The overall formation mechanism can be described in terms of: i) the initial reduction of the metal precursor ions by the presence of SC, Ce^{3+} or the combination of both, followed by ii) the slow oxidation and hydrolysis of Ce^{3+} ions catalysed at the surface of the metal NP. In these processes SC plays multiple roles. First, SC provides the conditions by which nucleation and growth of noble metal NPs is favoured, acting as a reducer and stabilizer. Second, SC acts as a pH buffer, keeping the solution slightly alkaline (pH>7), promoting the conditions by which the Ce^{3+} is oxidized by O_2 or noble metal cation. This was proved by performing the reaction at acidic pH where only the formation of Ag NPs was observed. Third, SC allows adjusting the reactivity of a Ce precursor towards stable species, preventing the formation of isolated CeO_2 NPs. In these conditions, SC acts as a directing agent for assisting the CeO_2 growth provided that the hydrolysis of Ce^{+4} requires the presence of the noble metal surface to be catalysed [27].

5.4 References

1. Bastús Neus, G., et al., *Exploring New Synthetic Strategies for the Production of Advanced Complex Inorganic Nanocrystals*, in *Zeitschrift für Physikalische Chemie*. 2015. p. 65.
2. Cozzoli, P.D., T. Pellegrino, and L. Manna, *Synthesis, properties and perspectives of hybrid nanocrystal structures.* Chemical Society Reviews, 2006. **35**(11): p. 1195-1208.
3. Sobal, N.S., et al., *Synthesis and Structure of Colloidal Bimetallic Nanocrystals: The Non-Alloying System Ag/Co.* Nano Letters, 2002. **2**(6): p. 621-624.
4. Sun, S., *Recent Advances in Chemical Synthesis, Self-Assembly, and Applications of FePt Nanoparticles.* Advanced Materials, 2006. **18**(4): p. 393-403.
5. Enache, D.I., et al., *Solvent-Free Oxidation of Primary Alcohols to Aldehydes Using Au-Pd/TiO₂ Catalysts.* Science, 2006. **311**(5759): p. 362-365.
6. Du, J., et al., *Facile synthesis of Au@TiO2 core-shell hollow spheres for dye-sensitized solar cells with remarkably improved efficiency.* Energy & Environmental Science, 2012. **5**(5): p. 6914-6918.
7. Jeong, U., J.B. Joo, and Y. Kim, *Au nanoparticle-embedded SiO2-Au@SiO2 catalysts with improved catalytic activity, enhanced stability to metal sintering and excellent recyclability.* RSC Advances, 2015. **5**(69): p. 55608-55618.
8. Wang, X., et al., *Pt@CeO2 Multicore@Shell Self-Assembled Nanospheres: Clean Synthesis, Structure Optimization, and Catalytic Applications.* Journal of the American Chemical Society, 2013. **135**(42): p. 15864-15872.
9. Qi, J., et al., *Facile synthesis of core-shell Au@CeO2 nanocomposites with remarkably enhanced catalytic activity for CO oxidation.* Energy & Environmental Science, 2012. **5**(10): p. 8937-8941.
10. Huang, P.X., et al., *CeO2 Nanorods and Gold Nanocrystals Supported on CeO2 Nanorods as Catalyst.* The Journal of Physical Chemistry B, 2005. **109**(41): p. 19169-19174.
11. Carrettin, S., et al., *Nanocrystalline CeO2 Increases the Activity of Au for CO Oxidation by Two Orders of Magnitude.* Angewandte Chemie International Edition, 2004. **43**(19): p. 2538-2540.

12. Cargnello, M., et al., *Control of Metal Nanocrystal Size Reveals Metal-Support Interface Role for Ceria Catalysts.* Science, 2013. **341**(6147): p. 771-773.
13. Mitsudome, T., et al., *One-step Synthesis of Core-Gold/Shell-Ceria Nanomaterial and Its Catalysis for Highly Selective Semihydrogenation of Alkynes.* Journal of the American Chemical Society, 2015. **137**(42): p. 13452-13455.
14. Mitsudome, T., et al., *Design of a Silver–Cerium Dioxide Core–Shell Nanocomposite Catalyst for Chemoselective Reduction Reactions.* Angewandte Chemie International Edition, 2012. **51**(1): p. 136-139.
15. Mitsudome, T., et al., *Core–Shell AgNP@CeO2 Nanocomposite Catalyst for Highly Chemoselective Reductions of Unsaturated Aldehydes.* Chemistry – A European Journal, 2013. **19**(17): p. 5255-5258.
16. Shi, Y., et al., *Core-shell structured nanocomposites Ag@CeO2 as catalysts for hydrogenation of 4-nitrophenol and 2-nitroaniline.* Rsc Advances, 2016. **6**(53): p. 47966-47973.
17. Wang, Y.-Y., et al., *Facile one-step synthesis of Ag@CeO2 core-shell nanospheres with efficient catalytic activity for the reduction of 4-nitrophenol.* CrystEngComm, 2017. **19**(4): p. 684-689.
18. Jian, L., et al., *Investigating the Hybrid-Structure-Effect of CeO2-Encapsulated Au Nanostructures on the Transfer Coupling of Nitrobenzene.* Advanced Materials, 2018. **30**(7): p. 1704416.
19. Yu, H., et al., *Au-CeO2 Janus-like nanoparticles fabricated by block copolymer templates and their catalytic activity in the degradation of methyl orange.* Applied Surface Science, 2018. **427**(Part A): p. 771-778.
20. Bastús, N.G., et al., *Synthesis of Highly Monodisperse Citrate-Stabilized Silver Nanoparticles of up to 200 nm: Kinetic Control and Catalytic Properties.* Chemistry of Materials, 2014. **26**(9): p. 2836-2846.
21. Shevchenko, E.V., et al., *Gold/Iron Oxide Core/Hollow-Shell Nanoparticles.* Advanced Materials, 2008. **20**(22): p. 4323-4329.
22. Montini, T., et al., *Fundamentals and Catalytic Applications of CeO2-Based Materials.* Chemical Reviews, 2016. **116**(10): p. 5987-6041.
23. Davey, W.P., *Precision Measurements of the Lattice Constants of Twelve Common Metals.* Physical Review, 1925. **25**(6): p. 753-761.
24. Schulz, F., et al., *Little Adjustments Significantly Improve the Turkevich Synthesis of Gold Nanoparticles.* Langmuir, 2014. **30**(35): p. 10779-10784.
25. Dong, X., et al., *Shape Control of Silver Nanoparticles by Stepwise Citrate Reduction.* The Journal of Physical Chemistry C, 2009. **113**(16): p. 6573-6576.
26. Piella, J., N.G. Bastús, and V. Puntes, *Size-Controlled Synthesis of Sub-10-nanometer Citrate-Stabilized Gold Nanoparticles and Related Optical Properties.* Chemistry of Materials, 2016. **28**(4): p. 1066-1075.
27. Zhu, F., et al., *In situ growth of Au@CeO2 core-shell nanoparticles and CeO2 nanotubes from Ce(OH)CO3 nanorods.* Journal of Materials Chemistry A, 2013. **1**(2): p. 288-294.

Chapter 6

Heterodimer Hollow Noble Metal-CeO_2 Nanostructures

The heterodimer $AgCeO_2$ nanostructure previously described in Chapter 5 can be transformed into heterodimer $AgAuCeO_2$, $AgPtCeO_2$, $AgPdCeO_2$ hollow NPs at room temperature by means of the GRR of the $AgCeO_2$ nanostructures with the corresponding noble metal precursor. Heterodimer $AgPdCeO_2$ hollow NPs were tested as a catalyst for the selective hydrogenation of alkynes, displaying good to excellent alkene selectivity, similar to the Lindlar catalyst but without incorporating toxic lead.

6.1 Introduction

Catalysis is essential in green chemistry and it is vital for sustainable processes design [1]. With the aim of more efficient catalysis, in the last few years, the design of metal NPs has become quite sophisticated by controlling particle size, morphology and composition. Hydrogenation is by far the most extensively applied catalytic process in the chemical industry [2], with a continuously increasing scope for application, such as multistep synthesis of fine chemicals and pharmaceuticals [3].

The selective hydrogenation of alkynes to alkenes is one of the most important reactions in the manufacturing of bulk and fine chemicals. As environmentally friendly alternatives to the Pb based Lindlar catalyst [$Pb(OAc)_2$-$Pd/CaCO_3$], Pd [4], Fe [5] and Cu [6] metals have been used. Gold NPs have also attracted attention due to their selectivity towards alkenes [7, 8]. However, Au catalysis systems have a limited substrate scope and the requirements of high temperature and additives limit its applicability.

Catalyst modification by introducing another component allows the fine tuning of its catalytic properties [9]. In general bimetallic NPs are known to improve catalytic performance for hydrogenation relative to monometallic NPs [10].

One of the most efficient ways of enhancing the C≡C bond hydrogenation selectivity is by promoting Pd catalysts with another metal [11, 12]. Thus, in recent years, there has been increasing interest in bimetallic compositions as promising catalysts for fine organic synthesis

[13]. The addition of group IB elements to Pd, considerably enhances the selectivity of the catalyst in the hydrogenation of the C≡C bond. Much attention has been focused on Pd-Ag as a very promising alkyne hydrogenation catalyst. There have been a number of studies confirming the efficiency of the Pd-Ag catalyst in hydrogenation. Karakhanov and co-workers [14] found that the product selectivity for a wide variety of alkynes can be increased by using a Pd-Ag hybrid catalyst supported on surface immobilized dendrites. Nikolaev and co-workers [15] demonstrated that the introduction of Ag into the Pd/Al_2O_3 system enhances the stability of the catalyst in hydrogenation of phenylacetylene.

It should be noted that the properties of bimetallic catalysts depend significantly on the degree of NPs homogeneity, and it is mandatory to prevent the formation of Pd crystal domains, which are more active but les selective in the hydrogenation reaction [16]. In the ideal case, the composition of each NP must correspond to the proportions of the components in the catalyst as a whole; however, it has been difficult to attain this degree of homogeneity. From this standpoint, conventional preparation methods are not always acceptable and generally do not avoid the formation of Pd NPs. In this regard, GRR, starting from an Ag template and a Pd precursor, is an efficient way to prepare unprecedented uniform hollow AgPd NPs. Additionally, the positive effect of CeO_2 in hydrogenation reactions has been proved [17, 18].

Catalytic hydrogenation of alkynols is nowadays considered a basic process for producing fine and intermediate chemicals [19]. Two important examples are in the production, through highly selective processes, of fragrant substances used in perfumes and cosmetics, and the production of intermediate precursors in the synthesis of the vitamins E and K and of the provitamin β-carotene [20].

Until now, there have been no reports of well-defined heterodimer hollow noble metal-CeO_2 NPs. In this context, by means of the galvanic replacement reaction, using the heterodimer $AgCeO_2$ as sacrificial templates, however, as is explained in this chapter, it is possible to obtain heterodimer $AgAuCeO_2$, $AgPdCeO_2$ and $AgPdCeO_2$ hollow nanostructures, by using the corresponding metal precursor. The catalytic performance of the heterodimer $AgPdCeO_2$ hollow nanostructure was evaluated using the selective hydrogenation of alkynes and alkynols.

6.2 Materials and methods

6.2.1 Materials

Hydrochloric acid (HCl), nitric acid (HNO_3), polyvinylpyrrolidone (PVP, MW 55,000), ascorbic acid (AA), gold (III) chloride trihydrate >99,9% ($HAuCl_4 \cdot 3H_2O$), potassium hexachloropalladate (IV) (K_2PdCl_6), and Potassium tetrachloroplatinate (II) (K_2PtCl_4) were purchased from Sigma-Aldrich. Cerium (IV) oxide, nanopowder (15-30nm APS Powder, S.A. 30-50 m^2/g) was purchased from Alfa Aesar. Absolute ethanol employed as solvent for the catalytic experiments was purchased from Merck (ACS. Iso. Reag). All chemicals were used as received without further purification. Distilled water passed through a Millipore system (ρ = 18.2 mΩ) was used in all experiments.

6.2.2 Methods

6.2.2.1 Synthesis of heterodimer $AgAuCeO_2$ hollow NPs. In a typical procedure, 1.0 mL of $AgCeO_2$ NPs ($[Ag^0]$ = 1mM) were added to a vial containing 2 mL PVP (5mM) and 1 mL of MQW and 200 μL of AA (0.15 mM). 700 μL of $HAuCl_4$ (1 mM) was injected at a rate of 5 μL/min using a syringe pump. The reaction was stirred for 30 min, and the product was then recovered by centrifugation (8000g, 15 min).

6.2.2.2 Synthesis of heterodimer $AgPtCeO_2$ hollow NPs. In a typical procedure, 0.5 mL of $AgCeO_2$ NPs ($[Ag^0]$ = 1mM) were added to a vial containing 1 mL PVP (5mM) and 250 μL HNO_3 (20 mM). 250 μL of K_2PtCl_4 (1 mM) was injected at a rate of 10 μL/min using a syringe pump. The reaction was stirred for 24 hours, and the product was then recovered by centrifugation (8000g, 15 min).

6.2.2.3 Synthesis of heterodimer $AgPdCeO_2$ hollow NPs. In a typical procedure, 0.5 mL of $AgCeO_2$ NPs ($[Ag^0]$ = 1mM) were added to a vial containing 1 mL PVP and 200 μL HNO_3 (20 mM). 200 μL of K_2PdCl_6 (1 mM) was injected at a rate of 10 μL/min using a syringe pump. The reaction was stirred for 1 hour, and the product was then recovered by centrifugation (8000g, 15 min).

6.2.2.4 Synthesis of AgPd hollow NPs. The standard protocol for the preparation of hollow AgPd NPs consisted of two simple steps: i) First, 200 mL of the Ag NPs solution (prepared by scaling up the seeded-growth method reported by Bastús et al [21]. were precipitated by centrifugation and re-dispersed in 15 mL of PVP 55K (275 mg/mL). The solution was left in a glass vial under soft stir for 24 hours to ensure PVP molecules capped all the surface of the Ag templates. ii) After this, 2.5 mL of HCl (250 mM) and 0.5 mL of 1 mM of K_2PdCl_6 were simultaneously added to the solution. After this very first injection, an additional volume of 9.5 mL of the precursor was added to the vial in 19 consecutive 0.5 mL injections with a time delay of 5 minutes between each one. During the whole process the solution was kept under vigorous stir, at room temperature, until the reaction was complete.

6.2.2.5 Characterization

Absorption spectra of the as synthesized $AgCeO_2$ NPs were acquired with a Shimadzu UV-2401 PC spectrophotometer. The morphology, size and chemical composition of the NPs were visualized using FEI Magellan 400L XHR SEM, in transmission mode operated at 20 kV. TEM, HR-TEM, and STEM/ HAADF images were obtained in a FEI Tecnai G2 F20 S-TWIN HR(S) TEM, operated at an accelerated voltage of 200 kV. A droplet of the sample was drop cast onto a piece of ultrathin carbon-coated 200-mesh copper grid (Ted-pella, Inc.) and left to dry in air. XRD data were collected on a PANalytical X'Pert diffractometer using a Cu Kα radiation source.

6.2.2.6 Catalytic semi-hydrogenation of alkynes. The catalytic reactions were performed in a five position Par 477 autoclave equipped with glass-tubes and magnetic stirrers. In a typical experiment, each tube was charged with 5 mL of ethanol, 0.33 mmol of the substrate and the corresponding catalyst. The autoclave was then pressurized with 10 bar of hydrogen, and heated at 50 °C during a selected time. After the reaction, the autoclave was cooled down, depressurised, and the ethanolic solution analyzed by gas chromatography. The conversion and selectivities were determined using an Agilent 7890A provided with a MS 5975C detector using a HP5-MS column (30 m, 0.25 mm, 0.25 µm).

6.3 Results

6.3.1 Synthesis of heterodimer $AgAuCeO_2$, $AgPtCeO_2$ and $AgPdCeO_2$ hollow nanostructures. Previously produced heterodimer $AgCeO_2$ NPs were transformed into heterodimer bimetallic noble metal (Ag and Au, Pt or Pd) hollow-CeO_2 NPs, in the presence of PVP as stabilizer agent via GRR at room temperature (see methods for experimental details), as is shown in the **Scheme 1**.

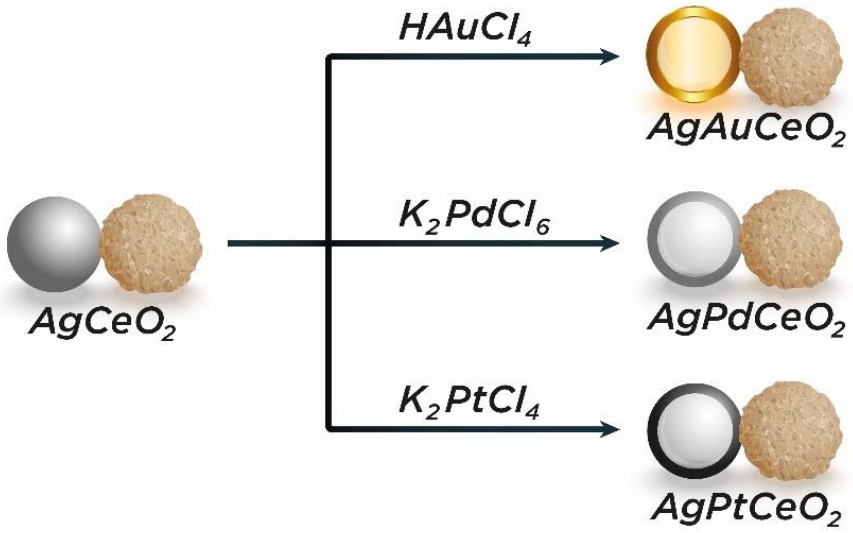

Scheme 1. Representation of the formation of heterodimer noble metal hollow-CeO_2 NPs starting from $AgCeO_2$ heterodimer NPs.

When $HAuCl_4$ was used as metal precursor, the evolution of the GRR could be easily followed by means of UV-vis, as the SPR peak position, as well as the colour of the NPs colloidal suspension, strongly depend on the degree of hollowing, which is directly related to the amount of gold precursor added to the reaction (see **Figure. 6.1**). By adding different amounts of the gold precursor into a fixed volume of heterodimer $AgCeO_2$ NPs, the colour of the solution changed from orange to brown, then purple and finally blue, as shown in the inset pictures of **Figure 6.1**. The UV-Vis spectra of the obtained sample varied with the $HAuCl_4$ amount added, the SPR peaks red-shifted from 410 nm for heterodimer $AgCeO_2$ NPs, to 620 nm for heterodimer $AgAuCeO_2$ hollow NPs.

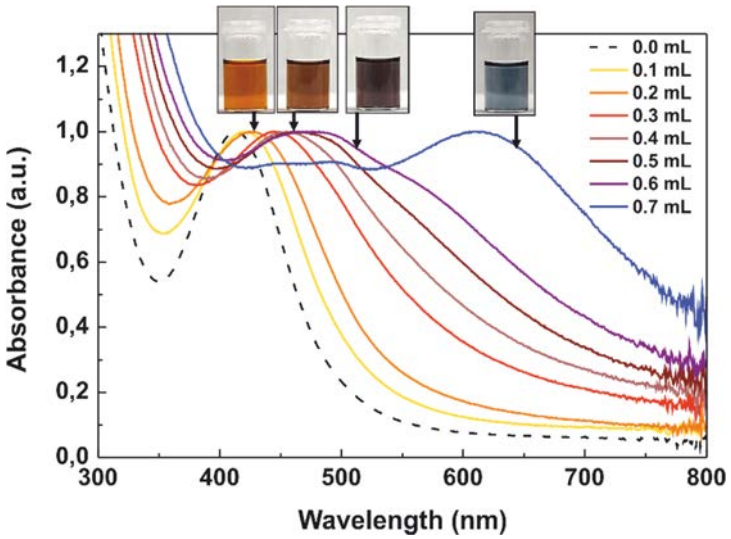

Figure 6.1. UV-Vis spectra of heterodimer $AgCeO_2$ NPs (dotted line) and the galvanic replacement reaction with different volumes of $HAuCl_4$ 1 mM.

In **Figure 6.2A** a selection of HAADF-STEM and HRTEM images of heterodimer $AgAuCeO_2$ hollow NPs is shown. The sample consisted of heterodimer nanostructures in which a hollow AgAu domain with a brighter contrast and an average diameter of 22.8 ± 3.6 nm, was coalesced with a polycrystalline CeO_2 domain. These images are quite similar to those of the previously reported $AgCeO_2$ heterodimers in Chapter 5. It is somewhat clear then, that the heterodimer nanostructure originating from $AgCeO_2$ sample keeps its morphology after the GRR with the Au precursor, as commonly observed in GRR processes.

Figure 6.2B shows HAADF-STEM and TEM images, revealing the homogeneity of the heterodimer $AgPtCeO_2$ NPs across the sample. The metal part consisted of AgPt hollow NPs with an average diameter of 25.4 ± 3.1 nm and wall thicknesses of ~4 nm. The diameter of initial Ag NPs was 19.1 ± 3.1 nm, indicating that the diameter of the metal part had increased about 6 nm with the addition of Pt.

Figure 6.2C shows TEM images of heterodimer $AgPdCeO_2$ hollow NPs. The nanostructures were composed of a 23.1 ± 3.5 nm hollow AgPd domain with a wall thickness of ~5 nm, attached to a polycrystalline CeO_2 domain. By comparing these images in **Figure. 6.1** with the previous heterodimer $AgCeO_2$ sample, which was used as a template, it can be seen that the CeO_2 part of the dimers is exactly the same as the starting sample, therefore the presence of the CeO_2 moiety did not impede the formation of hollow nanostructures.

After the GRR, the nanostructures maintained theirs heterodimer morphology suggesting a strong connection between metal and the CeO_2 nanocrystals.

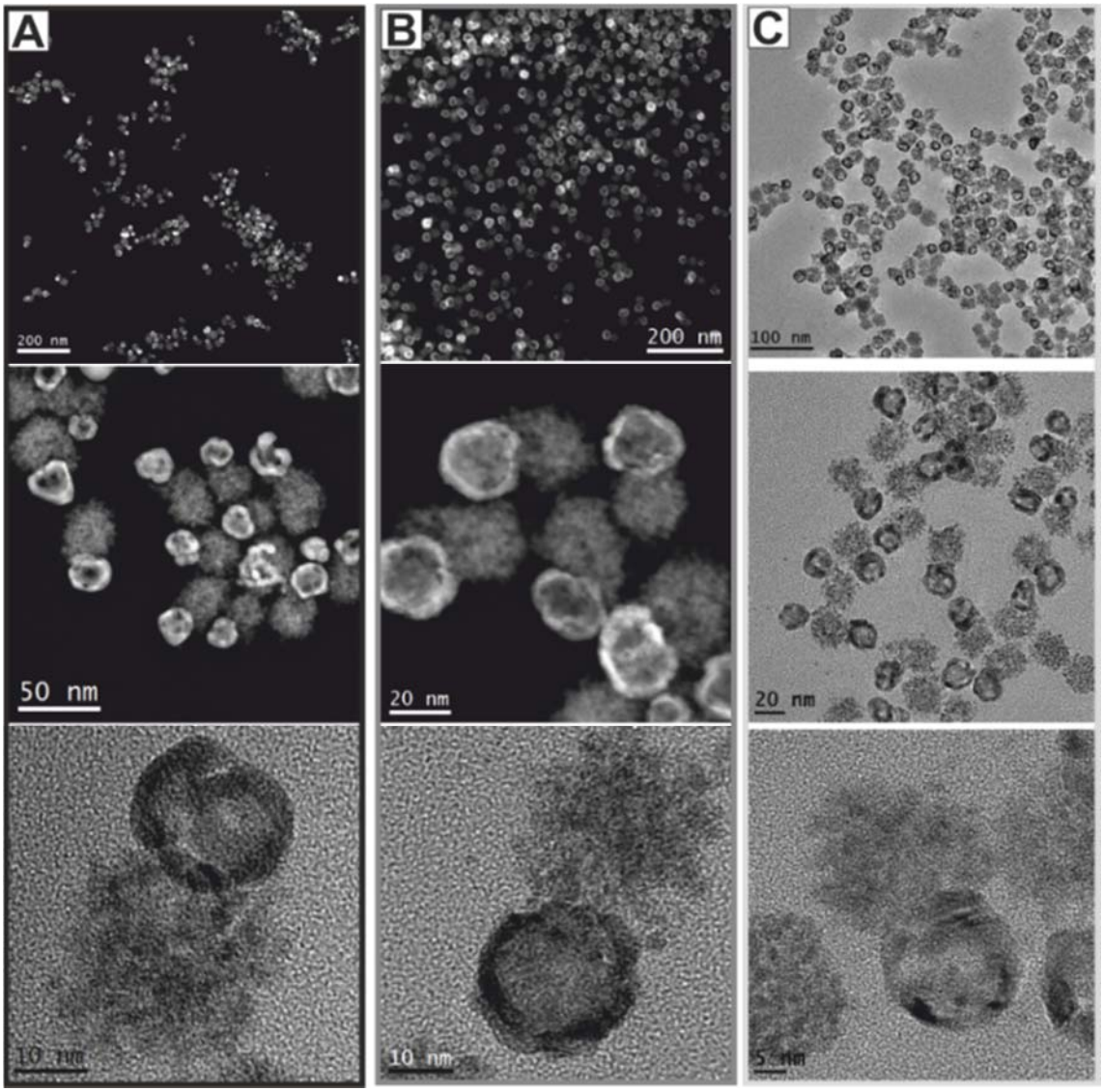

Figure 6.2. A. HAADF-TEM, TEM images of heterodimer $AgAuCeO_2$ hollow NPs. **B.** HAADF-TEM, TEM images of heterodimer $AgPtCeO_2$ hollow NPs and **C.** TEM images of heterodimer $AgPdCeO_2$ hollow NPs.

Figure 6.3A-C shows the STEM-EDS line scan results over the green arrows in the HAADF-STEM images of the heterodimer hollow noble metal metal-CeO_2 NPs, the red line corresponds to Ce, the blue line is Ag and the turquoise line is Au (in **Figure 6.3A**), Pt (in **Figure 6.3B**) and Pd (in **Figure 6.3C**). In **Figure 6.3A**, a single heterodimer $AgAuCeO_2$ hollow NP is presented. As can be seen, the most outer part of the shell (~1 nm in size) is richer in Au compared to the other parts of the hollow nanostructures. In **Figure 6.3B,** a shell of

approximately 3.6 nm of the ~28 nm AgPt domain is clearly visible in the intensity profile, where the intensities of Ag and Pt are also higher than in the rest of the hollow NP. It is important to highlight here that the most outer part of the shell (~1 nm in size) is richer in Pt. In **Figure 6.3C**, a 3 nm Pd rich outer shell is clearly visible in the intensity profile. Ag and Pd are present in the rest of the hollow NPs. In all cases Ce is present along with the noble metal in the junction of the heterodimer nanostructure (see the Ce profile) revealing tight bonding between the hollow and CeO_2 domains of the hybrid.

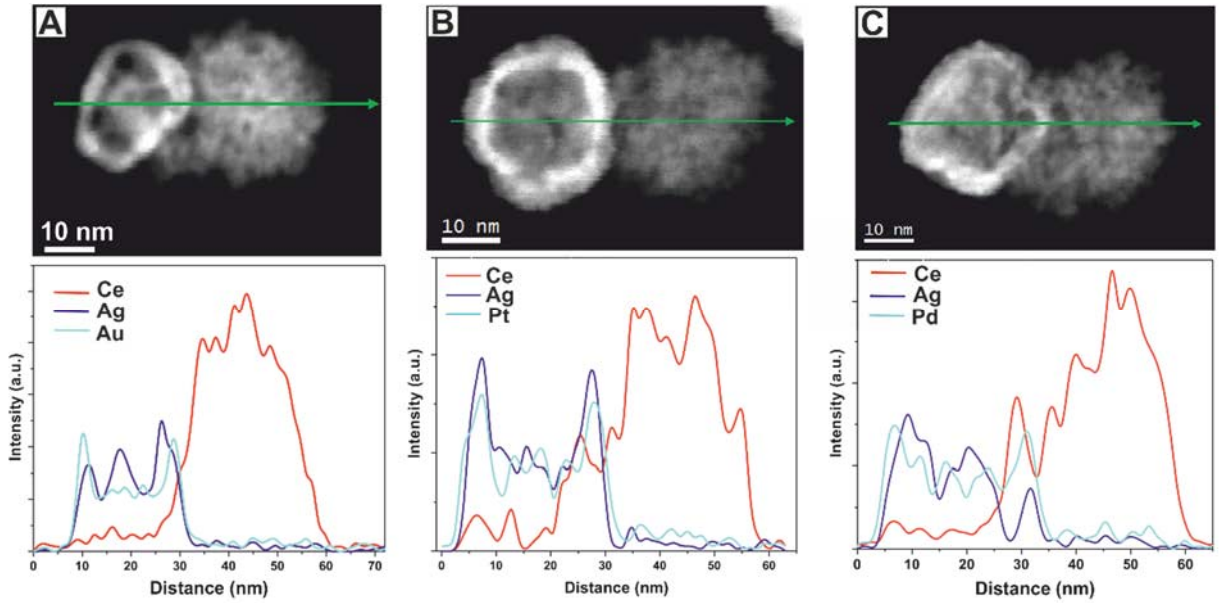

Figure 6.3. A-C. HAADF-STEM images and EDS line scanning profiles of heterodimer $AgAuCeO_2$, $AgPtCeO_2$ and $AgPdCeO_2$ hollow NPs respectively.

The XRD pattern of the heterodimer $AgCeO_2$ nanostructure (**Figure 6.4** black line) and heterodimer $AgAuCeO_2$ (**Figure 6.4** red line), $AgPtCeO_2$ (**Figure 6.4** blue line) and $AgPdCeO_2$ (**Figure 6.4** purple line) hollow NPs shows that the diffractions peaks at $2\theta = 28.6^{\circ}$, 33.1°, 47.3° and 56.4° are in good accordance with the standard diffraction peaks of the fluorite phase of CeO_2 (**Figure 6.4** blue dotted line). The other diffraction peaks are attributed to the hollow bimetallic domains and correspond to JCPDS standard (**Figure 6.4** dotted lines Ag (black, 04-0783), Pd (green, 05-0681), Pt (red, 04-0802) and Au (grey, 04-0784)). The lattice parameters, *a*, 4.07 Å for Au, 4.03 Å for Pd and 3.96 Å for Pt , were found to be slightly different from the references values (4.065 Å for Au, 3.859 Å for Pd and 3.912 Å for Pt [22]), indicating the possible formation of an alloy between Ag and the noble metal added through GRR.

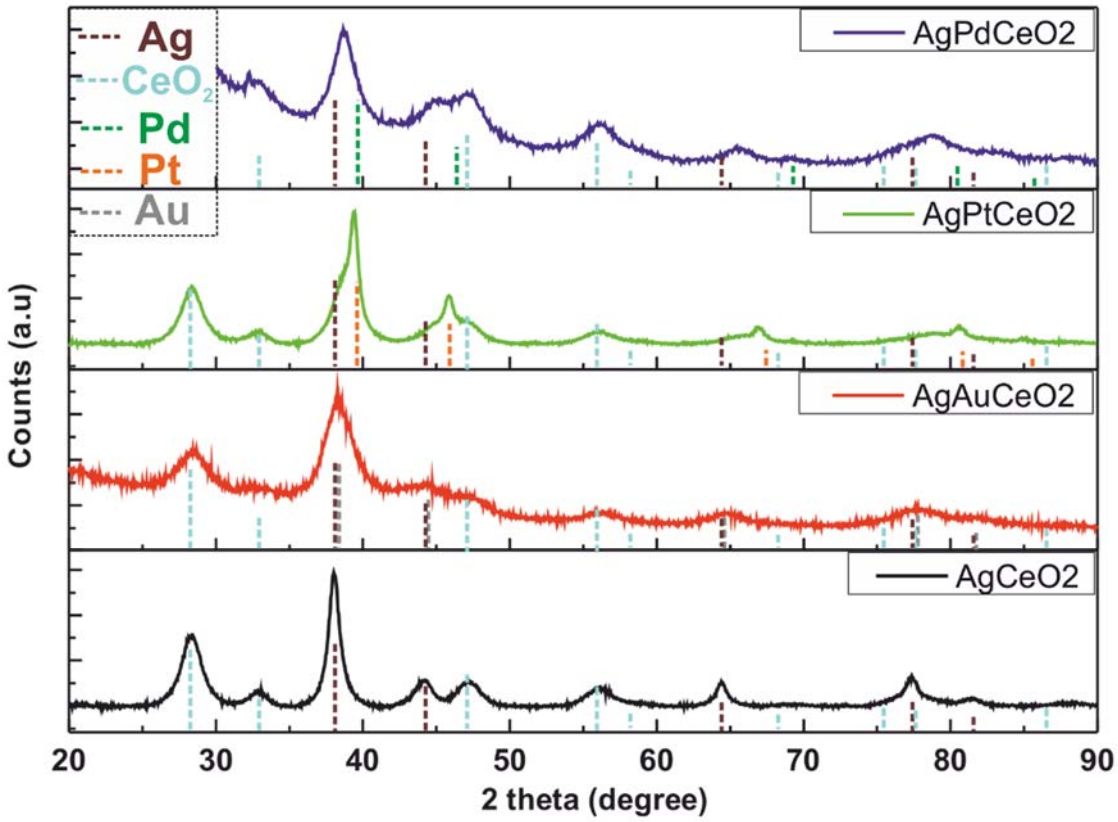

Figure 6.4. XRD patterns of heterodimer $AgCeO_2$ (black) and heterodimer $AgAuCeO_2$ (red), $AgPtCeO_2$ (green) and $AgPdCeO_2$ (blue) hollow NPs. Dotted lines correspond to JCPDS standard for Ag (brown, 04-0783), CeO_2 (light blue, 34-0394), Pd (green, 05-0681), Pt (orange, 04-0802) and Au (grey, 04-0784).

6.3.2 Selective hydrogenation of alkynes catalysed by heterodimer $AgPdCeO_2$ hollow nanostructures.

The catalytic potential of the heterodimer $AgPdCeO_2$ hollow NPs in the selective hydrogenation of alkynes and alkynols was studied. The hydrogenation experiments were carried out in ethanol under 10 bar H_2 and 50˚C. A series of terminal / internal alkynes as well as alkynols were tested to explore the substrate scope. The results are summarized in **Table 1**.

Regarding terminal alkynes, both aliphatic and aromatic alkynes were transformed into the corresponding alkenes with high conversion and selectivity. In the case of 1-octyne (Entry 1, equation 6.1) and 1-ethynylcyclohexene (Entry 13, equation 6.2) total conversion was observed at relatively short reaction times (<2h) with a selectivity towards the alkene of ~95%. For the tested terminal alkynes, phenylacetylene displayed the lowest conversion (74%

after 12 h, entry 12, Equation 6.3) with a 12% of the products corresponded to ethylbenzene. (**Table 6.1**).

Table 6.1. Substrate scope of selective hydrogenation of alkynes and alkynols catalysed by heterodimer $AgPdCeO_2$ hollow NPs.

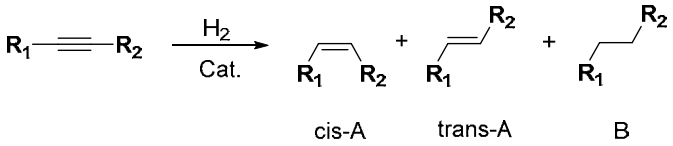

Entry[a]	Catalyst	R_1	R_2	Time, h	Conv, %	Sel. A% Isomer% or sel. cis%	Sel. B%
1	$AgPdCeO_2$	$CH_3(CH_2)_5$	H	2	100	94(2)	6
2	$AgPdCeO_2$	$CH_3(CH_2)_4$	CH_3	2	100	96(96)	4
3	$AgPdCeO_2$	$CH_3(CH_2)_2$	$CH_3(CH_2)_2$	2	100	100(93)	0
4	$AgPdCeO_2$	$CH_3(CH_2)_2$	$CH_3(CH_2)_2$	5	100	100(91)	0
5	$AgPdCeO_2$	$CH_3(CH_2)_2$	$CH_3(CH_2)_2$	20	100	95 (85)	5
6	PdAg[c]	$CH_3(CH_2)_2$	$CH_3(CH_2)_2$	20	13	100 (78)	0
7	CeO_2[d]	$CH_3(CH_2)_2$	$CH_3(CH_2)_2$	20	7	79 (88)	21
8	Lindlar[e]	$CH_3(CH_2)_2$	$CH_3(CH_2)_2$	2	100	98 (86)	2
9	Lindlar[e]	$CH_3(CH_2)_2$	$CH_3(CH_2)_2$	5	100	93 (74)	7
10	Lindlar[e]	$CH_3(CH_2)_2$	$CH_3(CH_2)_2$	20	100	79 (63)	21
11	Nanoselect[f]	$CH_3(CH_2)_2$	$CH_3(CH_2)_2$	2	100	0	100
12	$AgPdCeO_2$	Ph	H	2	74	88	12
13	$AgPdCeO_2$	Cy=[b]	H	1	100	96	4
14	$AgPdCeO_2$	Ph	CH_2CH_3	16	13	82(97)	18
15	$AgPdCeO_2$	Ph	CH_2OH	16	62	84(100)	16
16	$AgPdCeO_2$	$(CH_2)_3OH$	H	1	100	88(1)	12

[a] Reaction conditions: Substrate (0.33 mmol), cat (0.032 mol% Pd), 5 mL ethanol. 10 bar H_2, 50˚C; [b]1-ethynylcyclohexene; [c]0.032 mol % Pd vs 4 –octyne; [d]0.64 mol% CeO_2 (nanopowder, 15-30 nm) vs 4-Octyne; [e]0.032 mol% Pd vs 4-Octyne; [d] Pd Nanoselect catalyst, LF-200 0,032 mol% Pd.

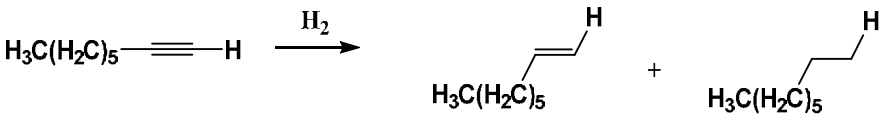

Equation 6.1. Hydrogenation of 1-octyne.

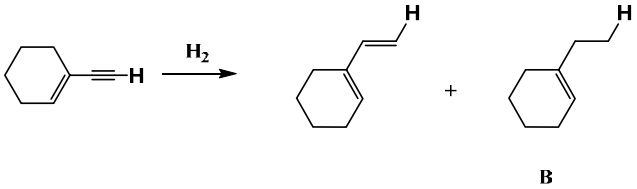

Equation 6.2. Hydrogenation of 1-ethynylcyclohexene

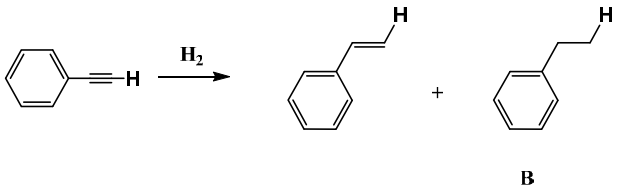

Equation 6.3. Hydrogenation of phenyl acetylene

Various internal aliphatic alkynes also gave the alkenes selectivity, 2-octyne (Entry 2, Equation 6.4) and 4-octyne (Entries 3-5, Equation 6.5). In the case of 2-octyne, an alkene selectivity of 95% was displayed. Similarly, in respect of 4-octyne, the evolution of the reaction products over time was studied by analysing the reaction after 2, 5 and 20 hours. At 2 hours (Entry 3) of reaction, the conversion was 96% and the alkene selectivity 99% (cis:trans, 94:6). For longer reaction times (5 hours, Entry 4), the substrate was fully converted and the alkene selectivity was maintained at about 95%. Even after 20 hours of reaction (Entry 5), the overhydrogenation product did not exceed 5%, thus evidencing the good resistance of the $AgPdCeO_2$ NPs against the overhydrogenation reaction.

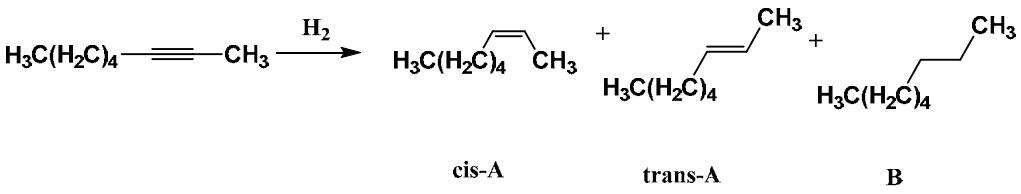

Equation 6.4. Hydrogenation of 2-octyne.

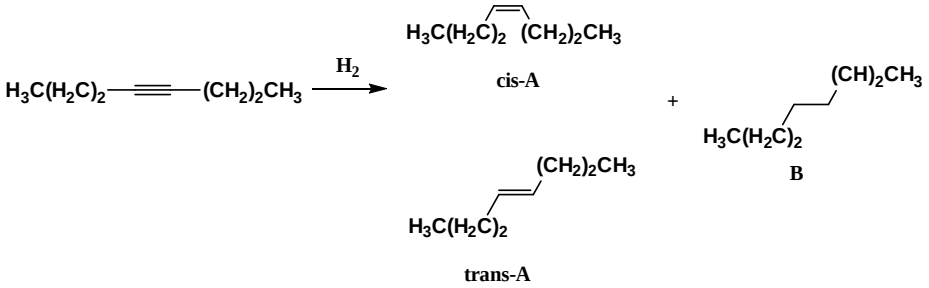

Equation 6.5. Hydrogenation of 4-octyne.

In order to gain insights into the source of the selectivity for this catalyst, hollow AgPd NPs (see Figure. 6.4) were tested under the same catalytic conditions. The activity of hollow AgPd NPs was very low (13% after 20h, entry 6) in comparison to hollow $AgPdCeO_2$ NPs.

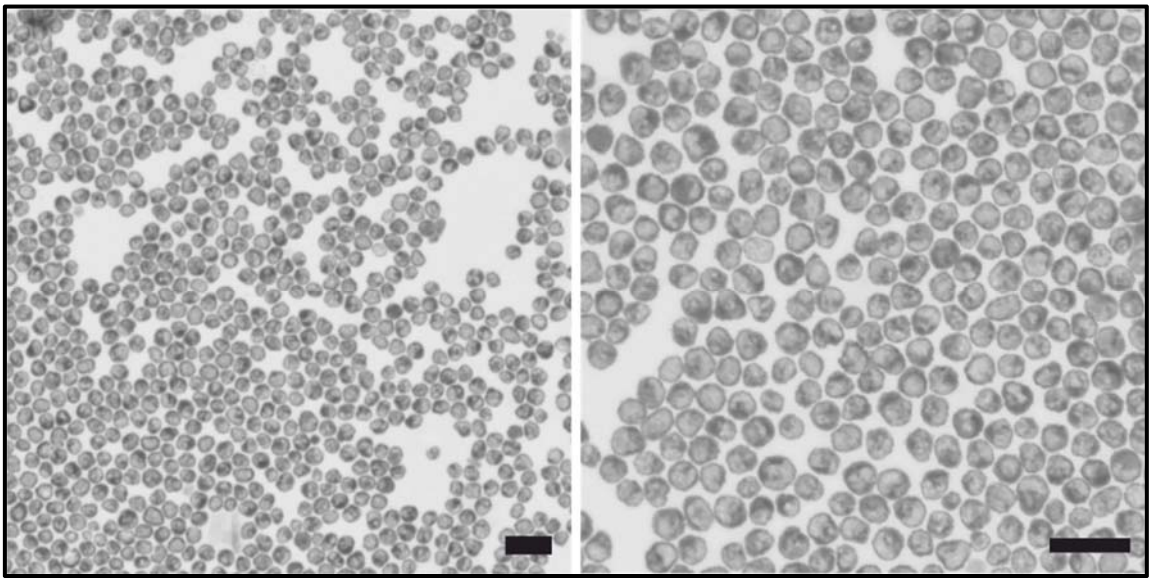

Figure 6.4. TEM images of hollow AgPd NPs. Scale bars represents 100 nm for all images.

Similarly, in order to evaluate the role of CeO_2 in the catalytic performance of $AgPdCeO_2$ NPs, a control experiment using commercial CeO_2 NPs was carried out (Entry 7). Under the tested conditions, the activity of the CeO_2 NPs was negligible, only 7% of alkyne conversion was observed after 20 hours of reaction with an alkene selectivity of 79%. This observation could suggest that the hydrogenation activity observed for heterodimer $AgPdCeO_2$ hollow NPs can be attributed to a possible synergistic effect between the domains formed of the nanostructure.

For comparison purposes, the Lindlar catalyst was tested in the hydrogenation of 4-octyne (Entries 8-10) under the same conditions employed for the heterodimer $AgPdCeO_2$

hollow NPs. The Lindlar catalyst displayed full conversion of the alkyne after 2 hours of reaction (Entry 8). It is remarkable that both, the alkene selectivity and also the *cis* selectivity decreased from 95 to 79% and 86 to 63% respectively, when the reaction was continued for 20h (Entry 10). This observation suggests that under the tested conditions, Lindlar catalyst do not prevent overhydrogenation or isomerization processes whereas the heterodimer $PdAgCeO_2$ NPs does.

With the aim of evaluating the effect of the Ag alloying in the heterodimer $PdAgCeO_2$ hollow NPs, a commercial catalyst based on pure Pd (not Pb poisoned) was also tested in the hydrogenation of 4-octyne (Nanoselect LF-200, Entry 11). Under the tested conditions, full overhydrogenation of the alkyne occurred after 2 hours of reaction. This observation evidences the positive effect of alloying the Pd phase with Ag for the moderation of the hydrogenation activity. Indeed, the promoting effect of silver in PdAg bimetallic systems for the selective hydrogenation of alkynes is widely documented in the literature [23, 24]. The superior performance of heterodimer $AgPdCeO_2$ hollow NPs in terms of the prevention of the over-hydrogenation reaction in comparison with the pure Pd Nanoselect catalyst, could be explained by one or a combination of the following effects. Firstly, the electronic effect of the alloying of Pd with Ag can moderate the catalyst activity, preventing the formation of sub-surface hydrides which are generally responsible for over-hydrogenation issues in palladium based catalysts operating above atmospheric pressures [9]. Secondly, a synergic effect between the CeO_2 and the bimetallic hollow nanostructure could impact positively on catalyst selectivity, as reported for other CeO_2 containing hybrid nanocatalysts [25].

Curiously, for the internal alkyne substituted with phenyl rings, 1-Phenyl-1-butyne (Entry 14, Equation 6.6) displayed a remarkably low conversion of 13% even after prolonged reaction times (16 hours). Additionally, in spite of their low conversion, this alkyne suffered from marked overhydrogenation issues of 18% towards the corresponding alkane.

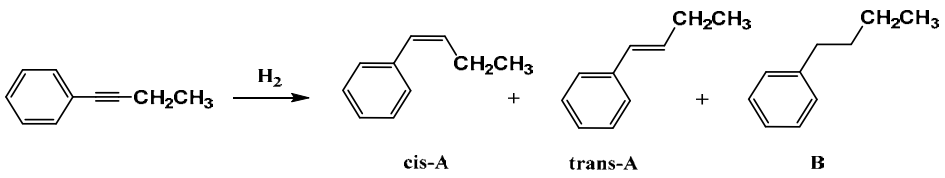

Equation 6.6. Hydrogenation of 1-Phenyl-1-butyne.

Considering that that internal alkynes such as 4-octyne, did not evidence such a retardation in the conversion or premature overhydrogenation, it is possible that a sum of electronic and/or steric effects of the phenyl ring on the triple bond (e.g. charge delocalization) in combination with their particular adsorption properties at the surface of the heterodimer $PdAgCeO_2$ hollow NPs, are responsible for the observed reactivity constrains.

Reducible moieties including benzyl (Entries 12, 14, 15), and cyclohexenyl (Entry 13) were not affected in the reaction.

Regarding the alkynols, both aliphatic and aromatic alkynols were transformed into the corresponding alkenol with total conversion and high selectivity: (88% toward the corresponding alkene) in the case of 4-pentyn-1-ol (Entry 16, Equation 6.7) and a discrete conversion (62%) and excellent selectivity (100%) towards the cis-alkene in the case of 3-phenyl-2-propyn-1-ol (Entry 15, Equation 6.8).

Equation 6.7. Hydrogenation of 4-pentyn-1-ol

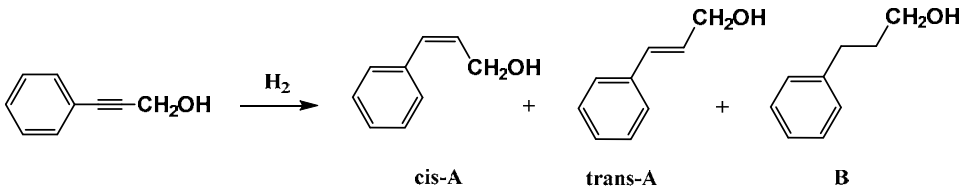

Equation 6.8. Hydrogenation of 3-phenyl-2-propyn-1-ol.

A plausible explanation for a synergy in the heterodimer $AgPdCeO_2$ hollow NPs in the selective hydrogenation of alkynes could arise from the in situ formation of a polar hydrogen species through the heterolytic dissociation of H_2 [25]. The cooperative dissociation of H_2 into polar hydrogen species $H^{\delta+}$ and $H^{\delta-}$ has been reported previously for Au, Ag and basic metal oxides as CeO_2 [26, 27]. The mechanism of the heterolytic dissociation in the case of heterodimer $AgPdCeO_2$ hollow NPs, could be attributed to a similar cooperative effect. It is also reported that polar hydrogen species are favourably reactive to alkynes instead of alkenes, due to the electrophilicity of alkynes [28].

6.4. References

1. Anastas, P. and N. Eghbali, *Green Chemistry: Principles and Practice.* Chemical Society Reviews, 2010. **39**(1): p. 301-312.
2. Blaser, H.-U., *Heterogeneous catalysis for fine chemicals production.* Catalysis Today, 2000. **60**(3): p. 161-165.
3. Roessler, F., *Catalytic Hydrogenation in the Liquid Phase.* CHIMIA International Journal for Chemistry, 2003. **57**(12): p. 791-798.
4. Henning, A.M., et al., *Gold–Palladium Core–Shell Nanocrystals with Size and Shape Control Optimized for Catalytic Performance.* Angewandte Chemie International Edition, 2013. **52**(5): p. 1477-1480.
5. Armbrüster, M., et al., *Al13Fe4 as a low-cost alternative for palladium in heterogeneous hydrogenation.* Nat Mater, 2012. **11**(8): p. 690-693.
6. Semba, K., et al., *Copper-Catalyzed Highly Selective Semihydrogenation of Non-Polar Carbon-Carbon Multiple Bonds using a Silane and an Alcohol.* Advanced Synthesis & Catalysis, 2012. **354**(8): p. 1542-1550.
7. Azizi, Y., C. Petit, and V. Pitchon, *Formation of polymer-grade ethylene by selective hydrogenation of acetylene over Au/CeO2 catalyst.* Journal of Catalysis, 2008. **256**(2): p. 338-344.
8. Yan, M., et al., *Nanoporous Gold Catalyst for Highly Selective Semihydrogenation of Alkynes: Remarkable Effect of Amine Additives.* Journal of the American Chemical Society, 2012. **134**(42): p. 17536-17542.
9. Lopez, N. and C. Vargas-Fuentes, *Promoters in the hydrogenation of alkynes in mixtures: insights from density functional theory.* Chemical Communications, 2012. **48**(10): p. 1379-1391.
10. Ferrando, R., J. Jellinek, and R.L. Johnston, *Nanoalloys: From Theory to Applications of Alloy Clusters and Nanoparticles.* Chemical Reviews, 2008. **108**(3): p. 845-910.
11. Nikolaev, S.A., et al., *Catalytic hydrogenation of alkyne and alkadiene impurities from alkenes. Practical and theoretical aspects.* Russian Chemical Reviews, 2009. **78**(3): p. 231.
12. Borodziński, A. and G.C. Bond, *Selective Hydrogenation of Ethyne in Ethene-Rich Streams on Palladium Catalysts. Part 1. Effect of Changes to the Catalyst During Reaction.* Catalysis Reviews, 2006. **48**(2): p. 91-144.
13. Ananikov, V.P., et al., *Development of new methods in modern selective organic synthesis: preparation of functionalized molecules with atomic precision.* Russian Chemical Reviews, 2014. **83**(10): p. 885.
14. Karakhanov, E.A., et al., *Alkyne hydrogenation using Pd–Ag hybrid nanocatalysts in surface-immobilized dendrimers.* Applied Organometallic Chemistry, 2015. **29**(11): p. 777-784.
15. Nikolaev, S.A. and I.N. Krotova, *Partial hydrogenation of phenylacetylene over gold- and palladium-containing catalysts.* Petroleum Chemistry, 2013. **53**(6): p. 394-400.
16. Rassolov, A.V., et al., *Catalytic properties of nanostructured Pd–Ag catalysts in the liquid-phase hydrogenation of terminal and internal alkynes.* Kinetics and Catalysis, 2016. **57**(6): p. 853-858.
17. Concepción, P., et al., *Chemoselective Hydrogenation Catalysts: Pt on Mesostructured CeO2 Nanoparticles Embedded within Ultrathin Layers of SiO2 Binder.* Journal of the American Chemical Society, 2004. **126**(17): p. 5523-5532.
18. Montini, T., et al., *Fundamentals and Catalytic Applications of CeO2-Based Materials.* Chemical Reviews, 2016. **116**(10): p. 5987-6041.
19. Yarulin, A., et al., *Size-Effect of Pd-(Poly(N-vinyl-2-pyrrolidone)) Nanocatalysts on Selective Hydrogenation of Alkynols with Different Alkyl Chains.* The Journal of Physical Chemistry C, 2013. **117**(26): p. 13424-13434.

20. Bonrath, W., M. Eggersdorfer, and T. Netscher, *Catalysis in the industrial preparation of vitamins and nutraceuticals.* Catalysis Today, 2007. **121**(1): p. 45-57.
21. Bastús, N.G., et al., *Synthesis of Highly Monodisperse Citrate-Stabilized Silver Nanoparticles of up to 200 nm: Kinetic Control and Catalytic Properties.* Chemistry of Materials, 2014. **26**(9): p. 2836-2846.
22. Davey, W.P., *Precision Measurements of the Lattice Constants of Twelve Common Metals.* Physical Review, 1925. **25**(6): p. 753-761.
23. Calver, C.F., P. Dash, and R.W.J. Scott, *Selective Hydrogenations with Ag□Pd Catalysts Prepared by Galvanic Exchange Reactions.* ChemCatChem, 2011. **3**(4): p. 695-697.
24. Mitsudome, T., et al., *Design of Core-Pd/Shell-Ag Nanocomposite Catalyst for Selective Semihydrogenation of Alkynes.* ACS Catalysis, 2016. **6**(2): p. 666-670.
25. Mitsudome, T., et al., *One-step Synthesis of Core-Gold/Shell-Ceria Nanomaterial and Its Catalysis for Highly Selective Semihydrogenation of Alkynes.* Journal of the American Chemical Society, 2015. **137**(42): p. 13452-13455.
26. Mitsudome, T., et al., *Design of a Silver–Cerium Dioxide Core–Shell Nanocomposite Catalyst for Chemoselective Reduction Reactions.* Angewandte Chemie International Edition, 2012. **51**(1): p. 136-139.
27. Mitsudome, T., et al., *Core–Shell AgNP@CeO2 Nanocomposite Catalyst for Highly Chemoselective Reductions of Unsaturated Aldehydes.* Chemistry – A European Journal, 2013. **19**(17): p. 5255-5258.
28. Spencer, J.Y. and B. Jonathan, *Regioselective Hydrometalation of Alkenes Reveals the Amphipolar Nature of the Pd−H Bond in Heterogeneous Hydrogenation.* The Journal of Organic Chemistry, 1997. **62**(25): p. 8618-8619.

Chapter 7.

General Conclusions.

Al the nanostructures presented in this thesis were fully characterized in order to determine their morphology, size and composition by different techniques including: UV-Vis spectroscopy, SEM, TEM, HR-TEM, HAADF-STEM microscopy, EDS line scan composition analysis or EDS elemental mapping composition analysis, EELS chemical composition analysis and XRD.

Herein, is a compilation of the various interim conclusions made throughout the thesis.

Hollow Complex Nanostructures.

The effect of different surfactants on the synthesis of AgAu nanoboxes was studied. When halogenated surfactants such as CTAB or CTAC were used, different nanostructures ranging from pinholed nanoboxes to double walled nanoboxes were obtained. The amount of gold precursor added to the reaction determined the final morphology of the nanoboxes as well as the optical properties of the resulting nanostructures. When CTApTS, a non-halogenated ionic surfactant was used, only single walled nanoboxes with and irregular thick wall were obtained.

When PVP was used changes in concentration produced both, well-defined single walled nanoboxes or highly porous nanoboxes with a SPR band around 1000 nm.

Different microscope techniques, such as, HAADF-STEM images, TEM images and EDS elemental mapping and line scanning analysis were used to determine the morphology, size and composition of the produced nanostructures.

A sensing experiment to measure the response of spherical Au NPS and single walled nanoboxes to sequential conjugation events with BSA and anti-BSA was conducted. This experiment showed that the hollow nanoboxes were 4 times more sensitive than the spherical solid counterpart.

Multidomain and Multicomponent Nanotubes

A facile and effective methodology was presented for the production at room temperature of bimetallic AgAu multidomain NTs, trimetallic AgAuPt, AgAuPd and tetrametallic AgAuPdPt NTs starting from Ag NWs.

The morphology of the obtained nanostructures was controlled by the addition of CTAB and/or AA in a suspension containing Ag NWs. Sequential GRR was used for the production of multimetallic nanostructures. In the formation process, the decrease in the reduction rate of $AuCl_4^-$ by CTAB and AA played a key role in the generation of the bimetallic AgAu multidomain NTs. In the formation of the multimetallic nanostructures, CTAB played an important role as a directing agent for the epitaxial deposition of the metal.

The catalytic performance of the multimetallic NTs was evaluated by the reduction of 4-nitrophenol to 4-aminophenol with $NaBH_4$ at room temperature. The findings show that all the nanostructures synthesized exhibited a good catalytic performance two orders of magnitude higher than Ag NWs.

Ag Nanorods

In summary, a general polyol method for the facile synthesis of short Ag NRs (length of 55.6 ± 9.3 nm and diameter of 19.3 ± 3.0 nm, aspect ratio 2.8), was developed. This method used EG as solvent and reducing agent, CF_3COOAg as a Ag precursor, high molecular weight PVP as a stabilizer and directing agent and TA at sub-stoichiometric concentrations as a co-reducer.

The effect of different parameter on the production of Ag NRs were studied. This parameter were: TA concentration, PVP molecular weight, reaction temperature, and silver precursor. From the study of these parameter the optimal conditions for the production of monodisperse low aspect ratio Ag NRs are: TA 0.25 mM, PVP molecular weight 1,300,000, a temperature of 170˚C and CF_3COOAg as silver precursor.

The produced Ag NRs were transformed into hollow AgAu NRs, *via* GRR at room temperature with $HAuCl_4$ in the presence of CTAB. These hollow AgAu NRs presented a LSPR band in the near infrared region, which make them a good candidate for biomedical applications.

Hybrid Nanostructures

Well defined, monodisperse heterodimer $AgCeO_2$, core-shell $Ag@CeO_2$ and hybrid $AuCeO_2$ NPs were synthesized via a novel, facile and reproducible one-pot aqueous approach. This synthetic strategy allowed the formation of noble metal-CeO_2 nanostructures, with control of the interface between the noble metal and the CeO_2 domains.

In the case of $AgCeO_2$ nanostructures, by adjusting the initial pH of the reaction it was possible to control the final morphology of the hybrid $AgCeO_2$ NPs, from heterodimer to core-shell nanostructures.

In the formation process of the noble metal-CeO_2 hybrid nanostructures, sodium citrate plays multiple key roles in complexing, directing, stabilizing and as a reducing agent.

Heterodimer Hollow Noble Metal-CeO2 Nanostructures

The heterodimer $AgCeO_2$ nanostructures were used as a template for the production of heterodimer $AgAuCeO_2$, $AgPtCeO_2$ and $AgPdCeO_2$ hollow NPs, *via* GRR with the corresponding metal precursor, at room temperature.

The results suggest that the simple and scalable synthetic strategy presented will be of great significance for the design and preparation of active and stable catalysts with complex compositions and heterodimer hollow nanostructures. Specifically, it was demonstrated that heterodimer $AgPdCeO_2$ hollow NPs, act as efficient catalysts for highly selective hydrogenation of various alkynes and alkynols with H_2. Furthermore, the dimeric structure of heterodimer $AgPdCeO_2$ hollow nanostructures can effectively exploit the interfacial cooperative catalysis between AgPd and CeO_2 for the dissociation of H_2 in a heterolytic cleavage, allowing the selective hydrogenation of alkynes and alkynols.

Appendix 1. List of Abbreviations

λmax: maximal absorption wavelength

AA: ascorbic acid

Ab: antibody

BSA: bovine serum albumin

Bp: boiling point

CTAB: cetyltrimethylammonium bromide

CTAC: cetyltrimethylammonium chloride

CTApTS: cetyltrimethylammonium p-toluene sulfonate

EDS: energy dispersive spectroscopy

EG: ethylene glycol

FCC: face-centered cubic

GRR: Galvanic replacement reaction

HAADF-STEM: High angle annular dark field scanning transmission electron microscopy

HHDMA: hexadecyl(2-hydroxyethyl)dimethylammonium dihydrogenphosphate

JCPDS: Joint Committee on Powder Diffraction Standards

MIN: minutes

MQW: milli Q water

MW: Molecular weight

NC(s): Nanocube(s)

NP(s): Nanoparticle(s)

NT(s): Nanotube(s)

NW(s): Nanowire(s)

PVP: polyvinylpyrrolidone

SC: Sodium citrate

SERS: surface enhanced Raman scattering

SPRs: surface plasmon resonance

STEM: scanning transmission electron microscop

TA: Tannic acid

TEM: transmission electron microscopy

UV-Vis: Ultraviolet visible

XRD: X-ray diffraction

Appendix 2. Publications and Contributions

Publications

Javier Patarroyo, Jorge A. Delgado, Florind Merkoçi, Aziz Genç, Jordi Arbiol, Neus G. Bastús, Cyril Godard, Carmen Claver and Victor Puntes. *Bimetallic $PdAgCeO_2$ hollow nanoparticles as structured catalyst for the selective hydrogenation of alkynes.* In preparation

Neus G. Bastús, Javier Patarroyo, Florind Merkoçi, Aziz Genç, Jordi Arbiol, and Victor Puntes *Facile Synthesis of $AgCeO_2$ heterodimer nanocrystals.* In preparation

Javier Patarroyo, Aziz Genç, Jordi Arbiol, Neus G. Bastús and Victor Puntes. *A general strategy for the synthesis of multidomain and multicomponent noble metal nanotubes.* In preparation

Neus G. Bastús, Jordi Piella, Javier Patarroyo, Jordi Arbiol and Victor Puntes. *A Coupled Redox Approach for the Interface-controlled Synthesis of Au/CeO_2 Heterostructured Nanocrystals.* In preparation

Florind Merkoçi, Javier Patarroyo, Lorenzo Russo, Jordi Piella, Aziz Genç, Jordi Arbiol, Neus G. Bastús and Victor Puntes. Understanding the hollowing process in Nanocrystals: the case of Pt and Ag. In preparation

Sema Karabel Ocal, Javier Patarroyo, N. Burak Kiremitler, Sami Pekdemir, Victor F. Puntes, and M. Serdar Onses. *Plasmonic Assemblies of Gold Nanorods on Nanoscale Patterns of Poly(ethylene glycol): Application in Surface-Enhanced Raman Spectroscopy*. **Journal of Colloid and Interface Science,** 2018, 532, 449-455

Lorenzo Russo, Florind Merkoçi, Javier Patarroyo, Jordi Piella, Neus G. Bastús and Victor Puntes. *Time- and size-resolved plasmonic evolution with nm resolution of galvanic replacement reaction of AgAu nanoshells*. **Chemistry of Materials**. 2018, 30 (15), 5098-5107.

Yazdi Amirali, Abo Makeb Ahmad, Garzón-Tovar Luís, Patarroyo Javier, Moral-Vico Javier, Alonso Amanda, Sánchez Antoni, Bastús Neus, Imaz Inhar, Font Xavier, Puntes Victor, Maspoch Daniel. *Core-shell Au/CeO_2 nanoparticles supported in UiO-66 beads exhibiting full CO conversion at 100 ˚C*. **J. Mater. Chem. A**, 2017, 5, 13966-13970

N. Burak Kiremitler, Sami Pekdemir, Javier Patarroyo, Ilker Torun, Sema Karabel, Victor F. Puntes, and M. Serdar Onses. *Assembly of plasmonic nanoparticles on nanopatterns of polymer brushes fabricated by electrospin nanolithography*. **ACS Macro Lett.** 2017, 6, 603−608.

Aziz Genç, Javier Patarroyo, Jordi Sancho-Parramon, Raul Arenal, Neus G. Bastús, Victor Puntes, Jordi Arbiol. *Spatially Mapping the Plasmon Resonances of Hollow 1D Nanostructures: Hybrid AuAg Nanotubes*. **European Microscopy Congress 2016: Proceedings**. DOI: 10.1002/9783527808465.EMC2016.5884.

Aziz Genç, Javier Patarroyo, Jordi Sancho-Parramon, Neus G. Bastús, Victor F. Puntes, and Jordi Arbiol. *Hollow metal nanostructures for enhanced plasmonics: synthesis, local plasmonic properties and applications.* **Nanophotonics**. September 2016*,* 6 (1), 193-213. DOI: 10.1515/nanoph-2016-0124

Javier Patarroyo, Aziz Genç, Jordi Arbiol, Neus G. Bastús, Victor Puntes. *One-pot Polyol Synthesis of Highly Monodisperse Short Green Silver Nanorods*. **Chem. Commun***., 2016, 52, 10960-10963.*

Aziz Genç, Javier Patarroyo, Jordi Sancho-Parramon, Martial Duchamp, Edgar Gonzalez, Neus G. Bastús, Lothar Houben, Rafal Dunin-Borkowski, Victor F. Puntes, Jordi Arbiol. *Hollow metal nanostructures for enhanced plasmonics*. **Proc. SPIE 9722**, Colloidal Nanoparticles for Biomedical Applications XI, 972206 (27 April 2016); doi: 10.1117/12.2211598

Aziz Genç, Javier Patarroyo, Jordi Sancho-Parramon, Raul Arenal, Martial Duchamp, Edgar E. Gonzalez, Luc Henrard, Neus G. Bastús, Rafal E. Dunin-Borkowski, Victor F. Puntes, and Jordi Arbiol. *Tuning the Plasmonic Response up: Hollow Cuboid Metal Nanostructures,* **ACS Photonics.** 2016, 3 (5), 770–779.

Neus G. Bastús; Edgar González; Joan Esteve; Jordi Piella; Javier Patarroyo; Florind Merkoçi; Víctor Puntes. *Exploring New Synthetic Strategies for the Production of Advanced Complex Inorganic Nanocrystals.* **Zeitschrift für Physikalische Chemie.** 2015, 229, 65–83.

Contributions to conferences

Javier Patarroyo, Aziz Genç, Jordi Arbiol, Neus G. Bastús and Victor Puntes. *One-pot Polyol Synthesis of Highly Monodisperse Short Green Silver Nanorods*. 3rd International Conference on polyol mediated Synthesis. June 25-27, 2018. Madrid. Spain. ***2nd poster prize.***

Javier Patarroyo, Aziz Genç, Jordi Arbiol, Neus G. Bastús and Victor Puntes. *One-pot Polyol Synthesis of Highly Monodisperse Short Green Silver Nanorods*. II Workshop on Chemistry of Group 11 Elements. January 26-27, 2017. Barcelona. Spain.

Javier Patarroyo, Aziz Genç, Jordi Sancho-Parramon, Raul Arenal, Martial Duchamp, Edgar E. Gonzalez, Luc Henrard, Neus G. Bastús, Rafal E. Dunin-Borkowski, Victor F. Puntes, and Jordi Arbiol. *Tuning the Plasmonic Response up: Hollow Cuboid Metal Nanostructures.* JPHD 2016: II Scientific Meeting of BNC-b Students, June 29-30 2016. Bellaterra. Spain.

Javier Patarroyo, Aziz Genç, Jordi Sancho-Parramon, Raul Arenal, Martial Duchamp, Edgar E. Gonzalez, Luc Henrard, Neus G. Bastús, Rafal E. Dunin-Borkowski, Victor F. Puntes, and Jordi Arbiol. *Tuning the Plasmonic Response up: Hollow Cuboid Metal Nanostructures.* NaNaX7: Nanoscience with Nanocrystals. April 4-8, 2016. Marburg. Germany.

Javier Patarroyo, Neus G. Bastús, Aziz Genç, Jordi Arbiol, Víctor Puntes *A General Strategy for the Production of (Ag/Au) Multidomain Bimetallic and (Ag/Au/Pt or Pd) Trimetallic Noble Metal Nanotubes. ACIN 2015.* Third International Conference on Advanced Complex Inorganic Nanomaterials. July 13-17, 2015. Namur. Belgium.

Javier Patarroyo, Aziz Genç, Raul Arenal, Edgar González, Jordi Arbiol, Víctor Puntes. *STEM-EELS mapping of the surface plasmon resonances of bimetallic AuAg complex hollow nanoparticles*. NaNaX6: Nanoscience with Nanocrystals. May 18-23, 2014. Bad Hofgastein. Austria.

Javier Patarroyo, Edgar González, Jordi Arbiol, Víctor Puntes. *Nanoscale features of complex hollow nanoparticles engineered for their application in drug delivery.* XXVIII Trobades Científiques de la Mediterrània. October 24-26, 2012. Maó, Menorca. Spain